Space Environmental Effects on Graphite-Epoxy Compressive Properties and Epoxy Tensile Properties

by

Derek J. Fox

Thesis submitted to the Faculty of the

Virginia Polytechnic Institute and State University

in partial fulfillment of the requirements for the degree of

Master of Science

in

Engineering Mechanics

APPROVED:

Carl T. Herakovich, Chairman

Zafer Gurdal

Marek-Jerzy Pindera

June, 1987

Blacksburg, Virginia

Space Environmental Effects on Graphite-Epoxy Compressive Properties and Epoxy Tensile Properties

by

Derek J. Fox

Carl T. Herakovich, Chairman

Engineering Mechanics

(ABSTRACT)

The objectives of this study were to characterize the effects of the space environment on the compressive behavior of T300/934 graphite/epoxy composite material and on the tensile properties of the neat (unfilled) epoxy matrix material. Both materials were tested in the baseline state and after exposure to electron radiation (total dose of 10,000 Mrads of 1 MeV electrons at a dose rate of 50 Mrads/hr). Irradiation was conducted under vacuum and simulates 30 year, "worst case", exposure in geosynchronous earth orbit.

A compressive test method was developed to characterize thin (8-ply) unidirectional coupons. Compression tests were conducted at cryogenic (-250° F; -157° C), room, and elevated (250° F; 121° C) temperatures. Elastic and strength properties were obtained in the principal material directions (E_1, E_2, ν_{12}, ν_{21}, X_c, Y_c). Tensile specimens of the neat Fiberite 934 epoxy resin were fabricated and tests were conducted at room and elevated (250° F; 121° C) temperatures. Elastic and strength properties (E, ν, σ_{ult}) were obtained.

Irradiation and temperature were found to have a significant effect on composite and neat resin properties. Properties tended to improve at cryogenic temperature and degrade at elevated temperature. Irradiation degraded properties at all temperatures, with the degradation being most severe at elevated temperature.

Acknowledgements

This work was performed under the sponsorship of the NASA-Virginia Tech Composites Program and funded by NASA Grant NAG-1-343. This support is gratefully acknowledged. The author thanks the students and faculty associated with the Composite Mechanics Group at Virginia Tech for their guidance, advice, and friendship. In particular, Profs. Herakovich, Pindera, and Gurdal are acknowledged for serving on the author's committee and for their many valuable discussions on this work.

The engineers, scientists, and technicians of the Applied Materials Branch at NASA-Langley Research Center, in particular, Dr. S.S. Tompkins and Mr. D.E. Bowles, are acknowledged for sharing their insight into a number of technical problems and questions. Mr. Randy Loudermilk is acknowledged for his help in the mechanical testing portion of this work.

The support and friendship of the author's fellow students is gratefully acknowledged. Finally, the author thanks his family and friends for their encouragement, undeserved praise, and, most of all, for simply "being there".

Dedication

This study would have been impossible without the advise and tireless effort of Mr. George F. Sykes, Jr.. George was tragically killed in an automobile accident before the completion of this report. He was an outstanding researcher in the Applied Materials Branch at NASA-Langley Research Center and a valued friend. He is sorely missed. This report is dedicated to the memory of George, which lives on in all who knew him.

Table of Contents

List of Illustrations

List of Tables

1.0 Introduction

The use of advanced composite materials, particularly graphite/epoxy (Gr/Ep), in the design of space vehicles and structures is increasing. The Hubble Space Telescope's main structural elements are Gr/Ep tubes, and it is nearly certain that the space station truss structure will be constructed of Gr/Ep tubes. Several large solar arrays and antenna structures, presently in the planning stage, are likely to use composites in their primary structural elements [1].

There are several characteristics of Gr/Ep which make it a near ideal material for such applications. Among the most important of these is the ability to tailor the properties of the finished component by selection of ply-angles. This allows the designer to use structural components with very low CTE (coefficient of thermal expansion), high stiffness and strength, and excellent damping characteristics. In addition, the low-density of the materials eases payload requirements.

Before the advantages of composites can be fully exploited, the effects of long term exposure to the space environment must be assessed.

1.1 The Space Environment

Three parameters of the space environment were investigated in this study: vacuum, electron radiation, and temperature. These parameters are believed to be the most significant degradation mechanisms present in the geosynchronous earth orbit (GEO) environment. While in space, all materials are subjected to a near perfect vacuum. This can produce serious outgassing and, subsequently, induce void formation and shrinkage problems. All materials in this study were held in vacuum for a minimum of three weeks. In addition, all the irradiation was conducted under hard vacuum.

The space radiation environment covers nearly the entire electromagnetic spectrum from visible and ultraviolet (UV) light to charged particles (electrons, protons) to hard cosmic and gamma rays. It is impractical and unnecessary to simulate all these types of radiation. In GEO the most significant forms of radiation are UV, electrons, and protons. Lower energy forms of radiation (visible light) are believed to have negligible, if any, effect on structural materials and the higher energy forms of radiation (x-rays, cosmic rays) have such low fluxes as to be insignificant. In addition, it is usually assumed that fast neutrons, gamma rays, and accelerated electrons all provide comparable degradation of epoxies, if the exposure is conducted under vacuum [2].

Ultraviolet and proton irradiation affect primarily the exposed surfaces of materials and while they are likely to degrade thin film coatings and highly polished surfaces, they are of small importance to relatively thick structural materials. On the other hand, electron radiation is highly penetrating and experienced in high doses over the expected 20-30 year life of a space structure. Electron radiation is the only form of irradiation investigated in this study.

The thermal environment of space is literally day-and-night. Surfaces exposed to the sun experience temperature upwards of 250° F (121° C), while those shadowed from the sun are

in the icy cold of space (-250° F; -157° C). Thermal conduction and cycling of the structure between light and dark means that these extremes won't be reached in most space structures. Nonetheless, the mechanical tests conducted in this study were performed at cryogenic (-250° F; -157° C), room, and elevated (250° F; 121° C) temperatures to span the entire space equivalent range.

1.2 Objectives

The objectives of this study are to characterize the effects of the space environment on the compressive properties of a graphite/epoxy composite (T300/934) and the tensile properties of the neat (unfilled) epoxy resin, Fiberite 934.

Previous work (to be discussed in the next chapter) has found that the space environment can produce large effects on matrix dependent composite properties, while fiber-dominated properties are essentially inert. Because longitudinal compressive properties are matrix dependent, it was believed they would be more sensitive to radiation and temperature than the corresponding tensile properties. The investigation of the neat resin was intended to provide a more quantitative measurement of the changes in the epoxy properties due to temperature and irradiation.

2.0 Background

The first section of this chapter is an overview of some of the recent work on irradiation effects on composites. Particular emphasis is given to the irradiation procedures used, the mechanical (or other) properties measured, and the most significant results obtained. Unless otherwise stated, the observations and conclusions are those of the respective authors.

Following the discussion of the literature, the materials and irradiation procedures used in this study are described. Finally, the effects of irradiation on the glass-transition temperature will be presented and discussed.

2.1 Literature Review

This report is the third in a sequence produced under sponsorship of the NASA-Virginia Tech Composites Program on the effects of electron irradiation on Gr/Ep, specifically the T300/934 material system. Milkovich, Herakovich, and Sykes [3-6] investigated the in-plane tensile and shear properties, thermomechanical and dynamic mechanical properties, and the combined

effect of thermal cycling and irradiation. Reed, Herakovich, and Sykes [7-8] studied the effect of chemically modifying the matrix material on the in-plane composite tensile and shear properties. In addition, they investigated the changes in energy dissipation under cyclic loading in both the standard, T300/934, and modified material systems.

In general, both studies found that matrix dependent properties (transverse tensile and shear properties) were most affected by electron irradiation and degradation was most significant at elevated (250° F; 121° C) temperature. In addition, radiation was found to: lower the glass transition temperature (T_g) [3,7], and increase the energy dissipation under cyclic loading [7]. The primary degradation mechanism was shown to be degradation of the epoxy network structure and generation of low molecular weight products [4].

Sykes, and co-workers at NASA-Langley Research Center, have performed a number of studies on irradiation effects. Bowles, Tompkins, and Sykes [9-11] investigated the effect of radiation on the dimensional stability and CTE (coefficient of thermal expansion) of several graphite/resin composites. They found that permanent residual thermal strains were produced in irradiated (10,000 Mrad) Gr/Ep (T300/5208) after thermal cycling [9] and embrittlement and microcracking of an elastomer-toughened Gr/Ep (T300/CE339) at total doses of irradiation as low as 10 Mrad. The elastomer-toughened system (T300/CE339) was shown to be more sensitive to radiation-induced degradation than a similar "non-toughened" system [10].

Work done by Sykes and Slemp [12] showed that T300/CE339 experienced significant degradation of in-plane mechanical properties following irradiation. This makes the material unsuitable for use in precision space structures subjected to electron radiation.

A recent study by Funk and Sykes [13] showed that electron radiation increased the fracture toughness of T300/934. This study utilized both the edge delamination tension (EDT) and

double cantilever beam (DCB) tests. The results indicated that electron irradiation affected bulk matrix properties and did not significantly degrade the fiber-matrix interface.

It should be noted that all these studies [3-13] used irradiation procedures similar to those used in this report. The only difference was that some of the studies investigated the effects of varying the total dose. In these studies the radiation source and dose rate were the same as in this study, but the specimens received less than the 10,000 Mrad dose believed to be equivalent to 30 year space exposure. Other researchers have used different radiation sources, dose rates, and total doses. It is important to note these parameters when comparing the work of different researchers.

Milkovich, et al. [3] provided a rather extensive survey of the available literature on radiation effects in composites. To briefly summarize the results of this survey, it was found that: the total doses of radiation employed in research studies were often insufficient to simulate the long term ($>$20 years) effects of radiation, only a limited number of properties had been investigated, and many different, often conflicting, conclusions had been drawn. The trends in the data included the following: degradation was most significant at elevated temperature, glass transition temperatures were lowered, and there was little or no effect on fiber-dominated properties. The results of three other studies (conducted since the publication of Ref. 3) will now be described.

Work by Takeda, et al. [14] indicated that interlaminar shear and flexural properties of carbon cloth/epoxy (Torayc no. 6142 plain woven type/Sumiepoxy ELM-434, respectively) laminates were unaffected by electron irradiation up to total doses of 12,000 Mrad. The irradiation was carried out using a Dynamitron IEA-300-25-2 type electron accelerator and a dose rate of 1800 Mrad/hr. The interlaminar shear strength was measured using a method similar to ASTM D-2733 and the flexural properties were obtained in three-point bending.

Leung [15] investigated moisture absorption, dynamic mechanical properties, and interlaminar shear strengths in Gr/Ep (T300/934) subjected to gamma radiation. The radiation source was Co-60 and the irradiations were conducted at 77° F (25° C), 212° F (100° C), under vacuum, and in air for a total of four different conditions. The dose rate was approximately 0.257 Mrads/hr and four different total doses (up to 320 Mrad) were used.

From moisture diffusion measurements, Leung concluded that the matrix material was damaged and the fiber-matrix interaction was improved by radiation. The dynamic mechanical results, measured using a Rheovibron Dynamic Viscoelastometer (Model RHEO-200), indicated a decrease in the glass transition temperature and initial decrease, followed by moderate increases, in the flexural damping loss tangent (tan δ) as total dose increased. Short beam interlaminar shear strength (at room temperature) showed an initial increase and subsequent decrease with increasing total dose.

Maiden, Gounder, and Seehra [16] measured several physical and mechanical properties of an ultra-high modulus Gr/Ep material system (RCA-2606114). They measured properties at -300° F, 70° F, and 160° F (-184° C, 21° C, and 71° C, respectively) before and after simulated space environment conditioning. This conditioning consisted of both electron irradiation and thermal cycling. The material was irradiated with 12 MeV electrons at a dose rate of 300 Mrads/hr to a total dose of 300 Mrads. The thermal cycling was conducted between -300° F (-184° C) and 160° F (71 ° C) with a heating/cooling rate of 11° F/min (6° C/min). All materials were oven dried at 225° F (107° C) for 4 hours and the material which was exposed to the simulated space environment was oven dried again (225° F; 107° C; for 4 hr) after exposure. The properties measured in this study included: longitudinal and transverse tensile strength and modulus, in-plane (45° off-axis tension) and interlaminar (short beam) shear strengths, longitudinal and transverse coefficients of thermal expansion and moisture expansion (CTE and CME, respectively).

The greatest changes observed by Maiden, et al. [16] were in longitudinal tensile modulus and transverse tensile strength at cryogenic temperature and transverse tensile modulus and in-plane shear modulus at elevated temperature. In-plane shear strength was significantly reduced across the entire temperature range. CTE and CME properties were only slightly affected by exposure to the simulated space environment.

2.1.1 Observations on the Literature

The literature on irradiation effects on composites covers a wide range of irradiation procedures, measured properties, material systems, etc. The most common properties investigated are tensile modulus and strength, shear modulus and strength, and a variety of thermophysical properties (CTE, T_g, tan δ, etc.). When investigated, test temperature was shown to have a significant effect on the amount of radiation-induced degradation.

The interested reader is encouraged to consult the references mentioned in this section for details of the various experimental programs and results obtained. The studies surveyed are not an exhaustive list, but are believed to be representative of the recent work in the field.

2.2 Materials

2.2.1 Graphite/Epoxy Composite

The composite material used in this study, as in previous work [3-8], is T300/934 graphite/epoxy. This material has been approved for use in space by NASA. Thornel (Union

Carbide) T300 is an intermediate strength carbon fiber produced from a polyacrylonitrile (PAN) precursor. Fiberite 934 is a 350° F (177° C) cure epoxy and is representative of epoxies of this type. The material was obtained as unidirectional prepreg tape, HYE-1034C, from the Fiberite Corporation. Panel layup and processing were conducted at NASA-Langley Research Center according to manufacturers specifications. All compression specimens were cut from a single unidirectional 8-ply panel.

This panel was C-scanned to ensure integrity and samples of the panel were analyzed to determine void content, volatile content, fiber weight percent, and density according to ASTM Standard D3171-76 [17]. From this data and the densities of the constituent materials the fiber volume fraction can be calculated [17]. The results of these measurements and calculations are summarized in Table 1. These measurements were made on baseline and irradiated samples. There were differences in the specimens but it was unknown whether this difference was due to irradiation or simply reflected the "natural" variability of the material or the measurement process. The irradiated material seems to have a lower fiber weight and volume fraction than the baseline.

2.2.2 Neat Epoxy Resin

The neat resin tensile tests were conducted using Fiberite 934 epoxy resin provided by the Fiberite Corporation. The resin was supplied thoroughly compounded and mixed in 20-30% acetone solution. The resin was cast to the net shape of ASTM Type V tensile specimens (Standard Test Method D638-2a [18]) in silicone rubber molds.

This resin (Figure 1) is based on a tetraglycidyl epoxy (MY-720) cured with a diamine curing agent (DDS). A diglycidyl reactive dilutent (GLYCEL 100) is present--such dilutents are commonly added to decrease the viscosity of the uncured resin and allow easier processing. A

Table 1. Density and Volume Fraction Results for T300/934 Graphite-Epoxy

Property	Baseline	Irradiated
Fiber Weight Fraction, W_f	68.2%	66.6%
	70.5	67.9
Average	69.4	67.3
Volatile Content	0.1%	0.2%
	0.0	0.1
Average	0.05	0.15
Density (g/cm^3)	1.59	1.59
	1.61	1.60
Average	1.60	1.60
Fiber Volume Fraction, V_f	61.6%	60.2%
	64.5	61.7
Average	63.1	61.0

	Weight Percent
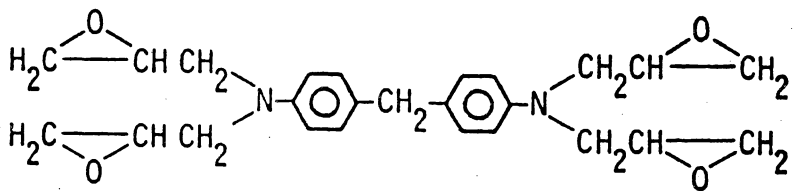 Tetraglycidylmethylenedianiline (MY-720)	64
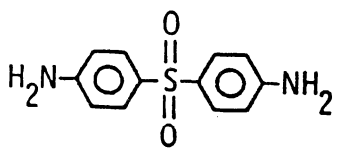 Diaminodiphenylsulfone (DDS)	25
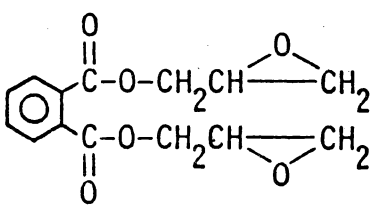 Diglycidyl orthophthalate (GLYCEL-100)	11
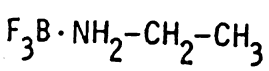 Boron Triflouride-monoethylamine complex (BF_3MEA)	0.4

Figure 1. Composition of Fiberite 934 Epoxy Resin

BF_3MEA complex is added as a semi-latent hardener. This is often done in laminating applications because it allows "cooking" of the resin and cooling to obtain a dry stable B-staged material [2]. Details of specimen processing and fabrication will be discussed in Chapter 5.

2.3 *Irradiation Facility and Procedures*

All radiation exposure was conducted in the Space Materials Durability Laboratory at NASA-LaRC. Specimens were firmly attached to an aluminum backplate (Figure 2) which was water-cooled during irradiation. The specimens were irradiated in three separate batches; two of which involved the composite compression coupons and a third for the neat resin tensile specimens. All irradiation was conducted under high vacuum ($2x10^{-7}$ torr).

The specimens were exposed to 1 MeV electrons at a dose rate of 50 Mrads/hr for 200 hours to yield a total dose of 10,000 Mrads. This translates to approximately two weeks of facility use. Dose rate and total dose were continuously monitored by a Faraday cup. Watercooling of the backplate and the chosen dose rate ensured that the temperature of the specimens was maintained $<$ 100° F ($<$38° C) [3]. The energy of the electrons is representative of those present in the Van Allan radiation belts and was sufficient to provide uniform thru-the-thickness exposure. The total dose is representative of 30 year, "worst-case", exposure in space.

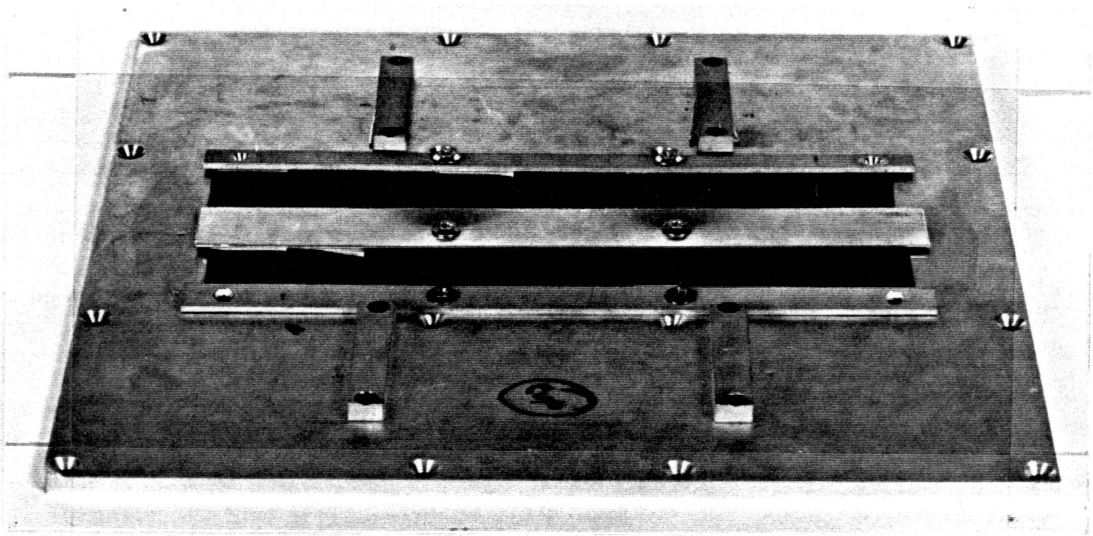

a) Composite Compression Coupons

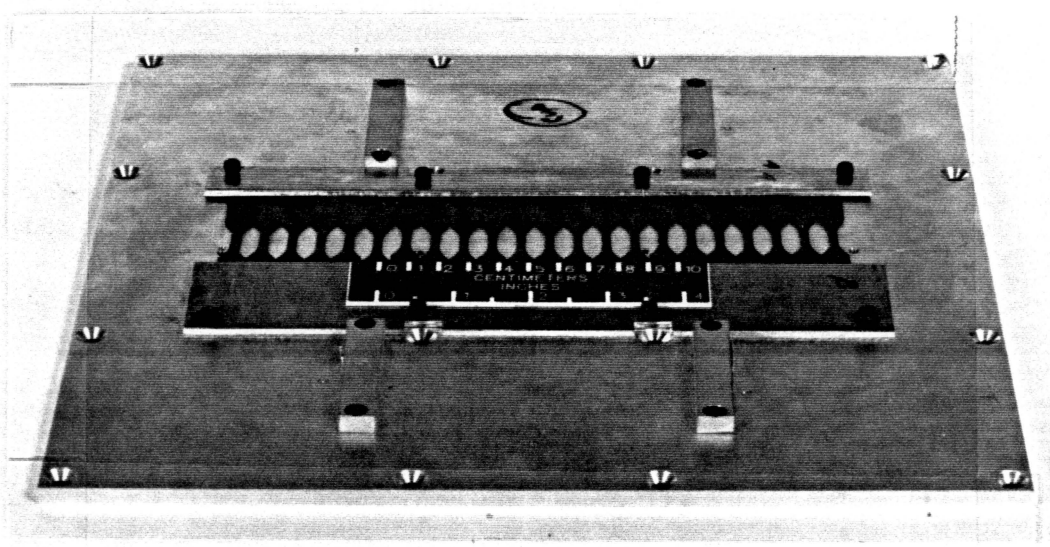

b) Neat Resin Tensile Specimens

Figure 2. Specimens Mounted on Plates for Irradiation

2.4 Dynamic Mechanical and Thermomechanical Analysis

One of the most frequently used measures of the effect of irradiation is the change in the second order transition or glass transition temperature, T_g. A second-order transition is defined as a change in the rate of volume change with respect to the temperature. Thermal agitation, which allows parts of the resin chain to rotate about its bonds, causes the transition. The T_g is useful in determining maximum use temperature and in characterizing the resin [2].

There are several methods which can be used to determine the T_g which include hardness tests, dilatometry, electrical resistance measurements, and dynamic-mechanical methods [2]. Because the molecular motions occur at specific rates the methods which load the material quickly tend to produce higher T_g values. Many of the tests yield useful information about molecular structure and motions which is as useful as the T_g itself [2].

2.4.1 Dynamic Mechanical Analysis

The DMA technique is based on the fact that the internal damping of the material greatly increases near the T_g. The shape of the damping vs temperature curve can be related to the molecular weight and crosslink density. The following general relationships are useful for interpreting DMA results: higher damping peaks indicate decreasing average molecular weight, rightward shifts (e.g. to higher temperatures) of the damping peak indicate higher crosslink density, and wider damping peaks indicate wider distribution of molecular weights.

Milkovich, et al. [3] used a DuPont 981 Dynamic Mechanical Analyzer and these relationships to determine the changes in the T300/934 material system due to electron irradiation. This instrument vibrates a small (1" by 0.5"; 25.4 mm by 12.7 mm) rectangular piece of the material

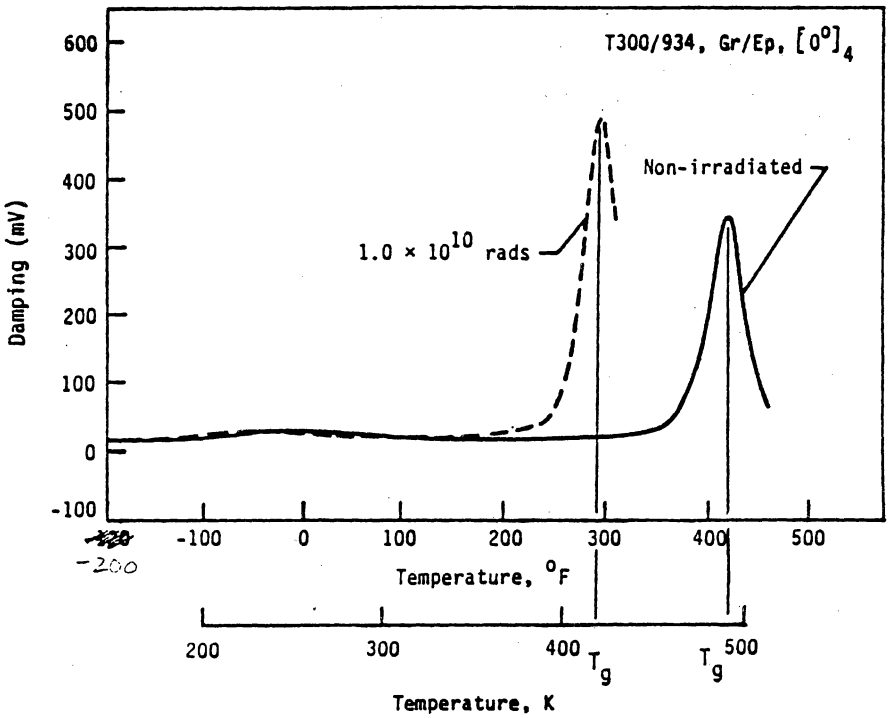

a) 0° Specimen

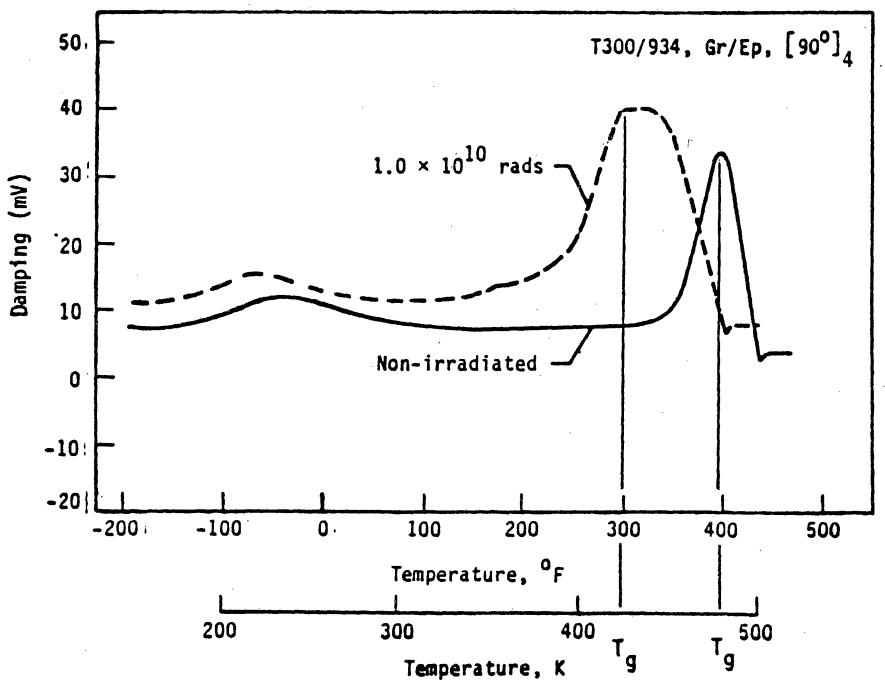

b) 90° Specimen

Figure 3. T300/934 DMA Results: (courtesy of Milkovich, Herakovich, and Sykes [3])

in flexure. The energy input required to maintain the oscillation at resonance as the temperature is varied can be related to the damping of the sample. Milkovich, et al. obtained the results shown in Figure 3 and in Table 2.

The lowering of the T_g and the higher damping peaks exhibited by the irradiated material (Figure 3) indicate that the average molecular weight and crosslink density were reduced by irradiation. The 90° specimen, which is more sensitive to matrix properties [7], also has a broader damping peak (Figure 3b). This implies that in addition to lowering the average molecular weight, irradiation also widens the distribution of molecular weights.

2.4.2 Thermomechanical Analysis

Composite Characterization: Thermomechanical analysis (TMA) is another method which can be used to determine the glass transition temperature (T_g). This method utilizes the large dimensional change which occurs near the T_g. This test also yields information regarding modulus changes, creep properties, and phase transitions [3,7]. The DuPont 942 Thermomechanical Analyzer was used by Milkovich, et al. [3] to obtain the results shown in Figure 4 and Table 2. This analyzer records the penetration of a hemispherically tipped probe into a small square (0.25″; 6 mm) sample of the material as a function of temperature. The expansion indicated near the end of the curve for the irradiated specimen was found to indicate blistering due to volatilization of low molecular weight products of irradiation. The results (Table 2) indicate that the softening point is lowered by about 100° F (50° C).

The TMA results correlate well with the DMA results. The DMA results indicated that irradiation tended to reduce the degree of cross-linking, lower the average molecular weight, and widen the distribution of molecular weights. All these effects suggest the formation of low molecular weight products and the TMA results confirm this hypothesis. It should be noted

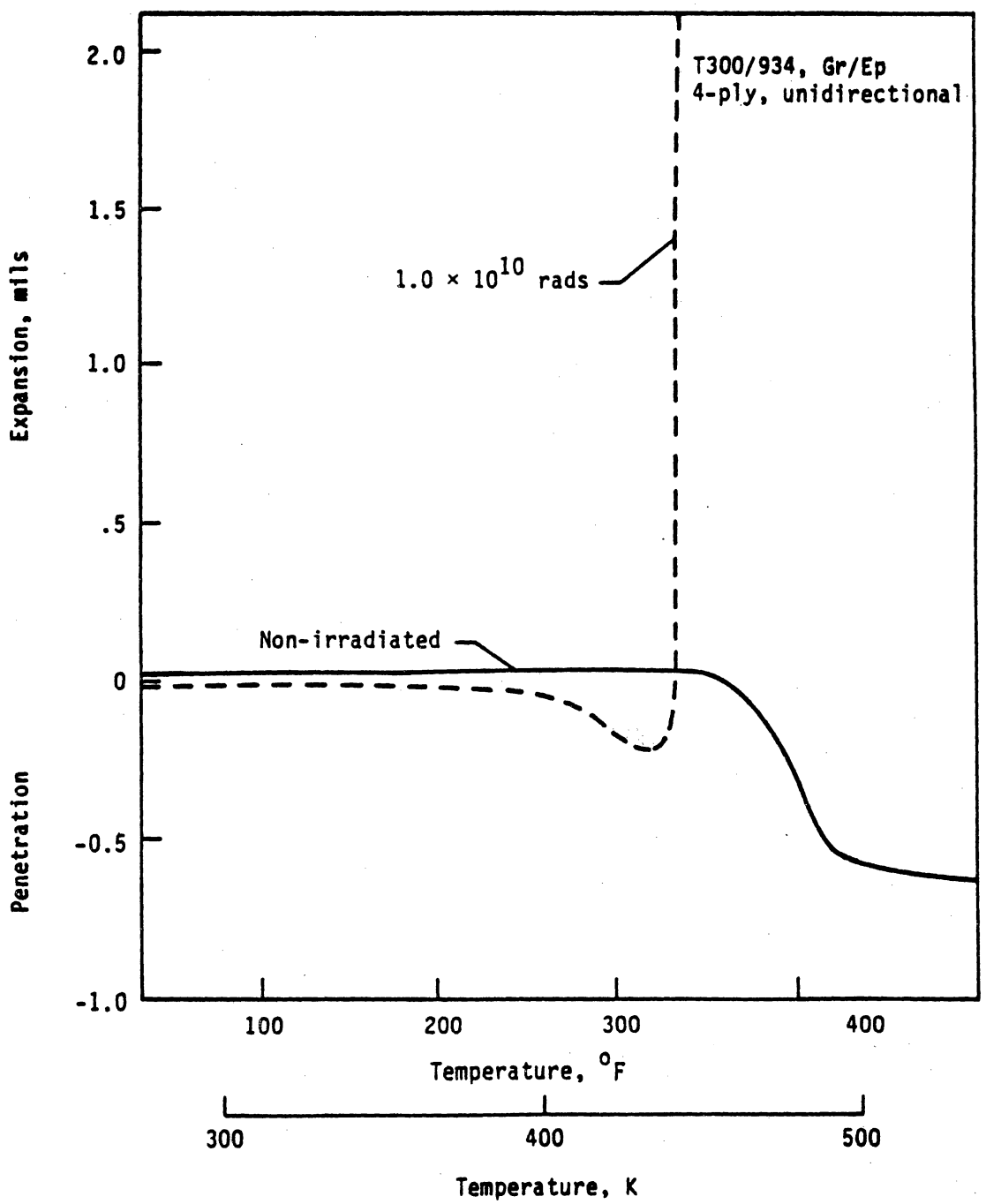

Figure 4. T300/934 TMA Results: (courtesy of Milkovich, Herakovich, and Sykes [3])

that Sykes, Milkovich, and Herakovich [3] have analyzed these products and found them to be fragments of the epoxy network structure. The subsequent work of Reed, et al. [7] showed that alterations to the epoxy chemistry could eliminate some of these low molecular weight products and cause a corresponding increase in the T_g in both the baseline and irradiated conditions.

During the course of the compression testing, to be discussed in the Chapter 4, the strain gages on the irradiated, elevated temperature, 90° specimens behaved peculiarly. It was impossible to maintain bridge balance at the elevated test temperature (250° F; 121° C). Because the strains were of relatively small magnitude (compared to those obtained during the mechanical test) and because of various factors associated with the level of initial preload, heating rate, specimen-to-specimen variability, etc. it was difficult to assess the cause of this effect.

The irradiated composite was very near the T_g (Figure 4) at the elevated test temperature (250° F; 121° C) and the material properties are highly temperature and time dependent in this region. In an attempt to more precisely define the above phenomena, it was decided to try a modification of the usual TMA test method. The usual method is to raise the temperature of the test specimen from room temperature to some elevated temperature (i.e. 900° F; 500° C) at a slow constant rate (9° F/min; 5° C/min) and record the probe penetration. In the modified procedure, the temperature was raised to 250° F (121° C) at 36° F/min. (20° C/min.) and then maintained (isothermal) for 1.5 hrs. Quite obviously, the material exhibits considerable time dependent deformation (Figure 5). It should be emphasized that the portion of the curve from point A to B was obtained while the material was at a constant temperature and very slight mechanical load (the mass of the probe and a 15 gram weight).

The results shown in Figure 5 complement the findings of Bowles, Tompkins, and Sykes [9] and Haskins [19] that permanent shrinkage occurs in the first thermal cycle during CTE measurements. The causes of this shrinkage remain undetermined and possible explanations

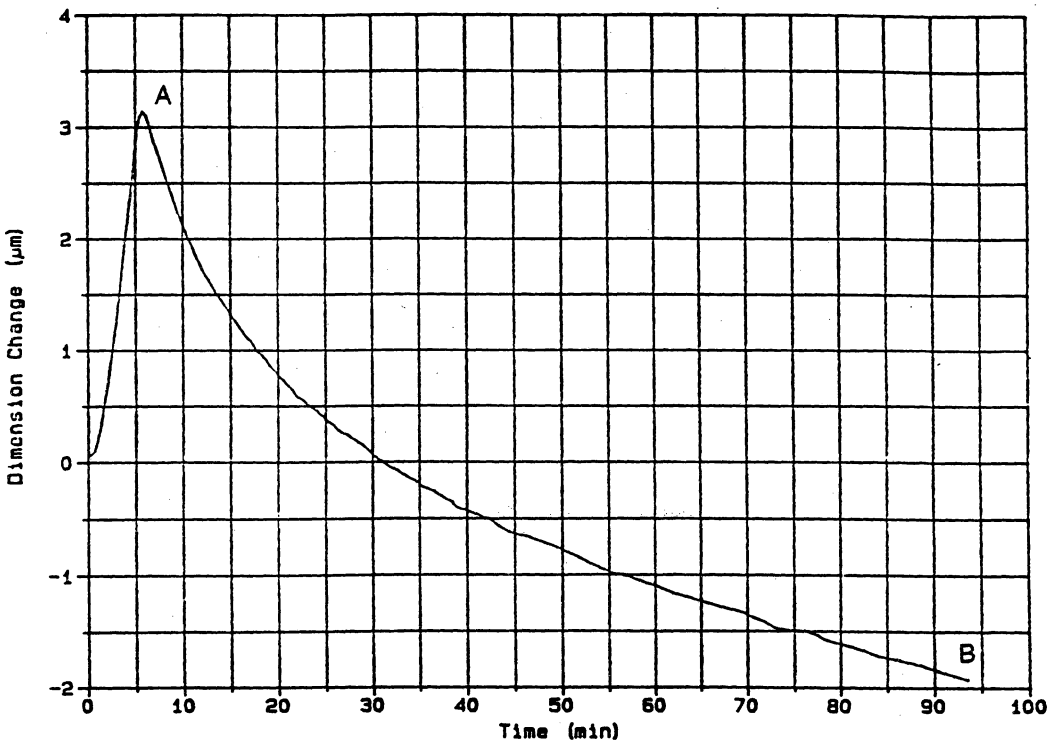

Figure 5. T300/934 TMA Results Using Modified Procedure

include: loss of volatiles (including water [19]) , changes in the epoxy chemical structure [9], and changes in the residual (curing) stress state. When the test method involves mechanical loads, as in the above TMA procedure, it is also possible that creep behavior occurs.

Neat Resin Characterization: The neat Fiberite 934 resin was also characterized using the standard TMA technique described above. The trends were similar to those observed in the composite (Figure 6, Table 2). The T_g was lowered by approximately 100° F (60° C) by irradiation. In the baseline material the elevated test temperature is clearly below the transition region, while after irradiation the material is clearly in the softening range at the elevated temperature.

The softening points of the baseline composite and neat resin materials are essentially the same. The softening point of the irradiated composite is approximately 50° F (30° C) lower than that of the irradiated neat resin. This is an indication that the material/radiation interaction may be different in the neat resin than in the composite.

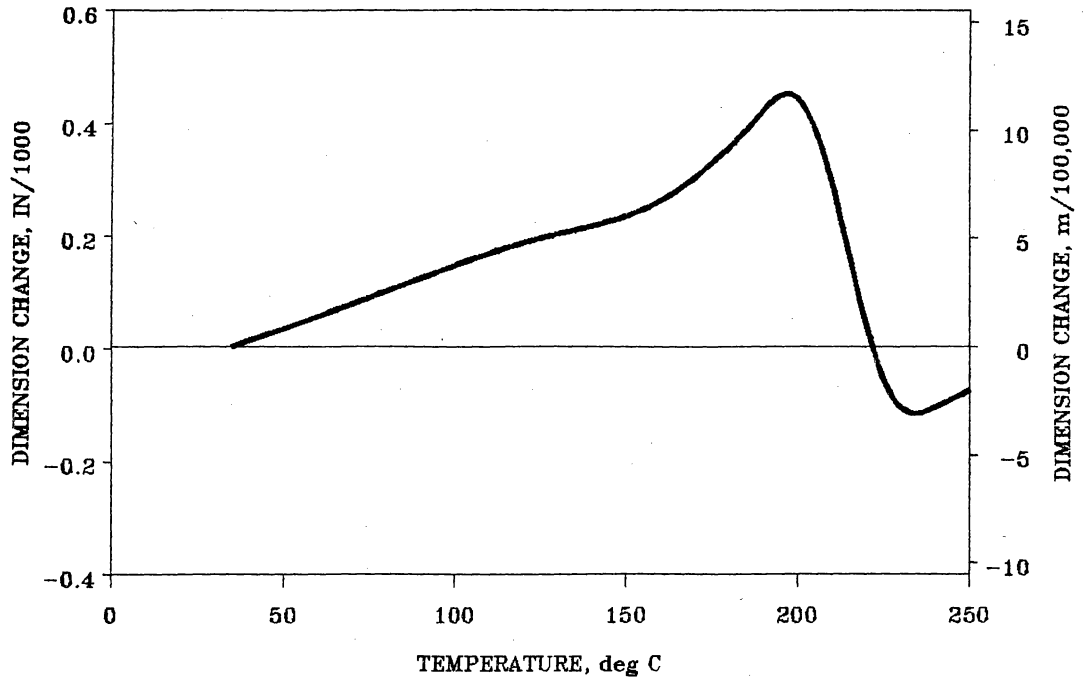

a) Baseline

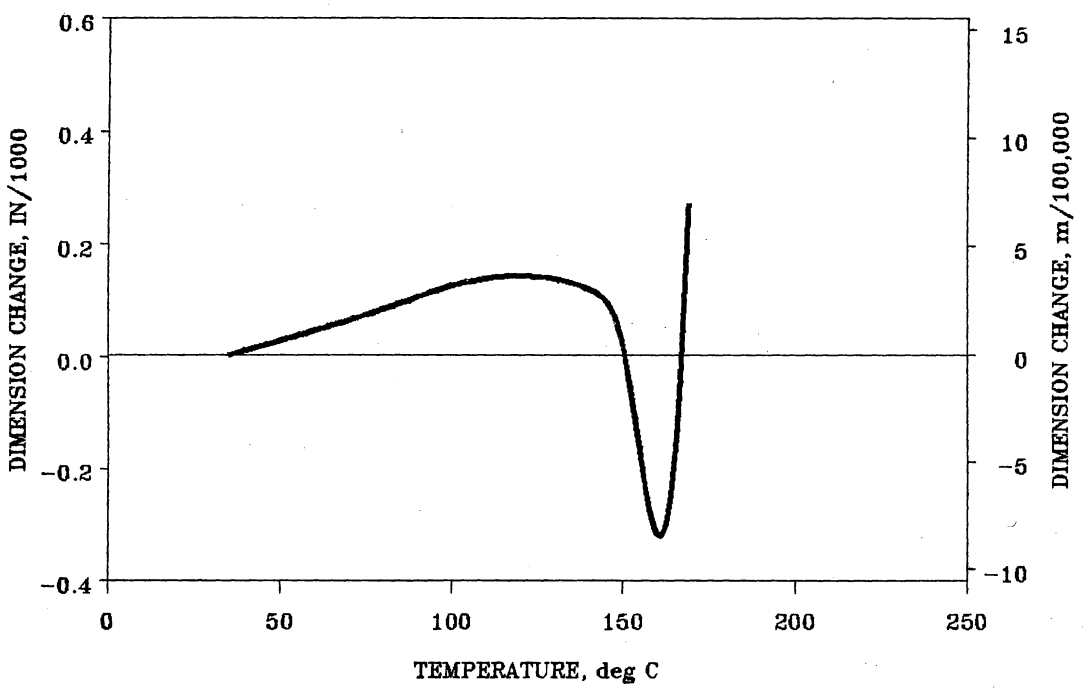

b) Irradiated

Figure 6. Neat Resin TMA Results

Table 2. Summary of TMA and DMA Results

T300/934 Composite*			
	Baseline	Irradiated	Δ%
Glass Transition Temperature, T_g	410° F (210° C)	300° F (149° C)	-27 (-29)
Beginning of Plastic Behavior	325° F (163° C)	175° F (79° C)	-46 (-51)

Fiberite 934 Epoxy			
	Baseline	Irradiated	Δ%
Beginning of Plastic Behavior	329° F (165° C)	223° F (106° C)	-32 (-36)

* Results of Milkovich, Herakovich, and Sykes [3]

3.0 Compression Testing

This chapter deals with one of the major thrusts of this study--the effects of temperature and irradiation on the compressive properties of Gr/Ep (T300/934). First, there is a brief overview of compression testing methods. The next section describes the features of the proposed test program which encouraged development of a new test method and an outline of the development process. Following this, the global buckling behavior of thin coupons is investigated analytically. Finally, the test procedure, instrumentation, and methods of data analysis are described.

3.1 Overview of Compressive Test Methods

As noted in the Introduction, it was decided to investigate the composite compressive properties because they are generally more matrix dependent than tensile properties. Indeed, Lee and Neville [2] state that for glass/epoxy, "...though no property can be considered as a general criterion for the resin formulation, compressive strength is probably the most sensitive of the tests". The increased matrix dependence under compressive loading often implies in-

creased nonlinearity (compared to tensile loading) in the stress-strain response and different properties (i.e. strength) in compression and tension.

Unfortunately, there are also difficulties encountered in compression testing of unidirectional composite materials. Tsai [20] stated compressive strength was "one of the most difficult properties to measure". The ideal compressive test method would satisfy the following requirements:

- Produce a uniaxial compressive stress state free of grip effects
- Forestall global instability (buckling)
- Use a simple test specimen
- Be easy to perform and analyze
- Yield consistent and accurate results

While it is difficult to satisfy all these criteria simultaneously, there are fixtures available which satisfy some of them. An exhaustive study of the fixtures available would be quite long and tedious, however, a brief description of some representative fixtures is worthwhile. The test fixtures can be classified by method of load introduction and by the techniques used to prevent premature buckling. The two principal methods of load introduction are shear introduction and direct loading. The techniques used to prevent premature buckling include the use of short test sections, "self-aligning" grips, supporting the non-loaded edges or faces of the coupon, etc.

The Celanese (ASTM Standard D3410 [21]) and the IITRI (modified Celanese) fixtures are probably the most widely used. These fixtures are very similar and apply load by shear introduction along the tabbed end of the specimen (Figure 7a). Buckling is prevented by the use of short gage sections and axial load application ensured by alignment pins in the fixture. The primary disadvantage of this fixture is associated with the necessity to tab the specimens. Besides the time and effort which must be spent in the tabbing operation, tab debond and

slippage can be substantial problems, particularly at elevated temperatures. Tab debonding acts to increase the effective Euler column length and may lead to premature buckling [22]. Measured strength values have also been shown to be sensitive to the flatness and parallelism of the tabs [23]. Principal advantages of these methods are the commercial availability of the test fixtures and widespread use---which facilitates direct comparison of experimental data.

Side- or face-supported fixtures (Figure 7c) restrain lateral displacement of the coupon edges or faces. The advantage is to raise the global buckling load and allow the use of longer gage length coupons. Potentially, this could be of particular value for off-axis compression tests. Unfortunately, buckling type failures are common in these fixtures and they generally produce "low" strength values. These type of fixtures may use either method of load introduction.

The final type of fixture to be considered is the end-loaded coupon type (Figure 7b). Direct load introduction is used and coupon sizes are generally quite small, especially since minimal grip region is required (compared to shear introduction specimens). Short thick specimens are used to prevent buckling. While it is often possible to eliminate tabbing the gripped section of the test coupon, direct load introduction requires the loaded surfaces of the fixture and the loaded edges of the specimen to be as flat and parallel as possible. There are numerous fixtures of this type.

For an excellent comparison and discussion of results from three test fixtures (Figure 7) the interested reader is referred to the report by Clark and Lisagor [23]. It is worth emphasizing that the above descriptions are very generalized. A plethora of different fixtures exists and are in use. Additionally, the fixture used by a particular researcher is likely to be determined by requirements specific to a proposed testing program (unusually thick or thin specimens, environmental exposure conditions, etc.). Two characteristics which should be present in virtually any experimental setup are: existence of at least one ball joint in the load train (to

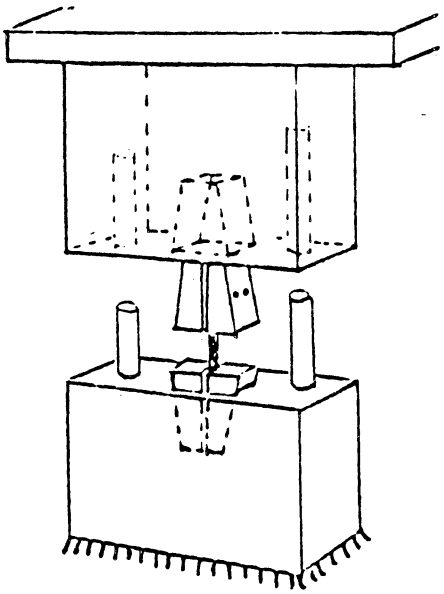

a) IITRI

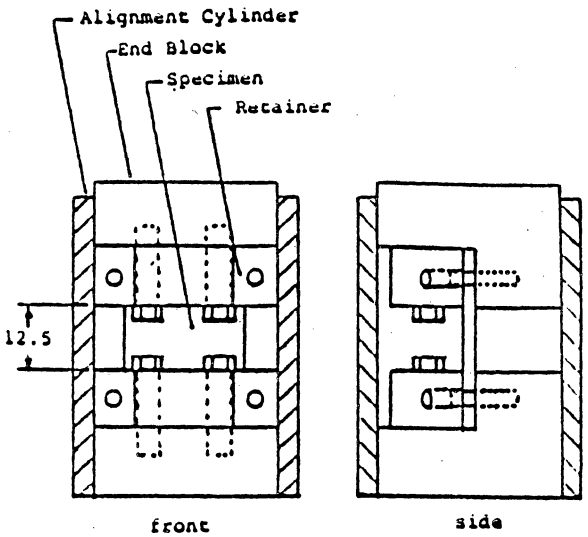

b) End-loaded Coupon

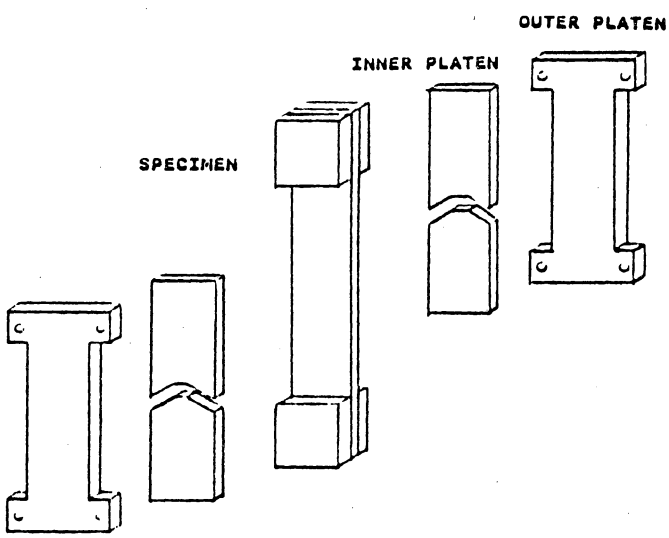

c) Face-Supported

Figure 7. Different Types of Compression Test Fixtures: (from Clark and Lisagor [23])

minimize applied moments) and reliable techniques to ensure axial load application (alignment pins, guide cylinders, wedge-shaped "self-centering" grips, etc.).

3.2 Test Method Development

As alluded to above, there were characteristics unique to the proposed test program which encouraged development of a different test method and which influenced the development process. Most significant of these was the necessity to limit the specimen thickness to eight plies. This was necessary to ensure uniform thru-the-thickness exposure, and to avoid overheating during, irradiation. The limited area which could be exposed during irradiation (10"; 254 mm; diameter circle) argued for a small compact specimen. The requirement to test at cryogenic (-250° F; -157° C) and elevated (250° F; 121° C) temperatures, as well as room temperature, suggested a fixture easily placed in and removed from the environmental chamber.

The highly anisotropic properties of unidirectional T300/934 formed yet another set of constraints. It was necessary for the fixture to be strong and rigid enough to withstand the forces involved in the 0° tests and yet not be so massive as to break or damage the 90° coupons during specimen mounting and positioning.

The development process began with a fixture being used at NASA-Langley Research Center to investigate thermal buckling behavior of thin laminates. Many of the basic features and the general overall appearance of this fixture remained intact throughout the development process. It was recognized, almost immediately, that elimination of premature buckling failure was the primary difficulty to be overcome. It was decided that room temperature longitudinal, "in-the-fiber-direction", strength would be the criterion by which success, or lack thereof, would be measured. This was done so that design changes could be evaluated quickly and

efficiently. It reduced instrumentation, data acquisition, and analysis needs to a minimum. From a perusal of the literature [20, 22-24], it was determined that consistent strength values in the 180 to 200 ksi (1200 to 1400 MPa) range would be acceptable for T300/934 graphite/epoxy.

Intrinsic to the existing fixture, or modifications made to it immediately were the following:

- All steel construction
- Direct load introduction with a portion of the coupon surface gripped
- Incorporation of a ball joint in the load train
- Loading eccentricity controlled by the tolerances between the slider and the guide cylinder and between the plunger and the top plate (Figure 8, Figure 9)

During the development process the size of the test (unsupported) section was reduced from 1″ (25 mm) to 0.125″ (3.2 mm) and expanded again to 0.25″ (6.4 mm), the overall coupon dimension shrunk from 1.5″ (38 mm) to 1.25″ (32 mm) and the portion of the coupon gripped grew from 0.25″ (6.4 mm) to 0.5″ (13 mm) at each end of the specimen.

Test method development began at Virginia Tech using a UTS screw-driven, displacement-controlled-type testing machine and unidirectional (0°) 8-ply T300/5208 material. It was felt that the differences between the Narmco 5208 and Fiberite 934 epoxy matrices would be negligible for fixture development purposes. During this period, winter and early spring 1986, the end grips were redesigned and the tolerance between the slider and guide cylinder was reduced from 0.002-0.003″ (0.05-0.08 mm) to 0.0005″ (0.013 mm). In the spring of 1986, reliable strength results of 180 ksi (1200 MPa) were being produced and fabrication and instrumentation of the T300/934 specimens began. It was also noticed that localized yielding of the steel slider had occurred in the contact region under the specimen. Rather than harden the entire piece and risk losing the close tolerance with the guide cylinder, a slot was cut into the piece and a hardened steel insert was pressed into the slot.

Subsequently, testing was resumed at NASA-LaRC in June, 1986 on a hydraulic MTS machine with a 100 kip (450 kN) load frame and with T300/934 specimens. Some difficulties were encountered in positioning the fixture in the test machine, although these were rapidly overcome. It was found that insufficient force had been used in pressing the steel insert into the slider, as it was pushed farther into the piece by initial checkout tests. The slider was surface ground flat and level to correct this problem.

More vexing than either of these problems was an unexpected tendency of the T300/934 specimens to crush, near the loaded edges, within the grip section. Such failures were very rare with the earlier T300/5208 specimens and considerable effort was expended to eliminate them with the T300/934 specimens. It was noticed that one pair of end-grips was slightly deformed and a new set was made of a harder material, but this failed to eliminate the problem. Again, it should be noted that longitudinal compressive strength was the only criterion for "success".

With some reluctance, it was decided to try tabbing the 0° coupons. It was felt that the additional support from the tabs would prevent the bearing-type failures. Because of the limited space available in the fixture, thin (0.020"; 0.5 mm) steel tabs were used. These tabs were found to be somewhat effective. Tab debond, followed by failure in the grip region, was initially encountered. Eventually this problem was overcome, by improving the tab bonding procedure, and although tab debonding still sometimes occurred at failure, the fracture surface was generally outside the grip region and the strength values were at an acceptable level ($>$180 ksi; $>$1200 MPa).

Checkout tests were run at elevated and cryogenic temperatures to verify that the fixture didn't bind or freeze-up. The fixture was heated, disassembled, to 250-300° F (120-150° C) and assembled, hot, several times. No difficulties were encountered. It was impossible to do the same at cryogenic temperatures for two reasons: the environmental chamber would be damaged by opening it and contact with the moist air would cause immediate icing. Visual

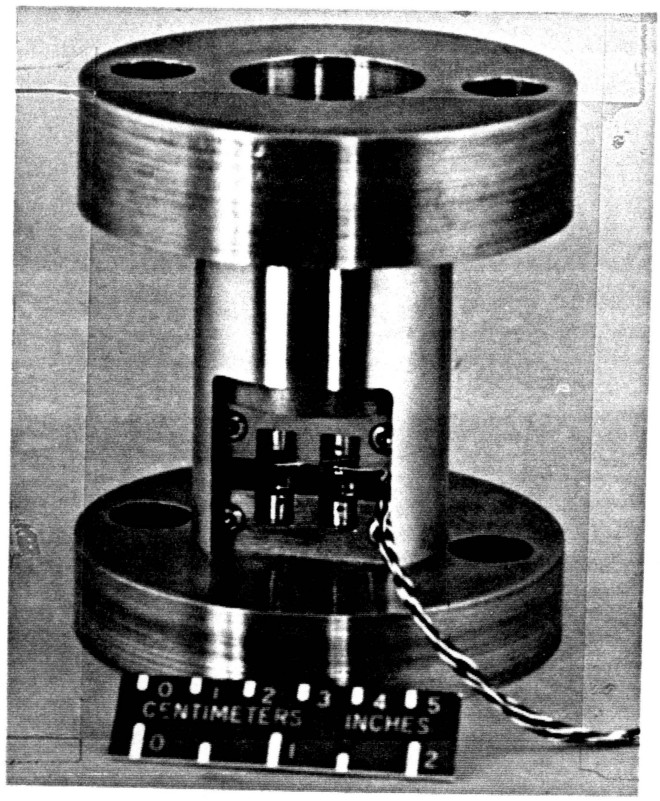

a) Assembled

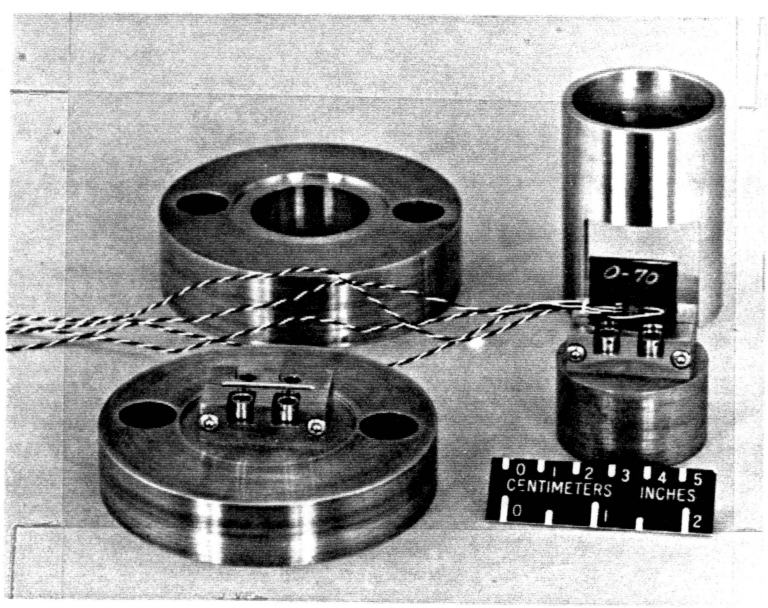

b) Disassembled

Figure 8. Compression Test Fixture

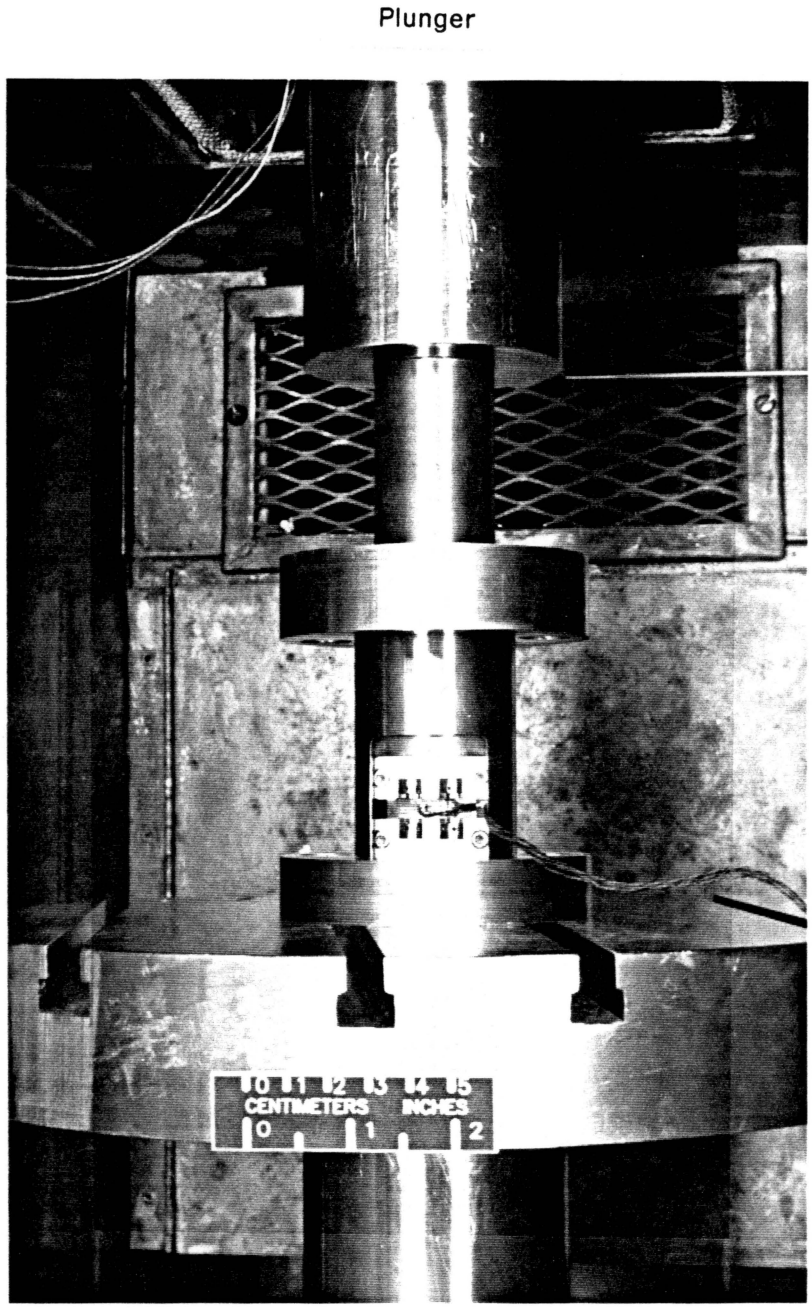

Figure 9. Compression Fixture Prepared for a Test

examination of the test fixture at cryogenic temperature revealed minimal frost accumulation during cool-down. No indications of icing were noticed during testing. In addition, uninstrumented specimens were tested at elevated and cryogenic temperatures. The strength values followed the expected trends qualitatively and quantitatively.

3.3 *Buckling Analysis*

In any situation where axial compressive loads are being applied instability phenomena must be considered. As mentioned in the last section, elimination of global buckling was one of the difficulties encountered during test method development. As a part of this work, the global buckling load was calculated for a variety of support conditions. It was found that the Euler column formula provides an excellent measure of the buckling load for the specimen geometry in this test. Analyses which take into account the widthwise or "plate" effects were investigated and found to yield results only slightly different from the simple column formula. The choice of support conditions has a significant influence on the value of the critical load. The mathematical models allow two conditions--simple support, wherein the ends of the specimen are restrained from lateral deflection but are free to rotate, and fixed support, wherein the specimen ends are restrained from both lateral deflection and rotation. Actual boundary conditions are likely to be less ideal, although probably closer to the latter (e.g. fixed conditions).

All the analyses which follow used the following properties:

$E_1 = 18.9$ msi $\qquad \nu_{12} = 0.314$

$E_2 = 1.38$ msi $\qquad G_{12} = 0.688$ msi

These are the values measured for the T300/934 baseline material at room temperature by Milkovich, et al. [3].

3.3.1 Simply Supported

The derivation of the buckling load for Euler columns can be found in many texts in strength of materials and virtually every text on elastic stability. The following result is used without proof:

$$P_{cr} = \frac{\pi^2 EI}{L^2}$$

where E is Young's modulus, I is the moment of inertia, and L is the length of the column (Figure 10a).

For a thin rectangular specimen, of thickness, t, the buckling criterion, in terms of the critical stress, is:

$$\sigma_{cr} = \frac{\pi^2 Et^2}{12}\left(\frac{t}{L}\right)^2$$

The stability of a plate simply supported on the loaded edges was considered by Ashton and Whitney [25]. The out-of-plane displacement is assumed to be of the form:

$$w = f(y) \sin \frac{m\pi x}{L}$$

A solution for the stability criterion can be found if:

$$f(y) = Ae^{-\alpha y} + Be^{\alpha y} + C\cos(\beta y) + D\sin(\beta y)$$

where α and β are

$$\alpha = \frac{m\pi}{a}\left[\left[\left(\frac{D_{12} + D_{66}}{D_{22}}\right)^2 - \frac{D_{11}}{D_{22}} - \frac{N_x}{D_{22}}\left(\frac{L}{m\pi}\right)^2\right]^{1/2} + \frac{D_{12} + 2D_{66}}{D_{22}}\right]^{1/2}$$

$$\beta = \frac{m\pi}{a}\left[\left[\left(\frac{D_{12} + D_{66}}{D_{22}}\right)^2 - \frac{D_{11}}{D_{22}} - \frac{N_x}{D_{22}}\left(\frac{L}{m\pi}\right)^2\right]^{1/2} - \frac{D_{12} + 2D_{66}}{D_{22}}\right]^{1/2}$$

the D_{ij} terms are elements of the bending stiffness matrix and N_x is the x-direction stress resultant.

In general, the constants A, B, C, and D are found by satisfying the boundary conditions on the unloaded edges ($y=0$; $y=W$). This results in a set of homogeneous equations and the critical stress resultant, N_x, is found by setting the determinant of this set equal to zero and minimizing N_x. Applying this technique to the case where the unloaded edges are free, the minima is found for the trivial case $\alpha=\beta=0$, yielding:

$$N_x = D_{11}\left(\frac{m\pi}{L}\right)^2$$

and since,

$$D_{11} = \frac{E_1}{1 - \nu_{12}\nu_{21}}\left(\frac{t^3}{12}\right)$$

$$N_x = \frac{E_1}{1 - \nu_{12}\nu_{21}}\ \frac{t^3}{12}\left(\frac{m\pi}{L}\right)^2$$

The minimum is obtained for $m=1$. The equation written in terms of stress becomes:

$$\sigma_{cr} = \frac{\pi^2 E_1}{12}\left(\frac{t}{L}\right)^2 \frac{1}{1 - \nu_{12}\nu_{21}}$$

This is similar to the column formula and for T300/934 Gr/Ep the difference between the two is $< 1\%$.

3.3.2 Clamped Support

The critical load for an Euler column under clamped (fixed) end conditions is easily obtained using the effective length concept. For a fixed-fixed condition, $L_{eff} = \frac{L}{2}$,

$$P_{cr} = \frac{\pi^2 EI}{(L/2)^2}$$

$$\sigma_{cr} = \frac{\pi^2 E}{3}\left(\frac{t}{L}\right)^2$$

or four times the simply supported value.

Unfortunately, the plate solution is not as easy to obtain. Ashton and Whitney [25] considered the stability of symmetric plates using the Ritz method. The stability criterion is satisfied for stationary values of the following functional:

$$\frac{1}{2}\int_0^a \int_0^b \left[D_{11}\left(\frac{\partial^2 w}{\partial x^2}\right)^2 + 2D_{12}\left(\frac{\partial^2 w}{\partial x^2}\,\frac{\partial^2 w}{\partial y^2}\right) + D_{22}\left(\frac{\partial^2 w}{\partial y^2}\right)^2 + 4D_{66}\left(\frac{\partial^2 w}{\partial x \partial y}\right)^2 + N_x\left(\frac{\partial w}{\partial x}\right)^2 \right] dy dx$$

The out-of-plane displacement, w, is assumed to be of the form,

$$w = \sum_{i=1}^{m}\sum_{j=1}^{n} a_{ij}\varphi_i(x)\psi_j(y)$$

where φ_i and ψ_j are the characteristic shapes of beams in free vibration. By using the appropriate beam functions, any of the classical boundary conditions (free, simply supported, or clamped) can be applied to any edge. Substitution of the assumed form of the displacement into the above functional and minimization using the techniques of the calculus of variations yields a set of linear homogeneous equations. This set of equations forms an algebraic

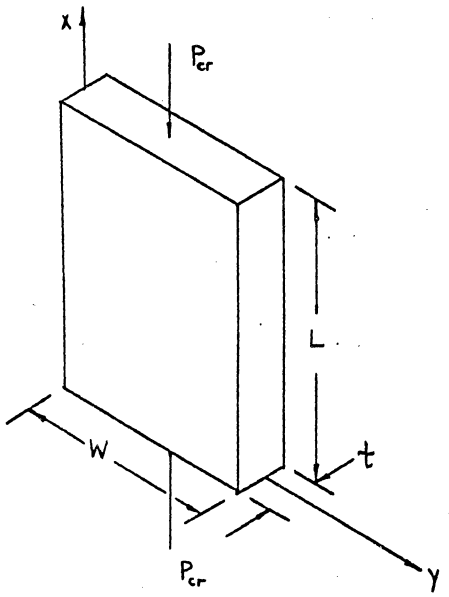

a) Specimen with Perfect Geometry and Loading Conditions

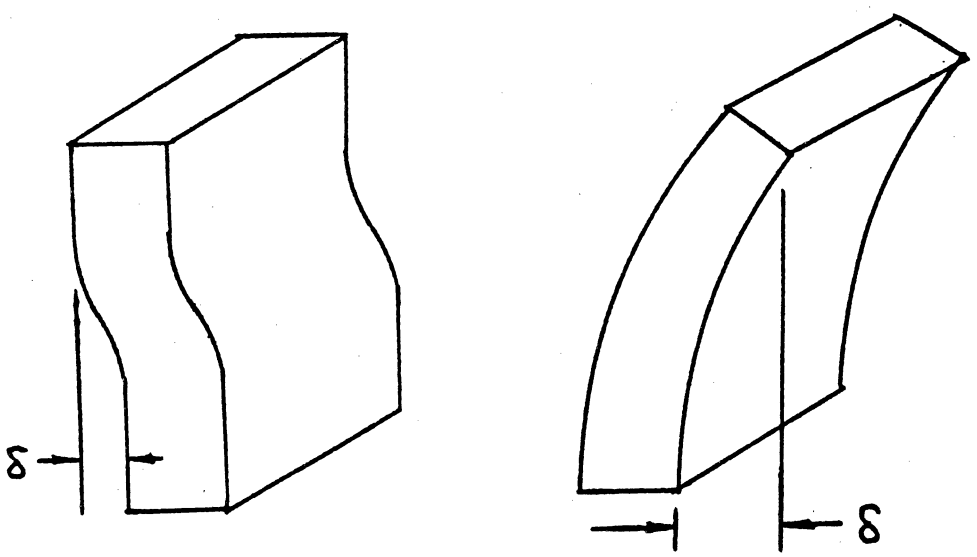

Lateral Displacement

Cantilever Displacement

Types of Eccentricity

Figure 10. Geometry Used in Buckling Analysis

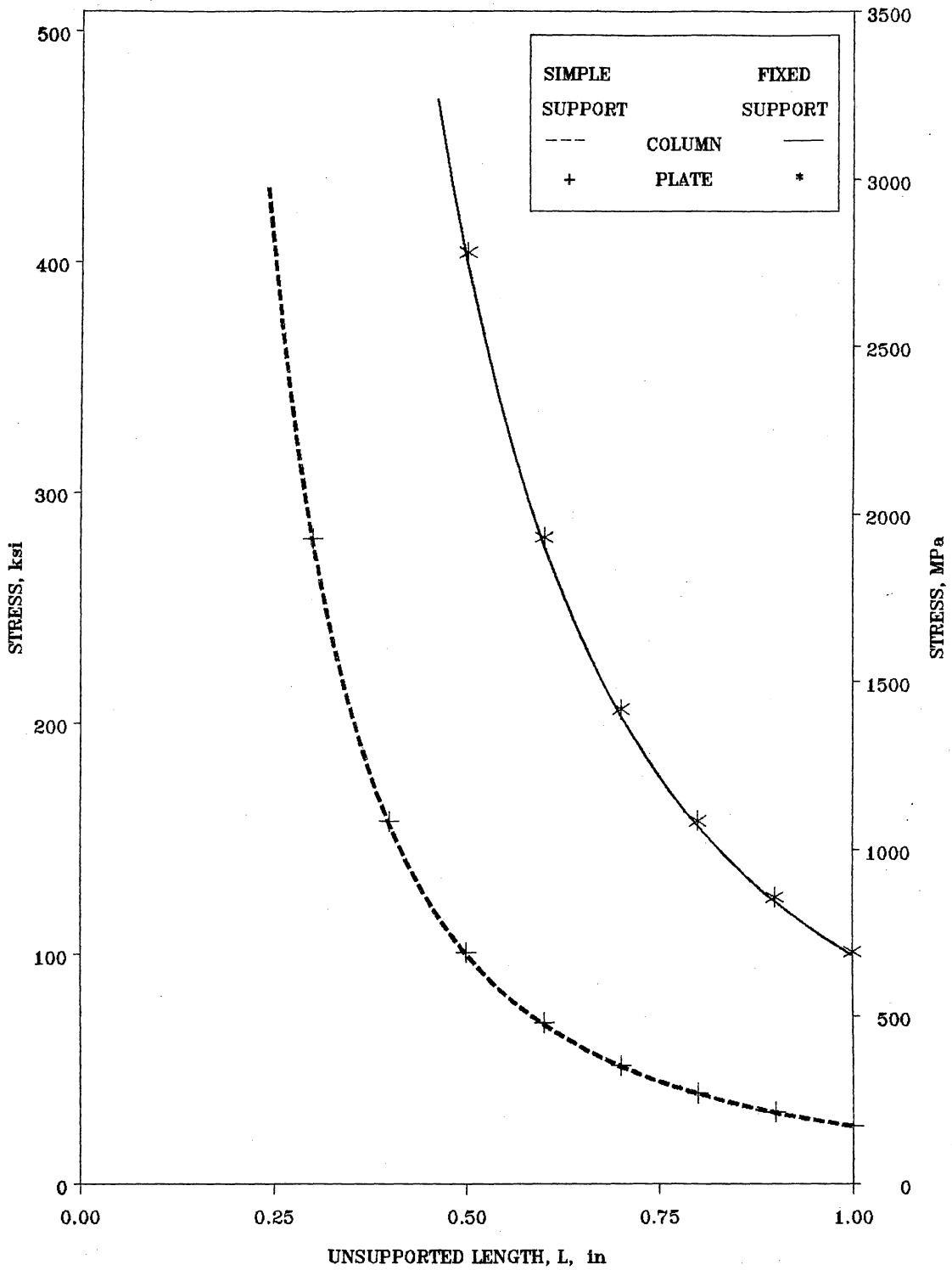

Figure 11. Buckling Load vs Unsupported Length

eigenvalue problem where the lowest eigenvalue corresponds to the buckling load and the corresponding eigenvector describes the buckling mode.

The details of this method are described by Ashton and Waddoups [26] and Ashton [27]. It should be noted that this is quite a general approach and this method can be used to investigate any midplane symmetric plate. The results of this analysis were found to be similar to those obtained from the column formula (Figure 11).

3.3.3 Effect of Eccentricities

All the analyses in the preceding sections have assumed perfect geometry and loading conditions. A more realistic analysis would include consideration of geometrical imperfections and load eccentricities. Generally speaking, these effects reduce the critical load, cause bending to occur throughout the load history (e.g. there is no sharp bifurcation point), and may change the buckling mode.

Chamis and Sinclair [22] investigated the effect of two types of eccentricities, which they denoted "cantilever-type" and "lateral-type" displacement (Figure 10b). They analyzed an ITTRI specimen, so the geometry of the problem was somewhat different and some of their specific conclusions probably do not apply to the present case. However, some of their findings are likely to be generally applicable. One of the most interesting results of their analysis was for the lateral-type displacement. They found that the buckling mode changed for this type of imperfection. In all the analyses mentioned thus far, including the cantilever-type displacement, the buckling mode has had a crest at the midspan (L/2) location. For the lateral displacement eccentricity, the mode shift produced buckling crests at the 1/4 and 3/4 span and a node at the midspan locations. Thus, noted Chamis and Sinclair [22], "back-to-back strain gages located at specimen midspan may not pick up out-of-plane bending...". They found that

the type of eccentricity had no effect on the buckling load. Additionally they found that twisting (plate) type buckling modes were observed for the specimen geometry they analyzed.

3.4 Specimen Preparation and Instrumentation

All composite compression coupons were cut from a single 8-ply (nominal thickness 0.040 in.; 1 mm) unidirectional panel at NASA-LaRC. The loaded edges of the coupons were flat and parallel to within 0.001″ (0.03 mm). The thickness was found to be irregular, typically varying 0.001-0.002″ (0.03-0.05 mm) across the coupon width, although variations of up to 0.008″ (0.2 mm) were found.

3.4.1 Tabbing Procedure

All 0° coupons were tabbed in an effort to prevent end-crushing failures. The tabs were 0.020″ (0.5 mm) thick steel and cover the entire gripped region. The adhesive used was Dexter-Hysol EA934 mixed according to manufacturers instructions with 5% (by weight) glass microspheres added to control bond line thickness. The tabbing procedure is as follows:

- Grit-blast the tab and composite bonding surfaces
- Prime the steel surface with BR127 Primer (a 10% solids epoxy/phenolic primer from the American Cyanamid Company) and allow to dry
- Carefully weigh out adhesive components and mix thoroughly
- Spread a thin layer of adhesive on the composite and tab surfaces
- Position tabs on composite coupon
- Clamp in jig and allow adhesive to cure for minimum of 24 hours at room temperature

- Remove excess adhesive and finish the loaded edges to within 0.001″ (0.03 mm)

3.4.2 Instrumentation

All compression coupons were instrumented with electrical resistance strain gages. All gages were located over the geometric center of the test coupon. One side of the specimen contained a three element rectangular rosette (Micro-Measurements WK-06-030WR-120) and the other side contained a single longitudinal ("in-the-load-direction") gage (Micro-Measurements SK-06-050AH-350).

Due to difficulties in obtaining the rosettes from the manufacturer, some specimens were instrumented with three single gages (Micro-Measurements SK-06-050AH-350) stacked in a rectangular rosette pattern. The term "stacked" is literally true, the single gages were physically placed on top of each other. Because it was possible to see the alignment marks thru the gage backing, the orientations of the grids could be accurately controlled. In the remainder of this report, rosettes fabricated in this fashion will be referred to as "stacked" rosettes and rosettes obtained from Micro-Measurements as such will be referred to as "factory" rosettes.

All gages were bonded using Micro-Measurements AE-15 Strain Gage Adhesive. This is a two component epoxy adhesive and was cured at 120° F (49° C) for six hours under 15 psi (103 Pa) pressure. Typical instrumented specimens are shown in Figure 12.

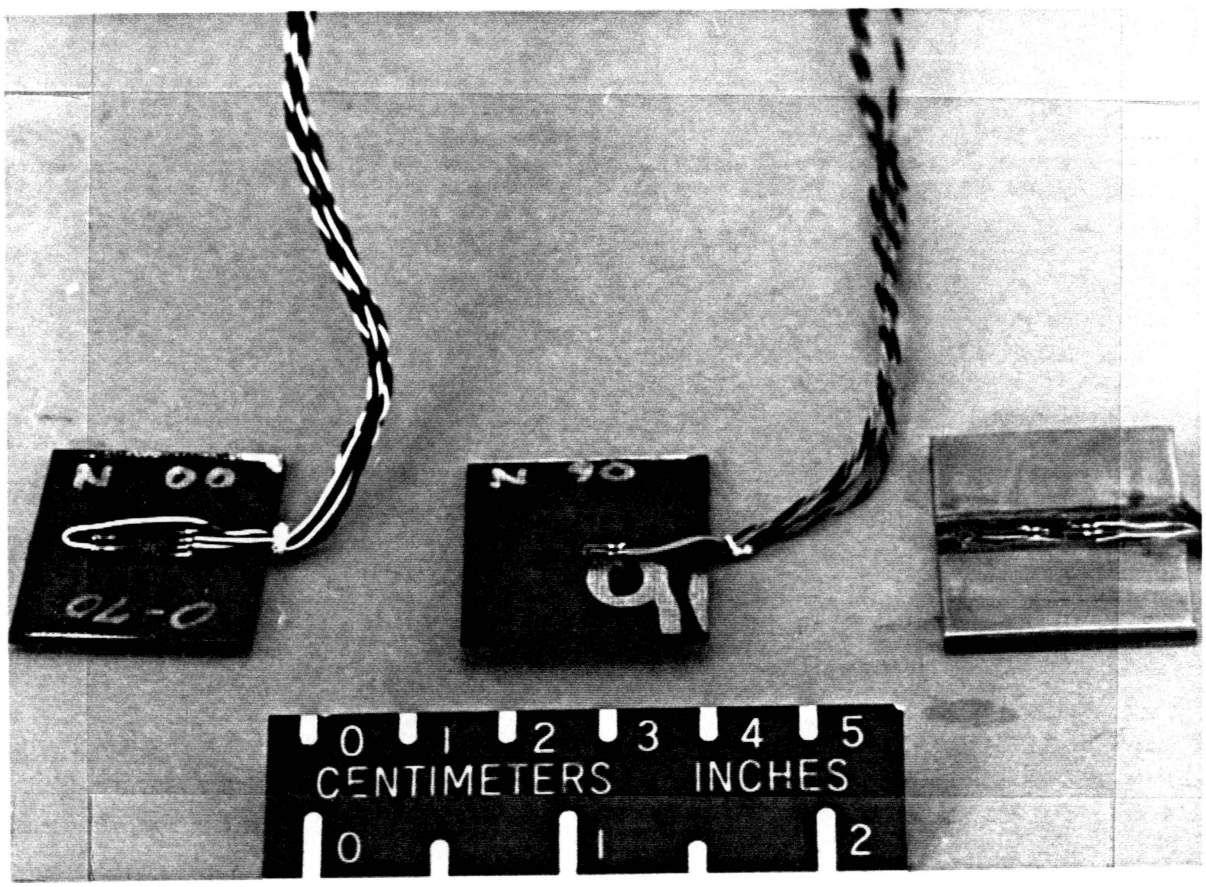

Figure 12. Typical Instrumented Compression Coupons

3.5 Testing and Data Acquisition Equipment

All compression tests were conducted at NASA Langley Research Center (LaRC) on a MTS 810 Material Test System with a 100 kip (450 kN) load cell (Figure 13b). Tests were conducted under stroke (displacement) control at a load rate of 0.0136 in/min (0.35 mm/min).

Strain gage and load cell data were acquired using an Hewlett Packard HP-236 computer and associated signal conditioning equipment (Figure 13a). The strain gages were connected to a constant voltage Wheatstone bridge circuit with a three-leadwire system.

A BEMCO Co. environmental chamber mounted in the load frame was used to perform the cryogenic and elevated temperature testing (Figure 13b). This chamber uses electrical resistance heating elements and liquid nitrogen for cooling. The load cell is located entirely outside the environmental chamber and was not exposed to the temperature extremes.

3.6 Specimen Mounting and Testing Procedure

The test procedure can be conveniently divided into three activities: (1) mounting the instrumented specimen in the test fixture, (2) positioning the fixture in the testing machine, and (3) performing the mechanical test. Each of these steps will be described in some detail.

Prior to mounting the specimen in the test fixture the width and thickness of the specimen was measured and recorded. In addition, the loaded edges of the coupon were checked for flatness and parallelism. The slider and the upper grip were then removed from the fixture, the coupon was placed in the upper grip, and the side screws were tightened. The upper grip

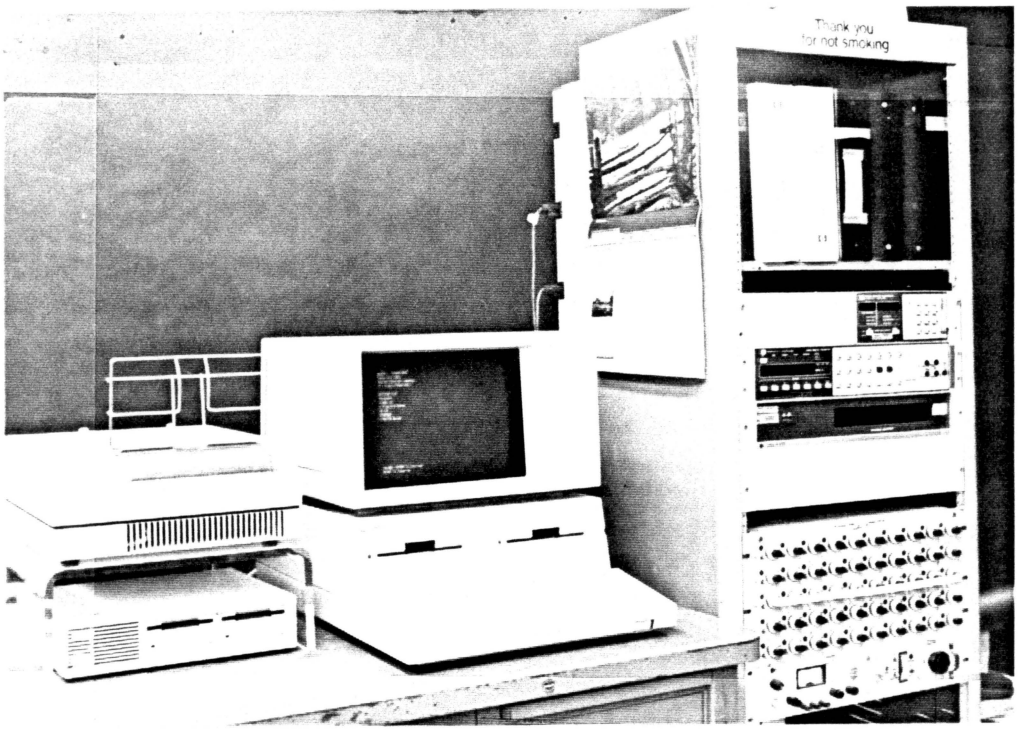

a) Data Acquisition and Signal Conditioning Equipment

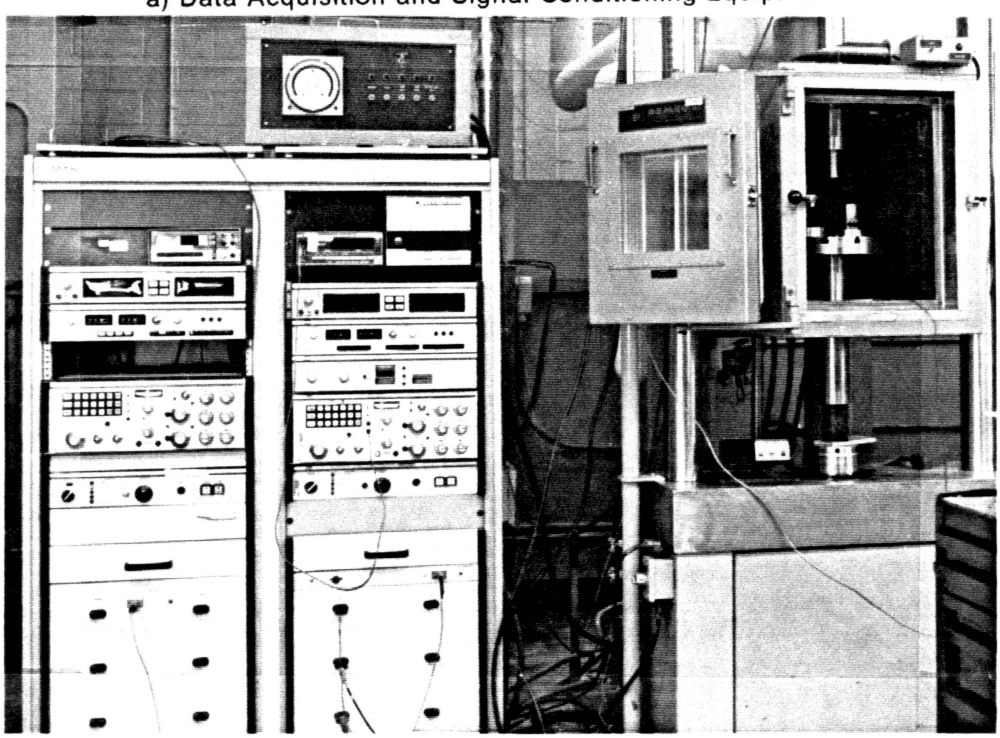

b) Testing Machine and Load Frame

Figure 13. Equipment Used for Compression Testing

(and coupon) was then visually aligned with centering marks permanently inscribed on the slider. Use of a lamp with a built in magnifying lens facilitated accurate and consistent alignment. The end screws were then tightened. The alignment was checked and this process repeated until the grip was centered on the slider. The slider was then placed in the guide cylinder and the guide cylinder on the baseplate (with attached lower grip). Once the specimen was firmly seated against the baseplate, the side screws in the lower grip were tightened. The guide cylinder was then gently rotated and the lower grip moved slightly until the guide cylinder rotated freely and didn't bind against the slider. The end screws on the lower grip were then tightened. The guide cylinder was then checked for binding and this process repeated, as necessary. This final step was the most difficult and required the most judgement and experience.

The entire process of specimen mounting was eased if the fixture was spotlessly clean. After a test, there would generally be small bits of graphite, epoxy, adhesive, etc. on the fixture. In addition, dirt and oils can be transferred from one's hands to the closely mating surfaces of the guide cylinder and slider. All this detritus and grease should be removed following each test. It was unnecessary to lubricate the guide cylinder, although this could have been done if desired (assuming the lubricant was suitable for the test temperature).

The positioning of the test fixture in the testing machine was a relatively simple process. The top-plate was slid up onto the plunger, the fixture was placed on the steel platen, and slid under the plunger. After making sure that the ball bearing was in position, the top plate was lowered onto the guide cylinder until it was firmly seated. The fit between the plunger and top plate, the slider and the guide cylinder, and the bearing seats in the plunger and slider all helped ensure axial alignment of the load train. The hydraulic ram of the testing machine was then raised until slight load was registered. The ram was subsequently lowered so that the test would begin under minimal preload (e.g. the weight of the fixturing). The strain gage leads were attached to the data acquisition equipment and the strain gages were balanced.

The coupon was now fully prepared for a room temperature test. The test fixture, with an instrumented specimen mounted, is shown in Figure 9.

3.6.1 Elevated Temperature Tests

Tests at other than room temperature called for a few modifications of the previously described procedure. For elevated temperature tests, the environmental chamber was heated until the metal platen reached a temperature of 270-280° F (130-140° C) before the fixture was placed in the chamber.

This was done in order to minimize the amount of time the test coupon was exposed to elevated temperature before testing. Initial heating of the chamber from ambient conditions required 2-2.5 hours. Using this procedure, the test fixture and coupon could be brought to a stable 250° F (121° C) temperature in 20-30 minutes from insertion in the chamber. Following testing, the chamber could immediately be opened and the fixture removed. The fixture could then be disassembled, the broken specimen removed, the fixture cooled, and another specimen mounted while the chamber remained at elevated temperature.

3.6.2 Cryogenic Temperature Tests

For the cryogenic temperature tests the fixture was positioned in the chamber (after specimen mounting) at ambient conditions. The chamber was then cooled, the test conducted, the chamber warmed, and the broken specimen removed. Cooling of the chamber required approximately 3 hours. It was extremely important that the fixture be grease- and moisture-free before conducting a cryogenic test. FREON was found to be adequate to remove most contaminants. The slight overpressure of the liquid nitrogen prevented infiltration, and subse-

quent icing, by the humid outside air, but any moisture on the test fixture (especially between the slider and the guide cylinder) was obviously undesirable. The warming of the chamber was necessary to avoid damaging it by thermal shock. It had to be brought to near ambient conditions to remove the large accumulation of frost which occurred during warm-up.

3.6.3 Temperature Monitoring

During elevated and cryogenic temperature tests, the temperature was monitored on the ends of the upper and lower grips with K-type thermocouples. During testing the temperature difference between the two locations was $<3°$ F ($<2°$ C). Mounting of the thermocouples on the specimen, while desirable, was impractical due to the small amount and relative inaccessibility of available space. It was felt that the temperature of the specimen would lie very near the temperature of these two nearby locations. The room temperature tests were conducted at ambient conditions and no attempt was made to control temperature.

3.7 Data Reduction and Analysis

The data from the compression tests were acquired in the form of raw voltage readings. Data points were acquired every 1-2 seconds and 30-100+ data points were acquired in a typical test. A peak-reading voltmeter was used to record the maximum (failure) load voltage. The data reduction and analysis procedure consisted of the following steps for each test:

- Conversion of raw voltage data to engineering units (stress, strain)
- Correction of the strain data for transverse sensitivity of the strain gages
- "Averaging" of the strain data to eliminate thru-the-thickness strain variation (bending)
- Preliminary calculation of material properties.

Conversion of the strain data from raw voltages to engineering units used conventional Wheatstone bridge calculations [28]. Correction of the strain data for transverse sensitivity was carried out in the usual fashion for the rosette gages [28-29]. Correction for transverse sensitivity of the single gage was carried out as outlined by Dally and Riley (Section 10.4 [28]) and using the assumption that the ratio of the transverse/longitudinal strain was the same on both sides of the test coupon.

"Averaging" of the strain data to eliminate bending effects was done by simple averaging for the tests in which factory rosettes were used. For tests in which the rosette was composed of stacked single gages, the averaging took into account the differences in the distances of the individual grids from the neutral axis (Appendix C).

Following completion of all the tests at one condition (e.g. one of the twelve combinations of fiber orientation, temperature, and radiation dose) the final calculation of material properties (E and ν) was made. These properties were calculated by fitting quadratic curves through the data in a least-squares sense (curvilinear regression). Plots showing the data points used in the regression analysis are presented in Appendix A.

The following example illustrates the analysis method and the details are presented in Appendix C. Assume it is desired to calculate Young's modulus, E, given a set of stress-strain data. Young's modulus is defined to be the initial slope of the stress-strain curve. If a function of the form $f(\varepsilon) = \sigma = A + B\varepsilon + C\varepsilon^2$ is chosen to represent the stress-strain response, application of the least squares criterion yields the following set of equations:

$$\begin{bmatrix} n & \Sigma\varepsilon & \Sigma\varepsilon^2 \\ \Sigma\varepsilon & \Sigma\varepsilon^2 & \Sigma\varepsilon^3 \\ \Sigma\varepsilon^2 & \Sigma\varepsilon^3 & \Sigma\varepsilon^4 \end{bmatrix} \begin{bmatrix} A \\ B \\ C \end{bmatrix} = \begin{bmatrix} \Sigma\sigma \\ \Sigma\varepsilon\sigma \\ \Sigma\varepsilon^2\sigma \end{bmatrix}$$

The summations are made over the entire range of the mechanical test data and include data points taken from all tests at the same condition. The total number of data points included in the summations is denoted "n". The slope of the stress-strain curve, E, is obtained by simply differentiating: $E = d\sigma/d\varepsilon = B + 2C\varepsilon$. Thus an expression for E, instantaneous tangent modulus, is obtained as a function of the longitudinal strain, ε. The initial (elastic) modulus, which is generally the quantity of most interest, is obtained by setting $\varepsilon = 0$. Similar calculations yield Poisson's ratio or properties obtained from an equation of the form $x = f(y) = A + By + Cy^2$ (Appendix C).

Quadratic curves were used because they were the lowest order polynomial which appeared to be able to match the behavior of the data. It was recognized that quadratics often tend to "hook" near the ends of the data (e.g. the origin and locus of failure). The slope of the function is, obviously, more susceptible to this behavior than the value of the function (in the example above, E is more susceptible than σ). To counteract this phenomena, one-third of the data points from each test were "reflected" through the origin into the third quadrant in order to force the slope to be accurately represented near the origin.

This is a somewhat novel method of analysis and requires some justification. Primary motivation was provided by the nature of the stress-strain data---if often appeared to be quite nonlinear over the course of the entire test. Additionally, although only initial "elastic" properties are commonly reported, it is often desirable to be able to conveniently estimate properties at any point on the stress-strain curve. Finally, it was intended to reduce the amount of judgement exercised by the analyst when determining properties. When properties are estimated using linear regression over a limited subset of the available data or "with a straightedge and pencil", the value produced can be influenced considerably by the biases of the analyst. It was believed that this method would remove much of this subjectivity, allow for better reproducibility, and simplify the data reduction task.

It can be argued that the present method merely substitutes a different sort of bias, in that a specific functional form is chosen a priori. However, the specific values of the coefficients in the assumed functional form are determined by criteria which are applied to different data sets in a uniform and consistent manner. In any case, the differences between an approach such as that outlined in this section and the other methods referred to above are generally small ($< 5\%$).

The strength properties were determined by dividing the maximum load by the appropriate cross-sectional area. The values for the five tests at each condition were then averaged.

It was, unfortunately, not possible to obtain the failure strains in a similar fashion. The strain gage data near failure were often unreliable. It was not uncommon for at least one of the strain gages to be broken at this point in the test. In addition, the maximum load was obtained using a peak reading meter while the final strain values were not. The failure strains were calculated from the quadratic σ-ε curves, described above, by solving the appropriate equation for the strain corresponding to the strength (failure stress). When comparisons can be made, the calculated values and the measured final strain value are in good agreement.

4.0 Compression Test Results

This section will discuss the results of the compression tests. The compression test matrix is shown in Table 3. First, the effects of temperature and irradiation on the overall stress-strain response will be discussed. The degree of non-linearity in the response will be emphasized. Following this, the specific engineering properties (Young's moduli, Poisson's ratios, strengths, and failure strains) will be discussed in detail.

For convenient reference, these properties are summarized and tabulated in Table 4. The stress-strain curves for all the test conditions are included in Figure 14 to Figure 18. These curves are the quadratic regression curves calculated as described in the preceding section.

The detailed test results and regression analysis used to calculate the properties can be found in Appendix A. The interval estimates ("error bars") in Figure 20 to Figure 27 are ± 2 standard errors on the mean values. The methods used to calculate the standard errors are outlined in Appendix C.

Table 3. Test Matrix for T300/934 Compression Coupons

Radiation Dose	Temp. °F (°C)	Number of Tests	
		Longitudinal	Transverse
Baseline (non-irradiated)	-250 (-157)	5	5
	Room	5	5
	250 (121)	5	5
Irradiated (10,000 Mrads)	-250 (-157)	5	5
	Room	5	5
	250 (121)	5	5

Test: Monotonic Compression
Material: T300/934 Gr/Ep
Nominal Thickness: 8 plies

Table 4. T300/934 Compressive Properties

		Baseline		Irradiated		
Temp	Prop	Value	Δ_{RT}%	Value	Δ_{RT}%	Δ_{IR}%
-250°F (-157°C)	X_c (ksi)	241	+25	228	+21	-5
	Y_c (ksi)	56.5	+86	51.8	+97	-8
	E_1 (msi)	17.2	+11	16.0	+10	-7
	E_2 (msi)	2.10	+29	2.14	+23	+2
	ν_{12}	0.136	-25	0.104	-32	-24
	ν_{21}	0.0320	-13	0.0324	-28	+1
	ε_1^f (%)	1.62	+12	1.68	-16	+4
	ε_2^f (%)	3.26	+6	2.92	+10	-10
Room	X_c (ksi)	193	---	188	---	-3
	Y_c (ksi)	30.4	---	26.3	---	-13
	E_1 (msi)	15.5	---	14.6	---	-6
	E_2 (msi)	1.63	---	1.74	---	+7
	ν_{12}	0.182	---	0.153	---	-16
	ν_{21}	0.0366	---	0.0447	---	+22
	ε_1^f (%)	1.45	---	2.00	---	+38
	ε_2^f (%)	3.07	---	2.65	---	-14
250°F (121°C)	X_c (ksi)	126	-35	48.3	-74	-62
	Y_c (ksi)	18.9	-37	8.71	-67	-54
	E_1 (msi)	15.0	-3	14.4	-1	-4
	E_2 (msi)	1.80	+10	0.666	-62	-63
	ν_{12}	0.309	+70	0.384	+151	+24
	ν_{21}	0.0791	+116	0.239	+435	+237
	ε_1^f (%)	0.751	-48	0.310	-85	-59
	ε_2^f (%)	1.94	-39	1.75	-34	-10

Δ_{RT}% = percent change w.r.t room temperature value

Δ_{IR}% = percent change of irradiated w.r.t baseline value

4.1 Overall Stress-Strain Response

4.1.1 Longitudinal Response

The longitudinal stress-strain ($\sigma_1 - \varepsilon_1$) responses at different temperatures are shown in Figure 14a for the baseline material and Figure 14b for the irradiated material. It is readily apparent that the ultimate properties, strength and failure strain, are significantly affected by temperature in both materials. It is important to note the nonlinearity of the σ-ε response. At cryogenic and room temperature, the curves show a slight "softening" at high loads. This is expected under compressive load. The apparent stiffening at elevated temperature, which occurs in both materials, was unexpected. Careful examination of the curves reveals that the initial modulus appears unchanged but the material stiffens as the load increases. Stiffening has been previously observed in tensile tests of unidirectional T300/934 [3,7]. The stiffening in tension was attributed to the straightening of initial fiber waviness or to increased alignment of the fiber's internal structure. Neither of these mechanisms seems very plausible for compressive loading.

The stiffening observed in compression may be due to increased fiber-fiber interaction. The matrix is softened, at elevated temperature, to such an extent that it can no longer restrain the lateral deflections of the fibers as efficiently as it does at lower temperatures. As the load is increased, the fibers develop additional curvature and eventually interact with each other leading to an increase in stiffness. This process is illustrated schematically in Figure 15.

The mechanism advanced above is highly conjectural and considerably more experimental and theoretical work would be needed to prove or disprove it. It can be argued that the relatively large fiber deflections required are unrealistic and that they imply considerable softening of the $\sigma - \varepsilon$ response before the hypothesized interaction, and subsequent stiffening, take

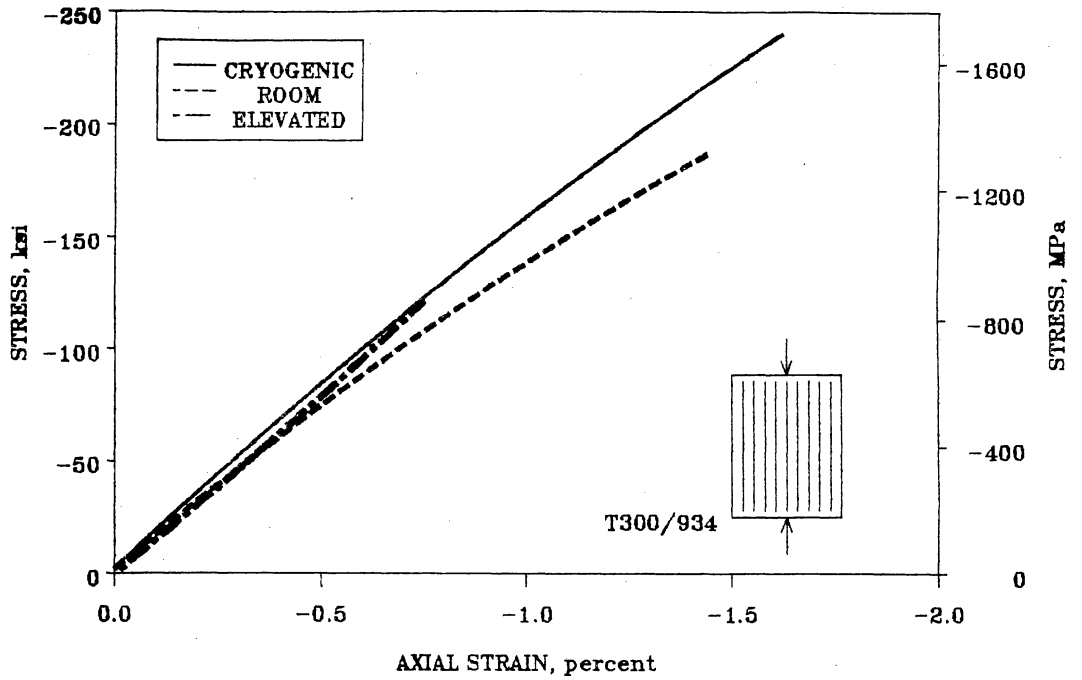

a) Baseline

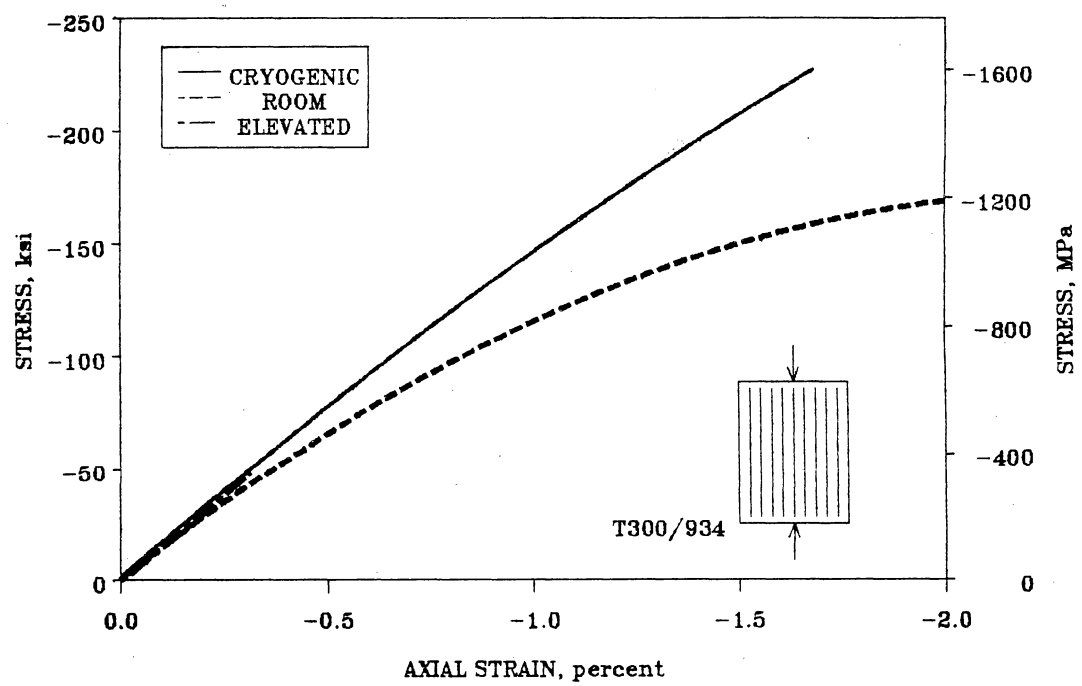

b) Irradiated

Figure 14. Effect of Temperature on T300/934 Longitudinal Compressive Stress-Strain Response

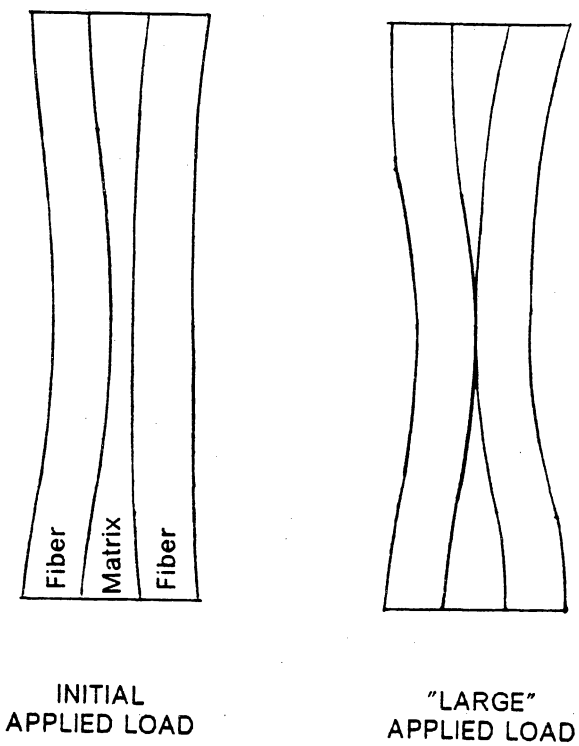

Figure 15. Schematic Representation of Fiber/Fiber Interaction

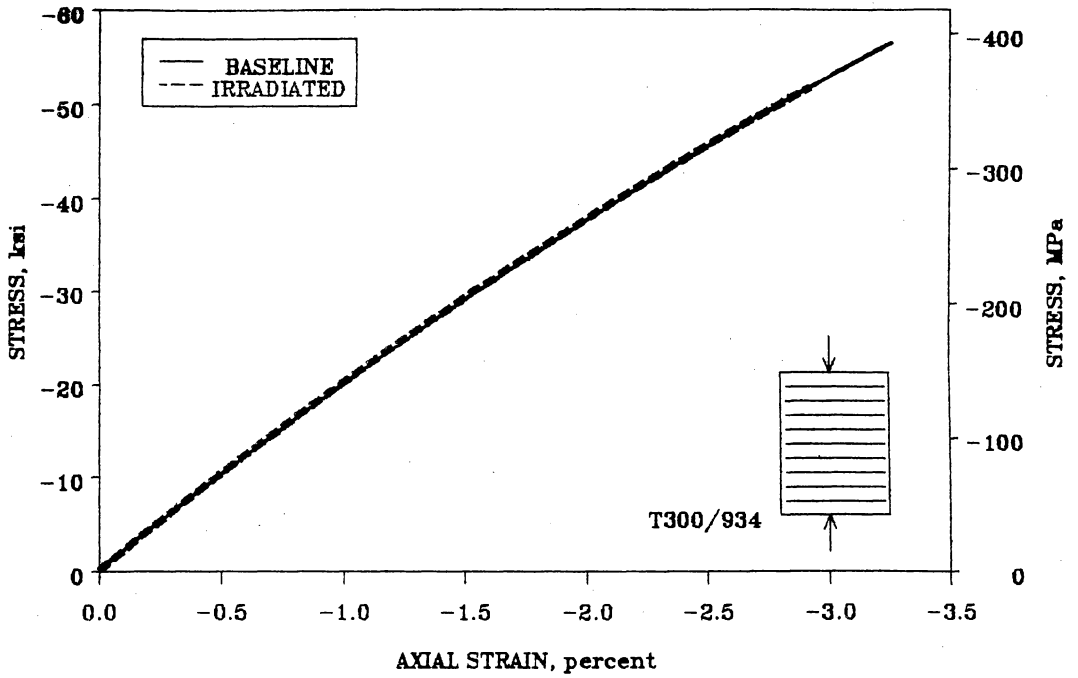

a) 90° Response

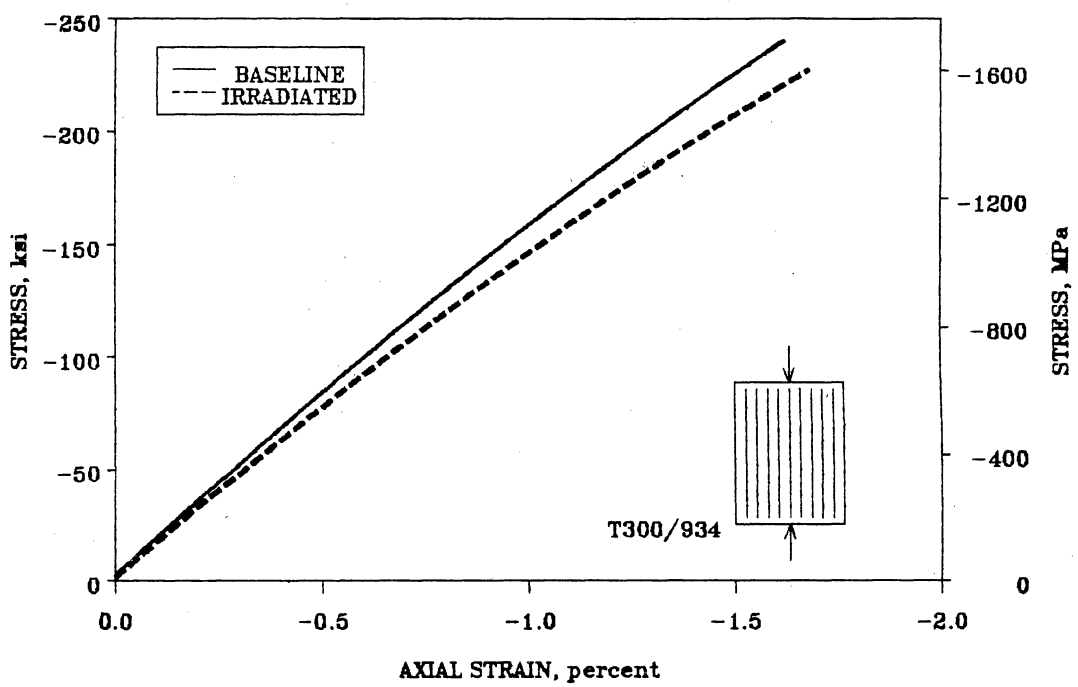

b) 0° Response

Figure 16. Effect of Irradiation on T300/934 Compressive Stress-Strain Response at Cryogenic Temperature

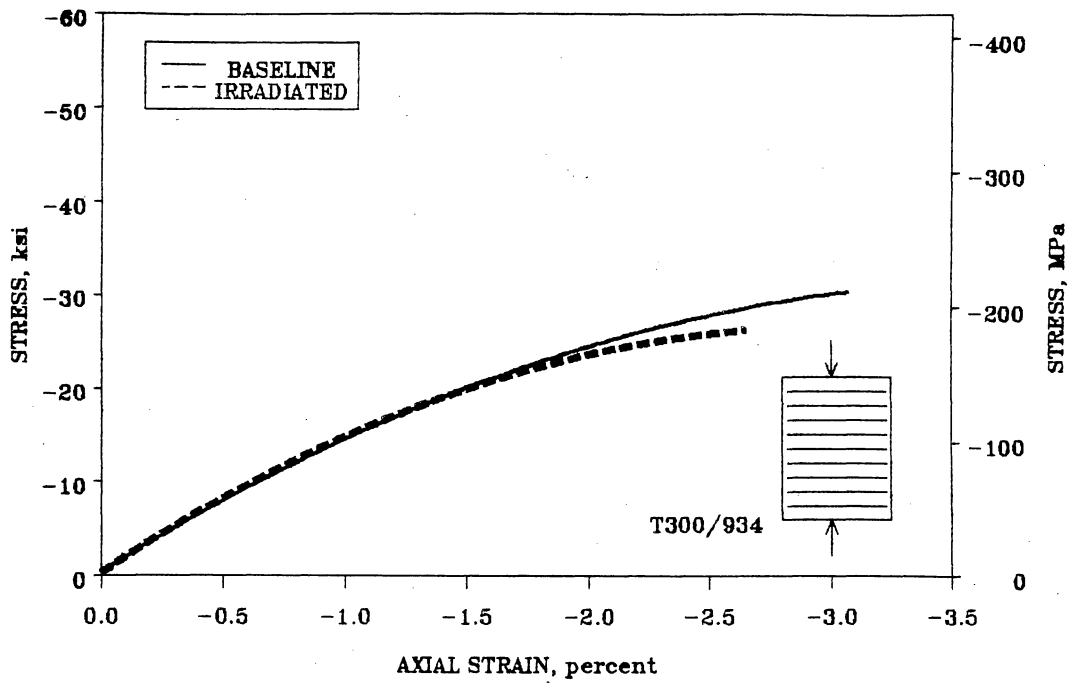

a) 90° Response

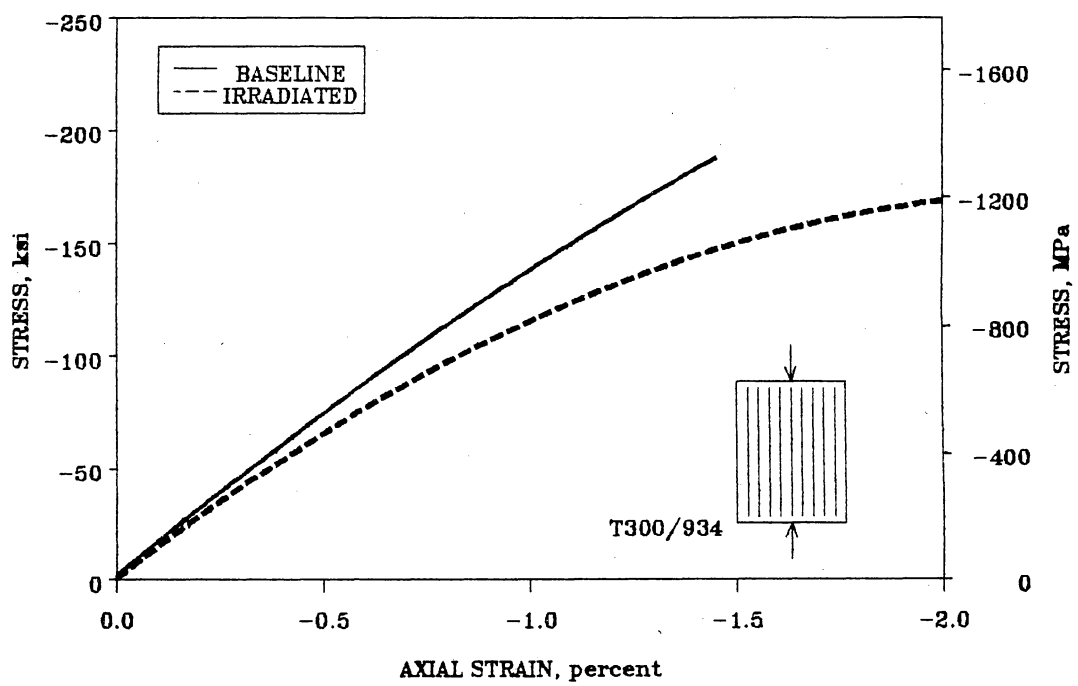

b) 0° Response

Figure 17. Effect of Irradiation on T300/934 Compressive Stress-Strain Response at Room Temperature

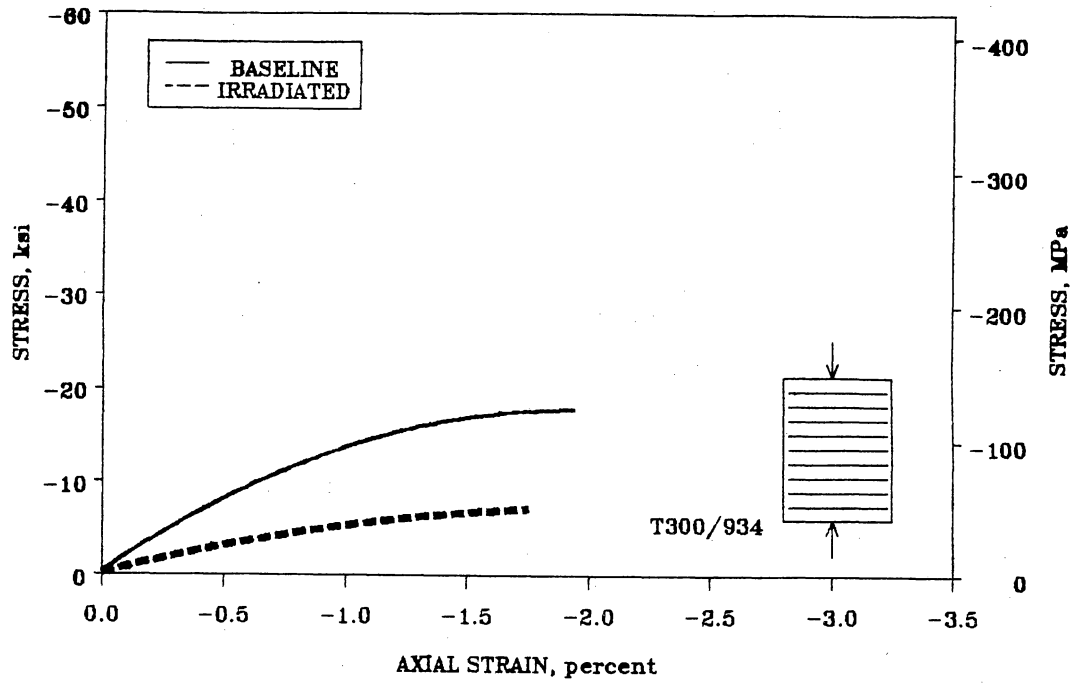

a) 90° Response

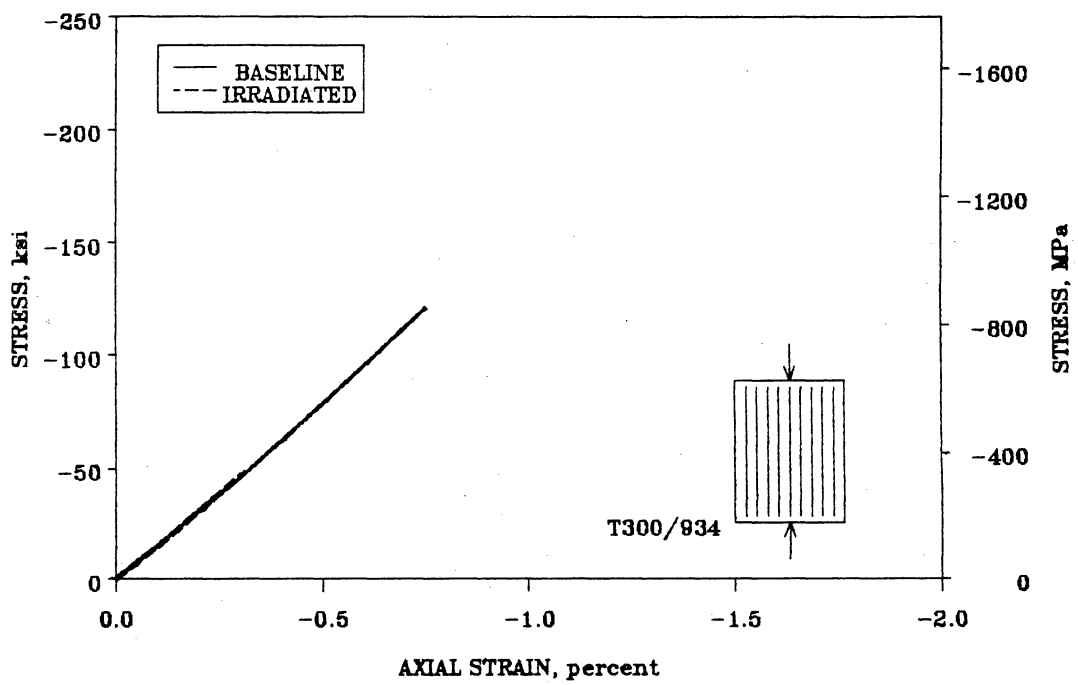

b) 0° Response

Figure 18. Effect of Irradiation on T300/934 Compressive Stress-Strain Response at Elevated Temperature

place. Nonetheless, the above mechanism is consistent with certain other phenomena observed during the mechanical testing.

The relatively large curvatures of the fibers required in the above process would undoubtedly lead to high local stresses in the matrix. These local matrix stresses may be high enough to fracture the matrix and lead to material failure. This will be discussed in more detail in the section on failure mechanisms. The large lateral deflections also imply increases in Poisson's ratio. As will be discussed later in this Chapter, large increases in ν_{12} were measured at the elevated test temperature for both the baseline and irradiated materials.

The stiffening is not believed to be related to the test method because it wasn't observed in either of the other test temperatures and wasn't observed in any of the 90° tests. Because the 90° coupons fail at lower stresses and are more compliant than the 0° coupons, it is believed they would be more susceptible to problems with binding in the test fixture.

At room and cryogenic temperatures the matrix stiffness is sufficient to laterally restrain the fibers such that composite strength more nearly reflects the strength of the fibers. These results agree well with the observation by Hahn and Williams [24] that a strong correlation exists between composite longitudinal compressive strength and matrix stiffness. The results also indicate the need to study the influence of matrix degradation on the compressive properties of the composite.

The baseline and irradiated $\sigma_1 - \varepsilon_1$ curves are compared at each test temperature in Figure 16b-Figure 18b. At cryogenic and room temperatures the curves diverge under increasing load, showing that irradiation "softens" the response of the material. At elevated temperature (Figure 18b) the curves don't diverge, however, the irradiated material fails at stresses considerably less than (approximately one-half) the baseline material.

4.1.2 Transverse Response

The transverse stress-strain ($\sigma_2 - \varepsilon_2$) responses at different temperatures are compared in Figure 19 for both the baseline and irradiated material. Comparison of Figure 14 and Figure 19 indicates that, as expected, the transverse response is more temperature dependent than the longitudinal response. The behavior is also quite nonlinear with the room and elevated temperature curves becoming nearly horizontal at failure.

The baseline and irradiated $\sigma_2 - \varepsilon_2$ curves are quite similar at cryogenic and room temperature (Figure 16a and Figure 17a, respectively) , but sharply different at elevated temperature. (Figure 18a). The difference at elevated temperature is a direct consequence of the reduced T_g following irradiation. As discussed in the preceding chapter, the TMA (thermomechanical analysis) results clearly show the material to be in the softening range in the irradiated, elevated temperature condition and the decrease in modulus is expected.

4.2 Young's Modulus

4.2.1 Longitudinal Modulus

Young's modulus in the fiber direction, E_1, is only slightly affected by temperature (Figure 20, Table 4). For the baseline material, E_1 is 10% higher at cryogenic temperature and 3% lower at elevated temperature, than the room temperature value of 15.5 msi (107 GPa). The irradiated material exhibits similar trends with a 10% higher value at cryogenic temperature and a slightly, 1%, lower value at elevated temperature. The longitudinal modulus of the

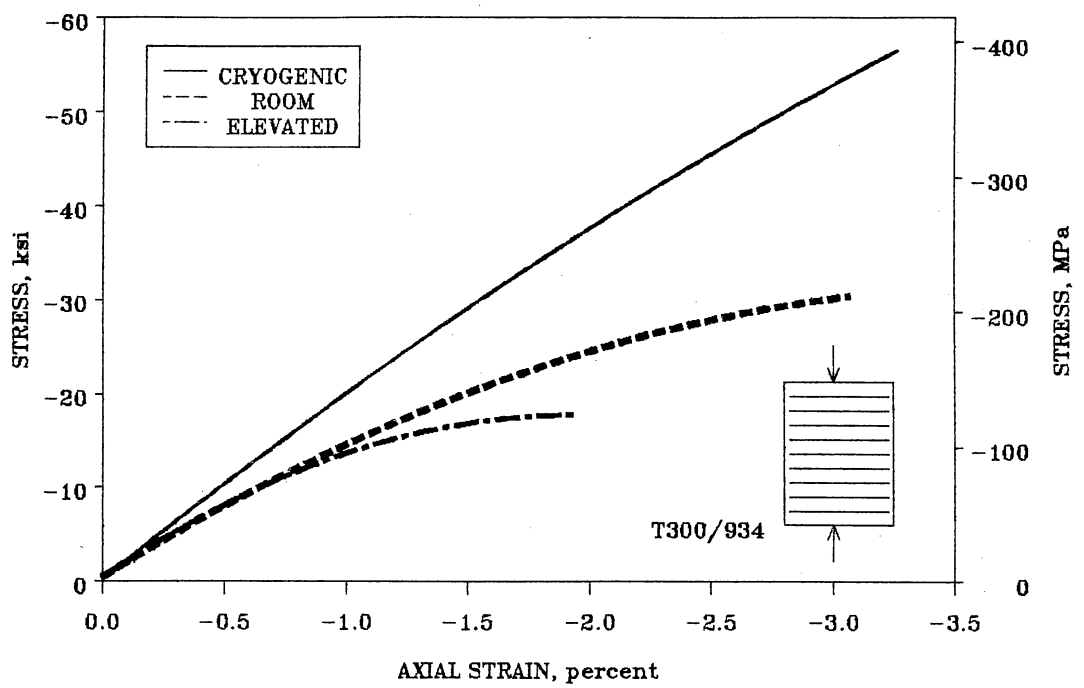

a) Baseline

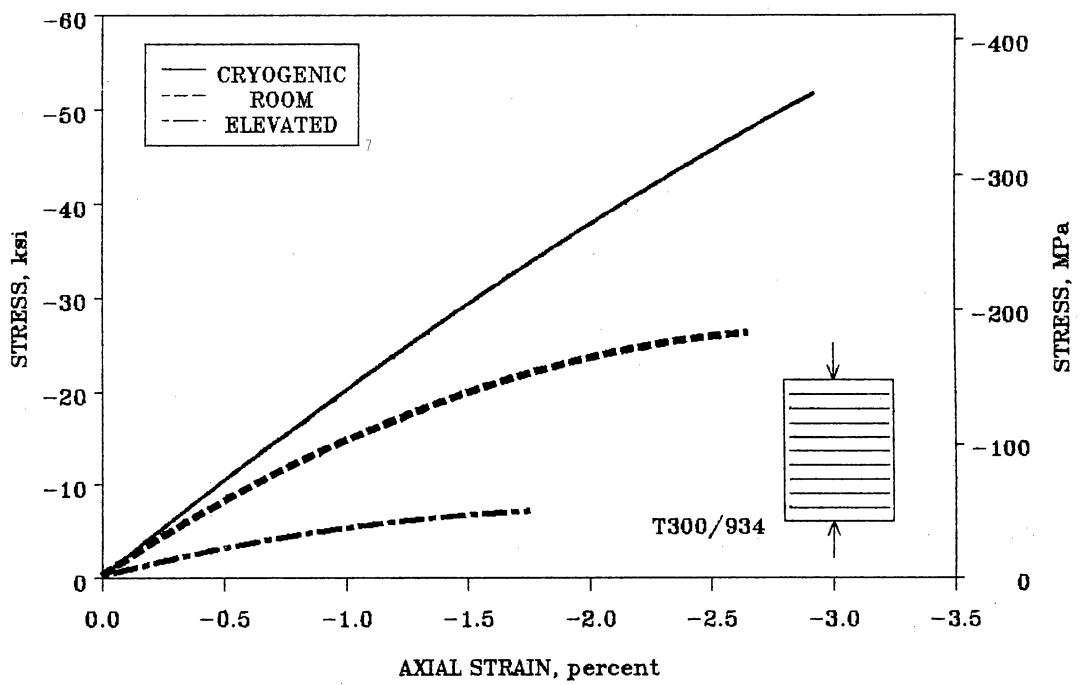

b) Irradiated

Figure 19. Effect of Temperature on T300/934 Transverse Compressive Stress-Strain Response

irradiated material is less than that of the baseline material across the entire temperature range. The difference is -7% at cryogenic, -6% at room, and -4% at elevated temperature.

The behavior of E_1 is consistent with the fact that it is a fiber dominated property and that the fibers are essentially inert to temperatures in this range. The reduction in E_1 following irradiation is somewhat difficult to explain, especially since carbon fibers are believed to be inert to irradiation [3,7]. These changes are probably related to the changes in the matrix and fiber/matrix interfacial properties. In addition, as noted in Chapter 2, the irradiated material seemed to have a somewhat lower fiber volume fraction, v_f, than the baseline. While this could account for the radiation-induced decrease in E_1, the magnitude and cause of the decrease in v_f remain unclear.

4.2.2 Transverse Modulus

The transverse Young's modulus, E_2, is more temperature dependent than E_1 (Figure 21, Table 4). For the baseline material, E_2, is 29% higher at cryogenic temperature and 10% higher at elevated temperature (both with respect to the room temperature value of 1.63 msi; 11.2 GPa). For the irradiated material, E_2 is 23% higher at cryogenic temperature, and 62% lower at elevated temperature. The transverse modulus for the irradiated material is slightly greater than for the baseline material at cryogenic and room temperature (2% and 7%, respectively). At elevated temperature, the irradiated material has a 63% lower modulus than the baseline material.

Transverse modulus is, of course, highly matrix dependent and generally follows the expected trends. In particular, the large decrease in E_2 for the irradiated, elevated temperature condition can be directly related to the radiation-induced decrease in the glass transition temperature (see Chapter 2 for a discussion of the T_g). The radiation-induced increases in E_2 at

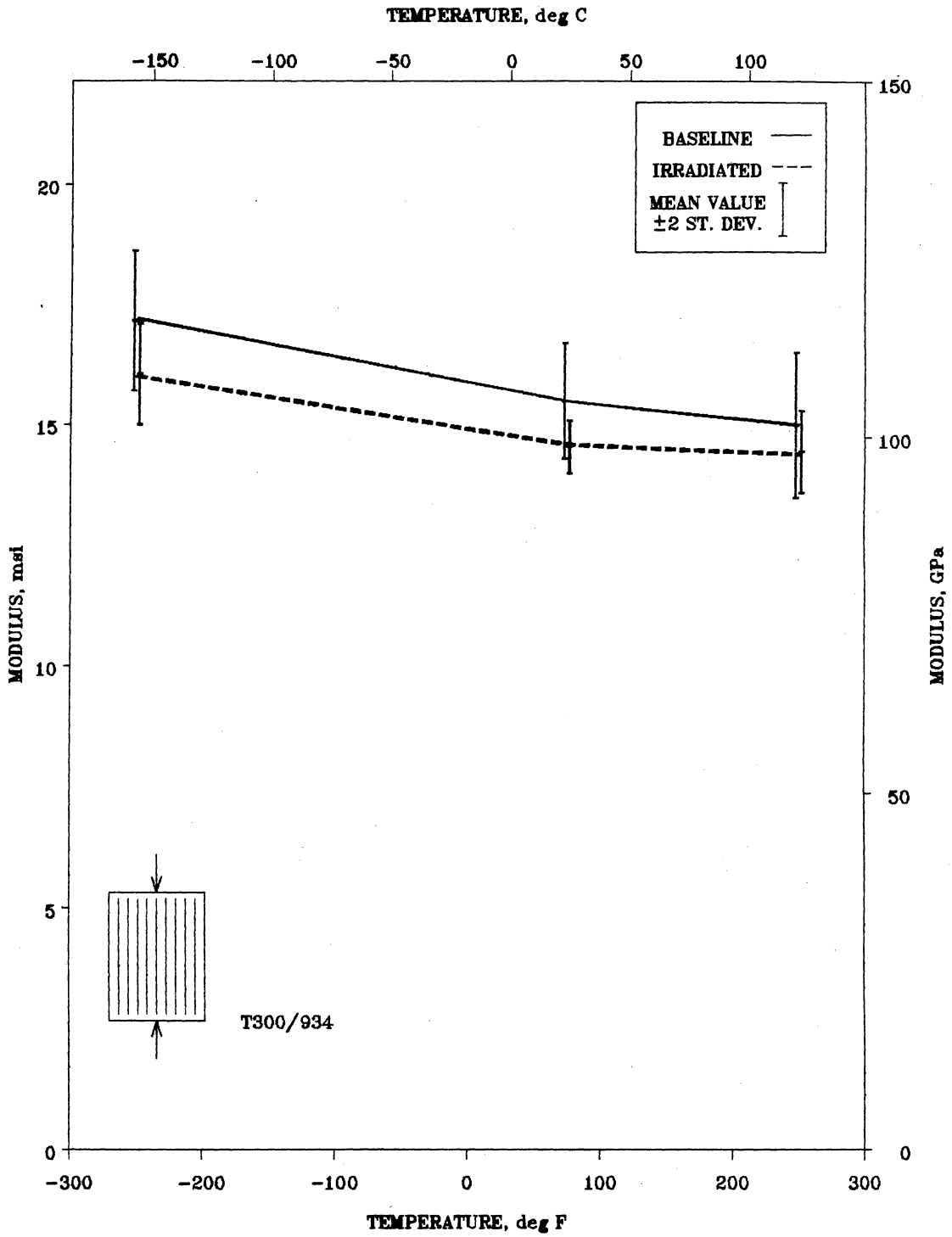

Figure 20. Compressive Longitudinal Modulus of T300/934 vs Temperature

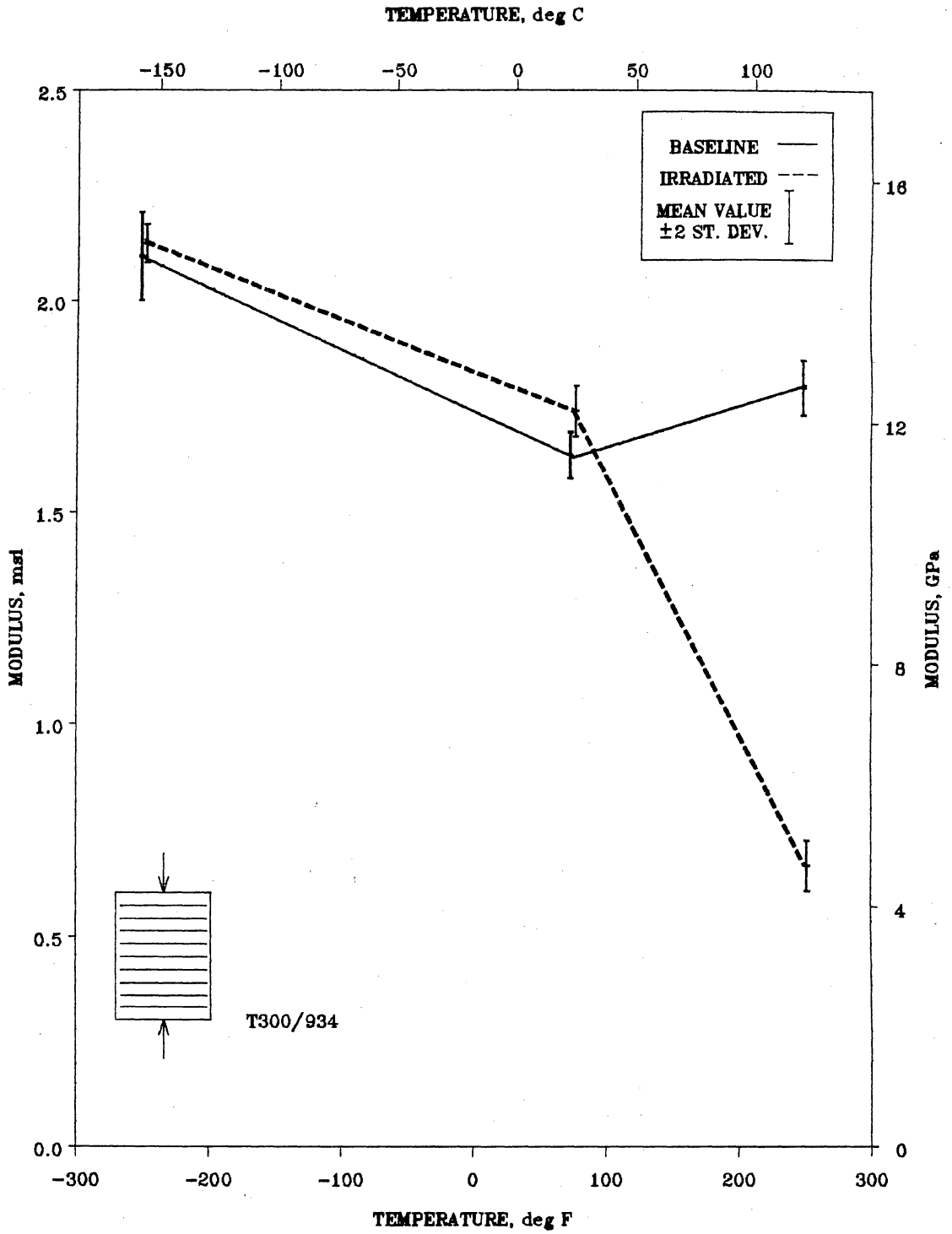

Figure 21. Compressive Transverse Modulus of T300/934 vs Temperature

cryogenic and room temperature are believed to be due to an increase in the modulus of the matrix at these temperatures (it will be shown in Chapter 5 that the modulus of the neat resin increases, following irradiation, at room temperature). The increase in E_2 for the baseline material at elevated temperature may be a result of changes in the residual (curing) stresses. The complexity of the residual stress state, the influence of the transverse fiber properties and role of the fiber-matrix interface make the situation somewhat unclear.

4.3 Poisson's Ratios

4.3.1 Major Poisson's Ratio (0° test)

Poisson's ratio is defined to be $-\frac{\varepsilon_y}{\varepsilon_x}$, when the stress state is uniaxial (in the x-direction) and ε_y is the strain perpendicular to the load. In the test of a 0° coupon, this ratio is called the major Poisson's ratio and is denoted ν_{12}. Plots of the Poisson response (ε_y vs ε_x) for all of the test conditions are presented in Appendix A. The major Poisson's ratio was significantly effected by temperature for both the baseline and irradiated materials (Figure 22, Table 4). For the baseline material, ν_{12} is 25% lower at cryogenic temperature and 70% higher at elevated temperature, with respect to the room temperature value of 0.182. The irradiated material is even more influenced by temperature with the cryogenic value being 32% less than and the elevated temperature value 152% greater than the room temperature value (0.153). The values of ν_{12} for the irradiated material are lower than for the baseline material at cryogenic and room temperature, by 24% and 16%, respectively, but 25% greater at elevated temperature.

The increases at elevated temperature are consistent with the argument advanced earlier to explain the stiffening in 0° coupons, namely that the fibers tend to absorb the load by bending

and the matrix fails to provide adequate support to prevent large (fiber) lateral deflections. This, obviously, leads to larger transverse deformations and increased Poisson's ratios. The radiation-induced change at elevated temperature, 25% increase in ν_{12}, is also consistent with this argument. The radiation-induced decreases in ν_{12} at room and cryogenic temperature may be due to reductions in the residual (curing) stresses [3,7] and may also be related to the increase in resin modulus (Chapter 5).

The Poisson response has several additional interesting and perplexing aspects. First, the magnitude of the measured values (i.e. room temperature values of 0.153-0.182) are substantially less than those reported in the literature for Gr/Ep (0.24-0.40), [20, 22-23]. This, almost certainly, is due to the effect of the tabs (and grips) in restraining transverse deformation in these low aspect ratio compression specimens. If ν_{12} is calculated from the measured values of ν_{21}, E_1, and E_2 using the reciprocal relationship ($E_1\nu_{21} = E_2\nu_{12}$) the results shown in Table 5 are obtained. The calculated cryogenic and room temperature values seem reasonable. The irradiated, elevated temperature (calculated) value is adversely affected by several factors, the most significant of which is the large increase in ν_{21} in this condition (to be discussed below).

In a recent report by Pindera, Gurdal, Hidde, and Herakovich [30] the effect of end constraints in determining Poisson's ratio under compressive loading is discussed. They investigated the problem using the finite element method and found that the apparent ν_{12} values, from a similar type of compression test, were predicted to be about about 60% of the actual value. Their experimental results were in excellent agreement with the numerical predictions. The material properties used in [30] are for aramid/epoxy and the specimen geometry is somewhat different so the results aren't directly applicable to this case. However, it is likely that the magnitude of the effect is the same (especially when it is noted that the calculated values of ν_{12} in Table 5 are roughly twice the measured, or apparent, values).

Table 5. Calculated Values of Major Poisson's Ratio

Dose	Temp °F (°C)	ν_{21} measured	ν_{12} measured	ν_{12} calculated
Baseline	-250 (-157)	0.0320	0.136	0.262
	Room	0.0366	0.182	0.350
	250 (121)	0.0791	0.309	0.658
Irradiated (10,000 Mrad)	-250 (-157)	0.0324	0.104	0.239
	Room	0.0447	0.153	0.378
	250 (121)	0.239	0.384	5.17

$$\nu_{12,\,calculated} = \nu_{21,\,measured}\left(\frac{E_{1,\,measured}}{E_{2,\,measured}}\right)$$

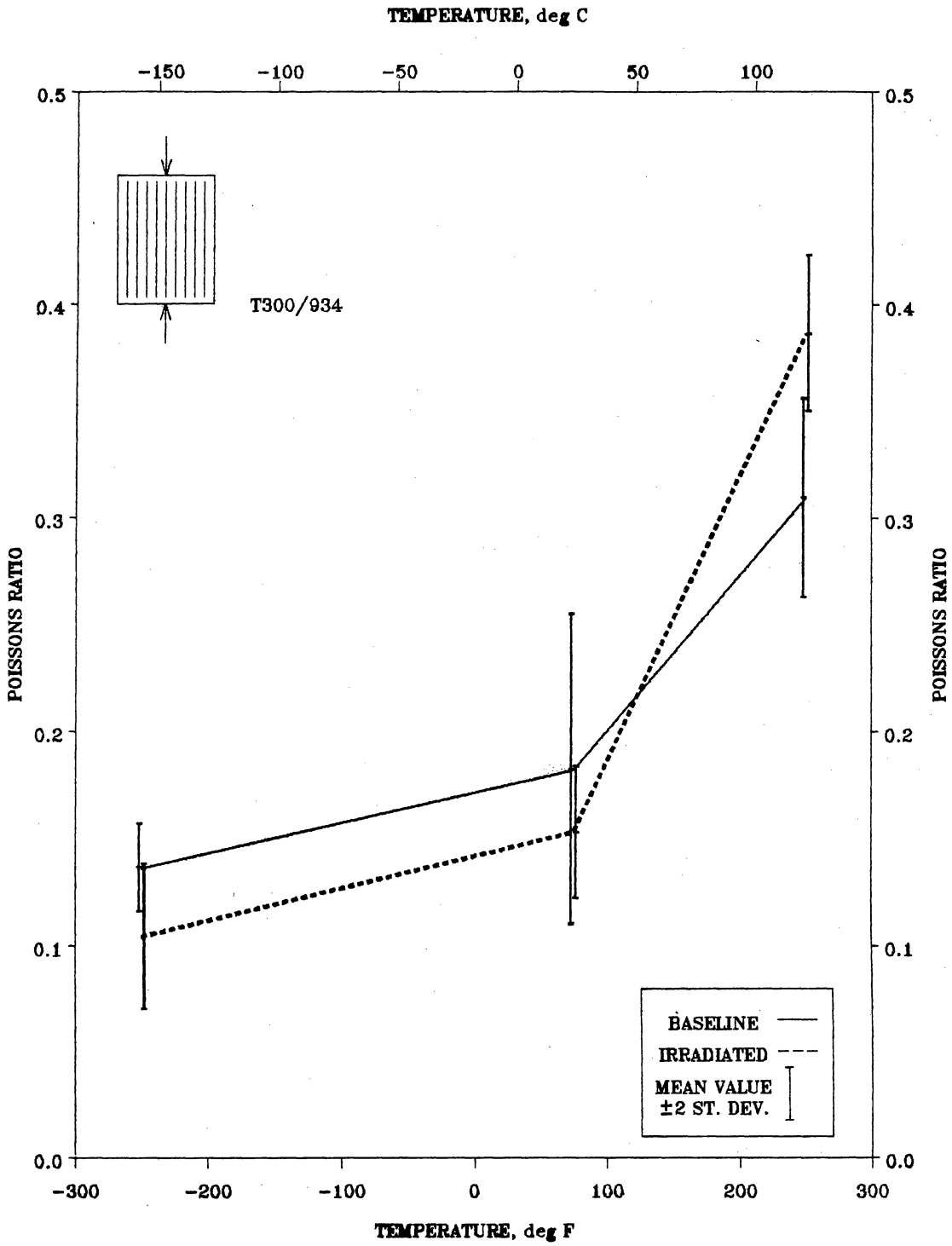

Figure 22. Compressive Major Poisson's Ratio of T300/934 vs Temperature

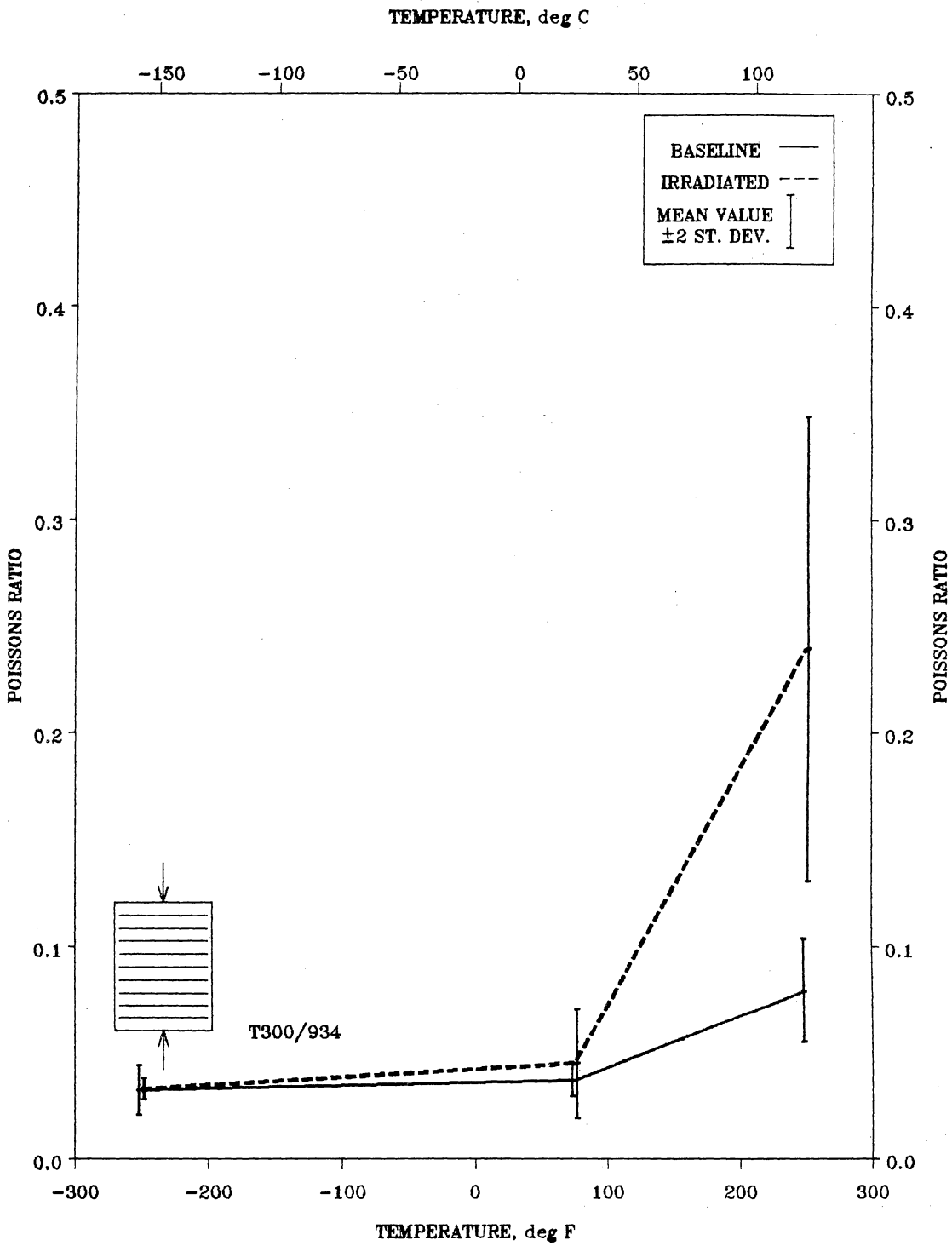

Figure 23. Compressive Minor Poisson's Ratio of T300/934 vs Temperature

The most disturbing aspect of the Poisson's ratio data is the large variability associated with it. This variability is most evident in the irradiated material at elevated temperature (Appendix A). Because similar large variations are not present in the stress-strain and strength data, it is believed that the variability is associated primarily with the transverse strain measurement. The strains were measured over a small portion of the coupon surface. Obviously, if the strain state is non-uniform the measured data could reflect local rather than global response.

4.3.2 Minor Poisson's Ratio (90° test)

The Poisson's ratio obtained from the test of a 90° coupon is referred to as the minor Poisson's ratio and denoted ν_{21}. For the baseline material, ν_{21} is 13% lower than the room temperature value at cryogenic temperature and more than double it (+116%) at elevated temperature (Figure 23, Table 4). These trends are are even more extreme for the irradiated material. The cryogenic value, for the irradiated material, is 28% lower than the room temperature value, while the elevated temperature value is over 5 times (+435%) larger. The irradiated material has a higher ν_{21} than the baseline material at all three temperatures. The difference increases with increasing temperature and is 1%, 22%, and 237% at cryogenic, room, and elevated temperature, respectively.

Quite obviously, the really intriguing result is the elevated temperature behavior of the irradiated material. It seems apparent that the measured response is indicative of a general lack of cohesion between the fibers and the matrix. The resistance to transverse deformation one would expect the fibers in a 90° coupon to provide is simply not present in this condition. Whether this lack of cohesion is due to a general degradation of the matrix or strictly to fiber/matrix interfacial effects is indeterminate from this data alone. It should be noted that the Poisson ($\varepsilon_y - \varepsilon_x$) data have a large amount of scatter, particularly at elevated temperature.

4.4 Compressive Strength

4.4.1 Longitudinal Compressive Strength

The compressive strength in the fiber direction, X_c, is quite temperature dependent (Figure 24, Table 4). For the baseline material, X_c is 25% higher at cryogenic temperature and 35% lower at elevated temperature. The irradiated material exhibits similar trends with a 21% greater value at cryogenic temperature and a 74% lower value at elevated temperature. The effect of irradiation is small at cryogenic and room temperature, (irradiated values 3-5% less than the corresponding baseline values) but more substantial at elevated temperature where X_c is 62% lower in the irradiated material. The scatter in the data is modest for longitudinal Gr/Ep compressive strength data.

The changes in X_c can be related to changes in the matrix strength and stiffness. At cryogenic temperature, the matrix is stiffer and stronger (in compression) leading to more efficient support of the fibers and therefore higher strengths. At elevated temperature the matrix is softer and weaker leading to less efficient support of the fibers and, hence, lower strengths. This is particularly evident in the elevated temperature, irradiated condition where the matrix is more severely degraded and the longitudinal strength is significantly reduced. These points will be discussed in more detail in the section on failure mechanisms.

4.4.2 Transverse Compressive Strength

The compressive strength in the direction perpendicular to the fibers, Y_c , is nearly a linear function of temperature (Figure 25, Table 4). The transverse compressive strength for the

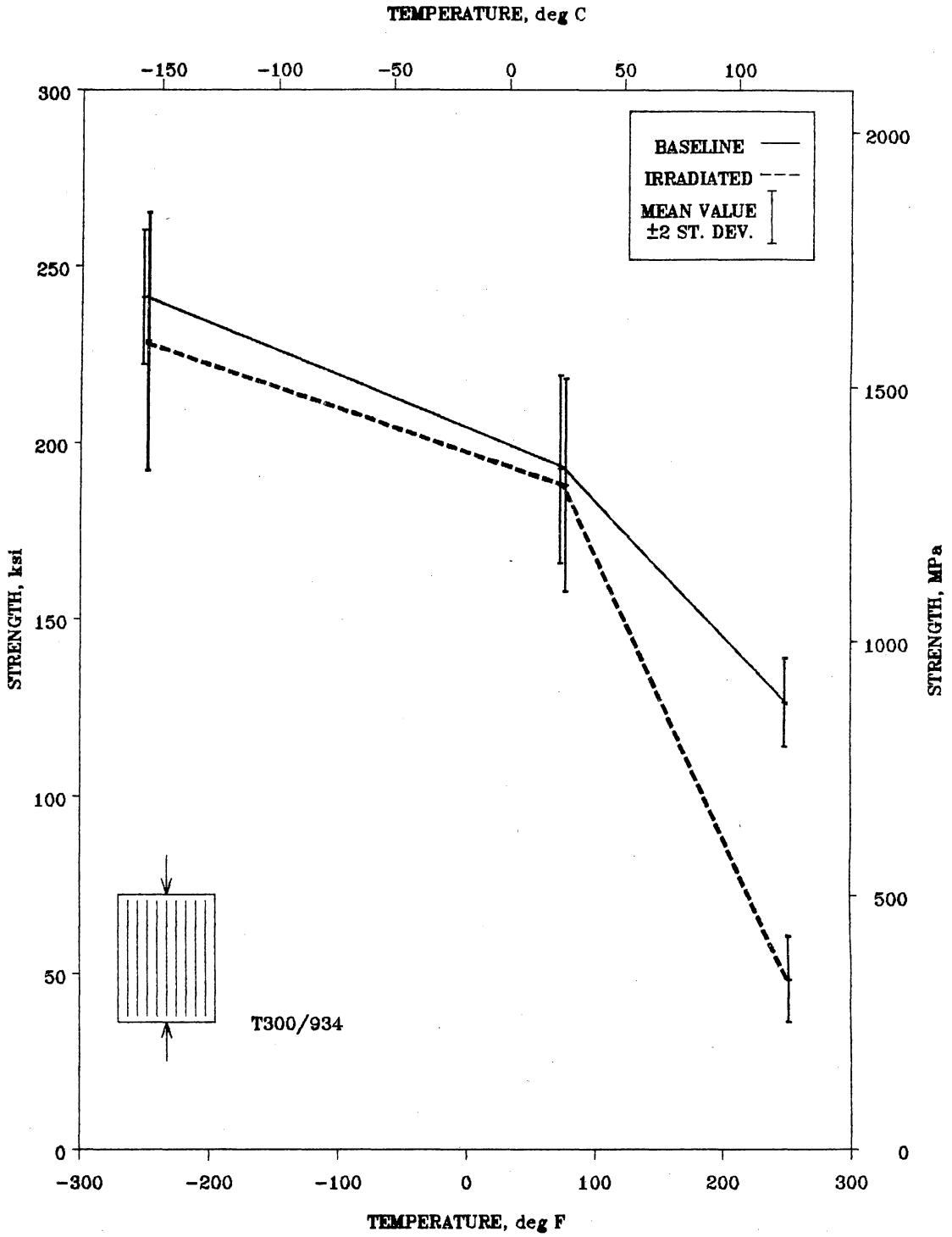

Figure 24. Longitudinal Compressive Strength of T300/934 vs Temperature

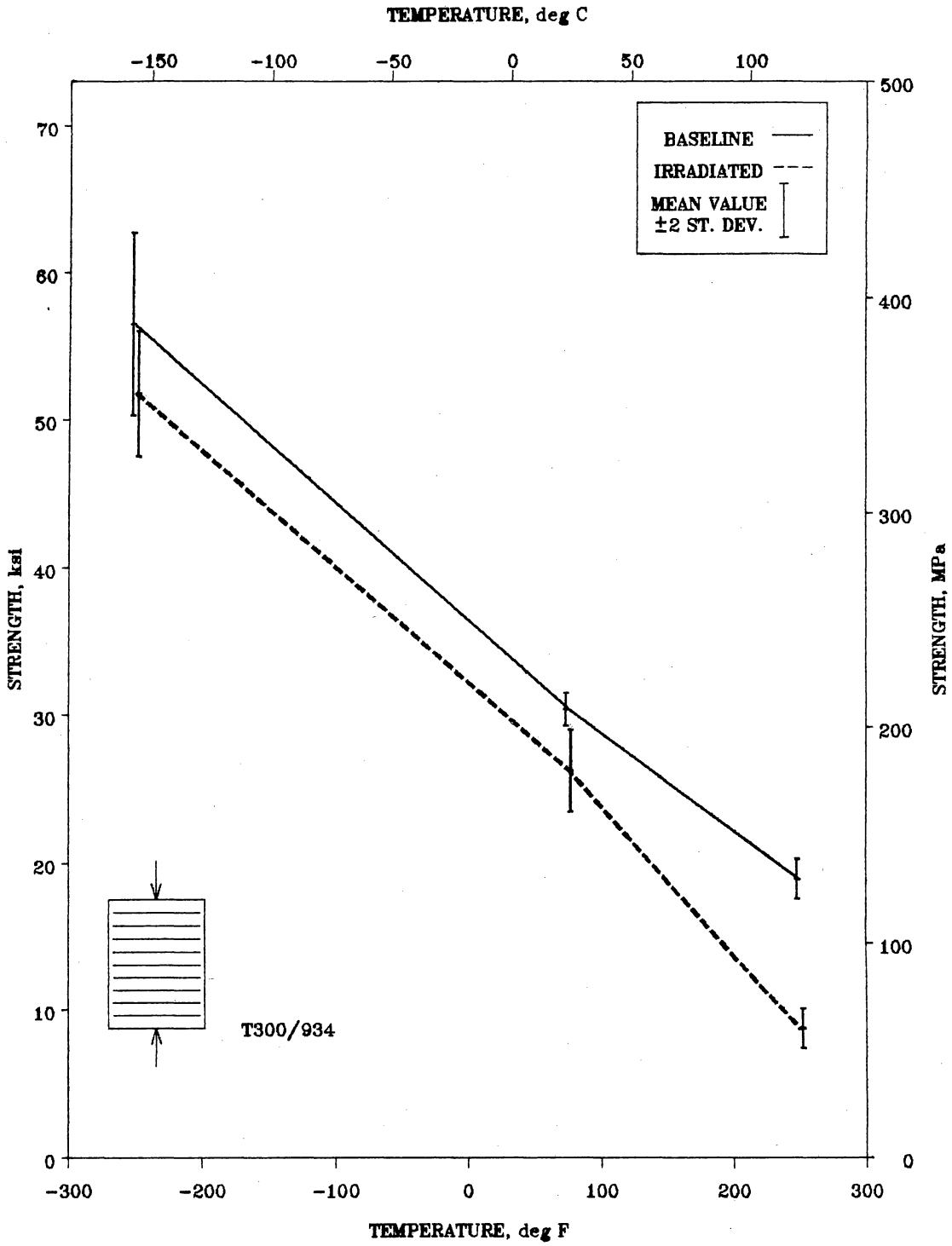

Figure 25. Transverse Compressive Strength of T300/934 vs Temperature

baseline material is 85% higher at cryogenic temperature and 37% lower at elevated temperature. For the irradiated material, Y_c is 95% greater at cryogenic temperature and 67% lower at elevated temperature than the room temperature value. The transverse compressive strength for the irradiated material is lower at all three temperatures. The difference is modest, -8 and -13%, at cryogenic and room temperature, respectively, when compared to the -54% difference at elevated temperature.

The strong temperature dependence of Y_c is consistent with the known effect of temperature on polymeric materials. Lee and Neville [2] state that cryogenic temperature increases the brittleness of epoxies and may provide up to 100% improvement in tensile properties (strength and modulus). It is reasonable to assume the compressive properties experience similar improvement at cryogenic temperature. The fact that irradiation reduces Y_c across the entire temperature range is indicative of a general degradation of the epoxy network structure.

4.5 Failure Strain

4.5.1 Longitudinal Failure Strain

The longitudinal failure strain, ε_1^f , for the baseline material is 12% greater at cryogenic and 48% lower at elevated temperature, both compared to the room temperature value of 1.45% strain (Figure 26, Table 4). For the irradiated material, ε_1^f is 16% lower at cryogenic and 85% lower at elevated temperature than at room temperature. The ε_1^f values for the irradiated material are higher at cryogenic and room temperature, by 4% and 38%, respectively, but 59% lower at elevated temperature.

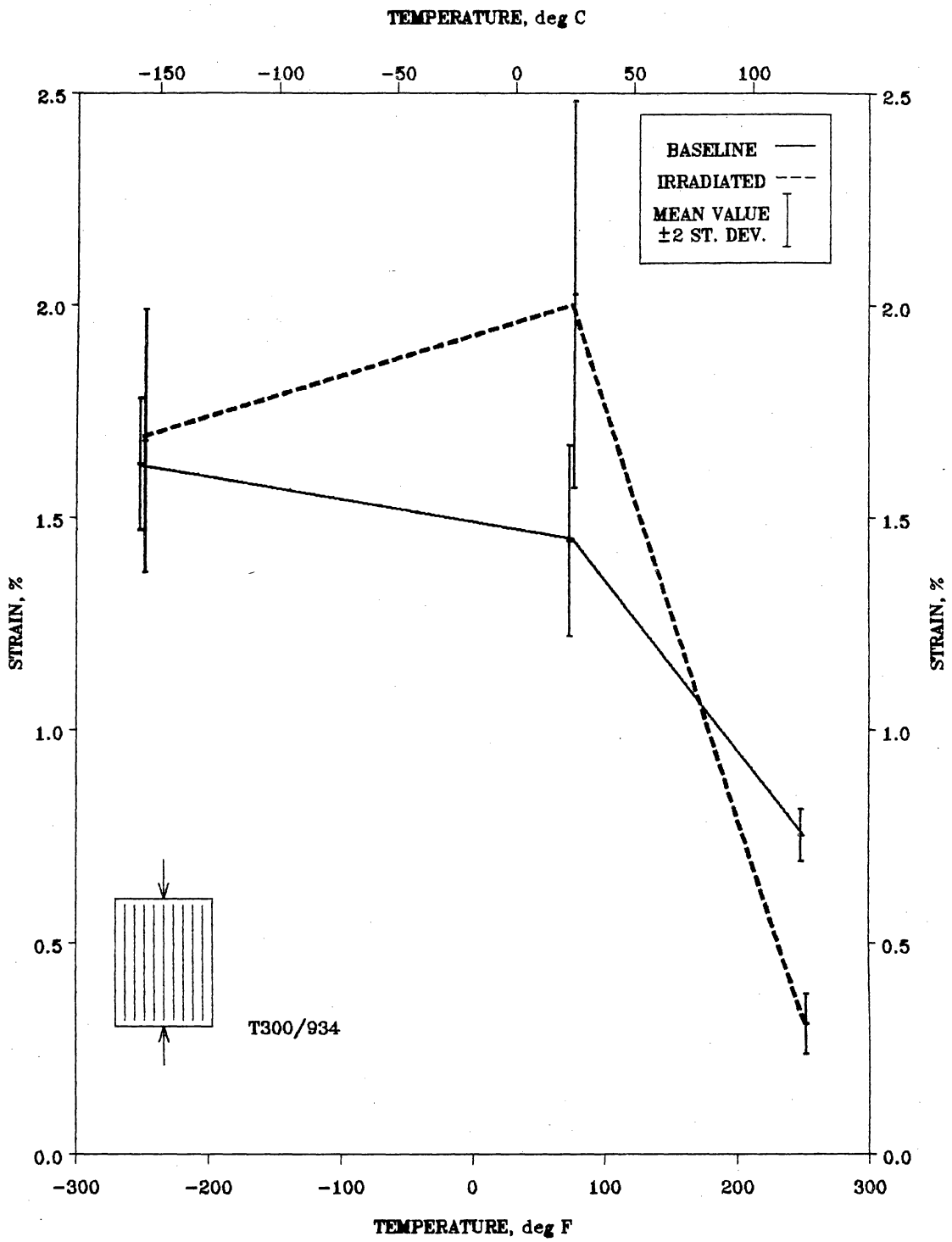

Figure 26. Longitudinal Compressive Failure Strain of T300/934 vs Temperature

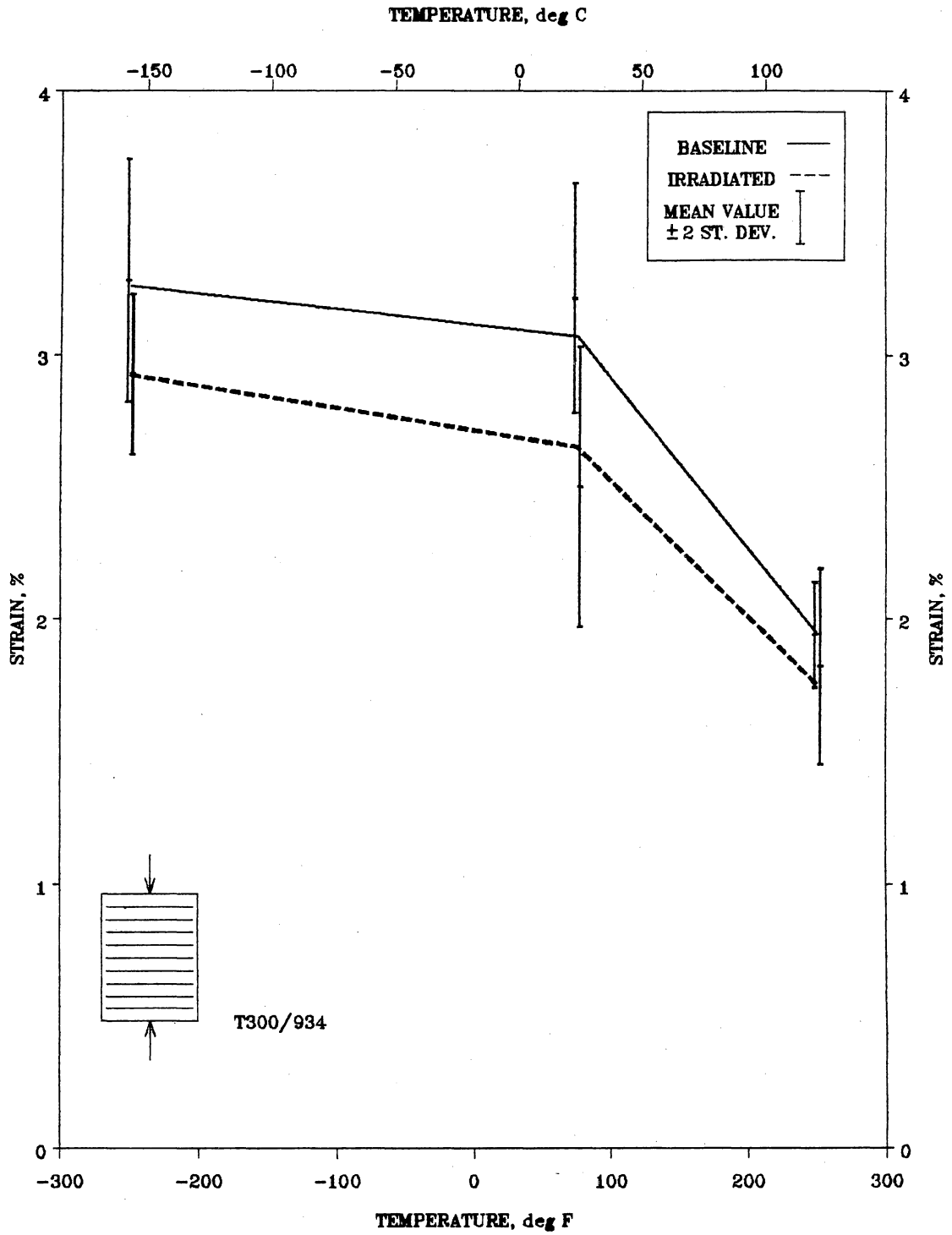

Figure 27. Transverse Compressive Failure Strain of T300/934 vs Temperature

The temperature dependence of the baseline ε_1^f values follow the same trend as the corresponding X_c values and is attributed to the same causes--improved matrix strength and stiffness at cryogenic temperature and corresponding decreases at elevated temperature. The radiation-induced increases in ε_1^f at cryogenic and room temperature are consistent with the corresponding reductions in E_1 under these conditions.

4.5.2 Transverse Failure Strain

The transverse failure strain, ε_2^f, for the baseline material is 6% higher at cryogenic and 39% lower at elevated temperature than the room temperature value of 3.07% strain (Figure 27, Table 4). The irradiated material follows the same trend, with the cryogenic value 10% higher and the elevated temperature value 34% lower than the room temperature value of 2.65% strain. The irradiated material has a lower ε_2^f at all three temperatures. The difference is -10%, -14%, and -10% at cryogenic, room, and elevated temperatures, respectively.

These results exhibit the same trends as the Y_c data--decreasing values with increasing temperatures and irradiation-induced decreases at all temperatures. The fact that irradiation reduced the transverse failure strain at all three temperatures is another indication that irradiation produces a general breakdown of the epoxy network structure.

4.6 Failure Mechanisms

As shown in the preceding section, the quantities related to material failure--strength and failure strain--were more influenced by both temperature and irradiation than were the moduli. In this section, the observed failure mechanisms will be more completely discussed. For the

purposes of establishing the quantities "strength" and "failure strain", failure was previously defined to be "the point in the mechanical test during which the maximum load was sustained by the test coupon." There are insights to be gained by reconceptualizing failure as a process and by attempting to describe that process.

Unfortunately, unidirectional Gr/Ep coupons tend to fail catastrophically and suddenly. This makes it difficult, if not impossible, to directly observe the failure process. The usual method is to infer the failure mechanism through examination of the failure surface (at both the macro- and micro-level), analogies to familiar structural failure modes, and comparison between theoretical (micromechanical) models and experimental results. This section will describe the type of compression failures observed in this study and examine some of the models used to describe the failure process.

4.6.1 Longitudinal Failure

4.6.1.1 Experimental Observations

At cryogenic and room temperature, the coupons tended to fracture across the entire width of the coupon or fail in the grip region (Figure 31b, Figure 32b). In both cases there was extensive longitudinal splitting. Examination of the failure surfaces was difficult because of the longitudinal splitting and fragmentation. For the room temperature coupons which failed in the grip region it was sometimes possible to observe what appeared to be shear crippling (to be further discussed below).

The cryogenic strength values are greater than the highest tensile strengths measured by Milkovich, et al. [3]. It has been reported in the literature [31] that the strength of carbon fibers

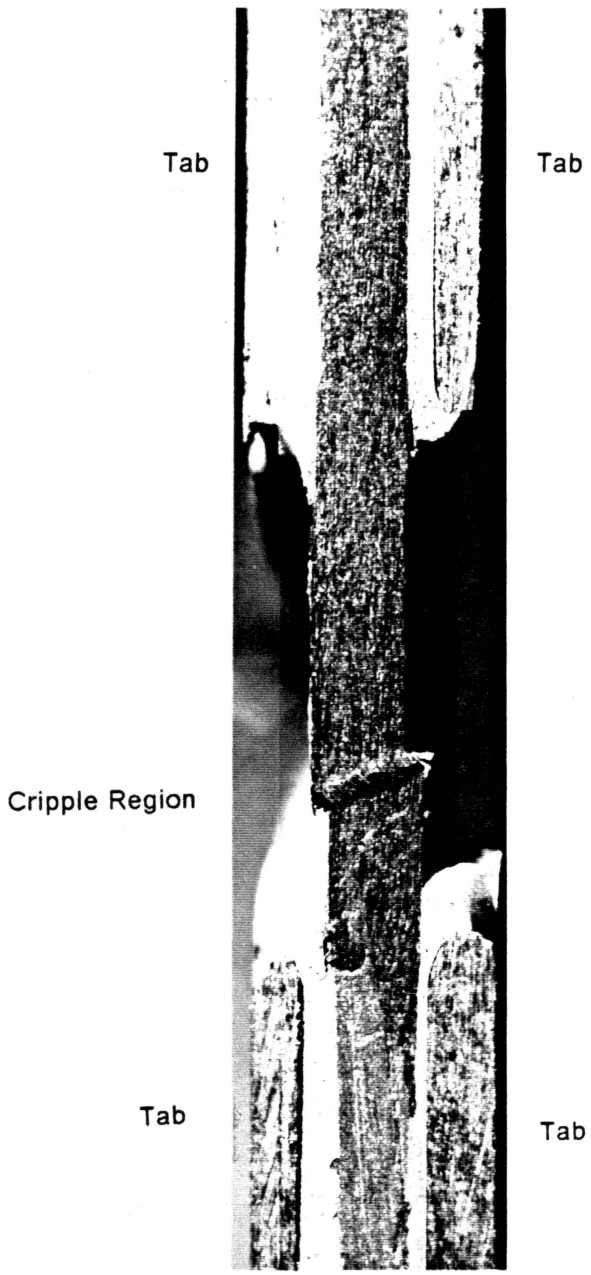

Figure 28. Shear Crippling Failure of 0° T300/934 Compression Coupon

may be lower in compression than tension due to the fiber microstructure. In a study of compressive failure mechanisms, Chamis and Sinclair [22] considered fiber compressive failure a possible failure mechanism and state that the fiber compressive strength may be taken to be 90% of the tensile strength. Making these assumptions leads to strength predictions (using simple rule of mixtures, $X_c = v_f X_f + v_m X_m$) of approximately 260-270 ksi for the composite. Because these values are relatively close to the measured strength values at cryogenic temperature (especially for the baseline material) it is reasonable to conclude that pure compressive fiber failure may be the operative failure mechanism at this temperature.

At elevated temperature (Figure 33b), the irradiated coupons clearly exhibited shear crippling failures. The type of failure shown in Figure 28 was clearly visible in three of the five coupons tested at this condition. The other two specimens tested at this condition were completely fractured (e.g. broken into two pieces) and it is suspected that the crippling region was destroyed in the wake of fracture. The baseline, elevated temperature coupons appeared to fail by extensive longitudinal splitting, as there was no clearly visible fracture area. After removal of the tabs, there was usually a fractured area near the ends of the specimen which had failed in a bearing (end crushing) mode. Microscopic examination of this area revealed existence of crippling regions similar to those referred to above. Because the failure occurred in the grip region and because it is impossible to determine whether the crippling caused the splitting or vice-versa, it is less clear whether shear crippling is the operative failure mechanism in this condition.

4.6.1.2 Compressive Strength Models

Compressive failure of unidirectional composites loaded in the fiber direction has been the subject of a large number of theoretical and experimental investigations [22-24, 32]. Several failure mechanisms have been proposed. Most models begin with a fiber microbuckling model. However, it is widely recognized that the simple microbuckling models (both the

symmetric and antisymmetric, or shear and extension, modes) yield strength values well in excess of those observed experimentally [31]. Therefore, most researchers incorporate non-linear matrix properties or initial fiber curvature--most often both. Including these effects allows the models to produce results comparable to those obtained experimentally. Unfortunately, the experimental results are inconsistent and sensitive to test method and various global failure mechanisms. In addition, the models are dependent on some parameters--in particular, initial fiber curvature--which are difficult to measure independently [24].

A recent paper by Hahn and Williams [24] presents a shear crippling mechanism which consists of the following events:

- Attainment of critical load
- Local kinking or microbuckling of a few fibers
- Formation of regions of shear crippling
- Gross composite failure

They also note the existence of other failure modes--longitudinal splitting and pure compressive fiber failure--and that the observed mode depend on "various material properties and geometrical parameters". In particular, they observe that a strong correlation exists between compressive strength and matrix modulus. They also mention that it is possible, if not likely, that kink bands in unidirectional material are destroyed in the wake of failure.

In view of the experimental evidence which has been presented and the model described above, the failure process would seem to be well understood and it would seem reasonable to assume that the longitudinal compressive strength could be calculated fairly accurately. Unfortunately, this is not the case. Because of the difficulty in independently determining some of the model parameters, most notably the characteristic size of the initial fiber imperfection, it is difficult to predict the strength a priori. A common method is to assume a

known set of "typical" values for all but one parameter, including the compressive strength and "back out" a "typical" value for the unknown parameter (i.e. initial fiber curvature). This is similar to the method presented by Tsai [20], in which he assumes knowledge of a reference state and then predicts the changes in various properties based on deviations of the relevant parameters from the reference values.

For a material with strong fibers and for which the shear stress-strain behavior can be approximated as elastic-perfectly plastic, Hahn and Williams derive the following equation:

$$X_c = v_f \frac{\tau_y}{\gamma_y + \pi \frac{f_o}{L}}$$

where

X_c	longitudinal compressive strength
v_f	fiber volume fraction
τ_y	shear yield stress
γ_y	shear yield strain
$\frac{f_o}{L}$	characteristic size of the initial fiber curvature

If γ_y is replaced by $\frac{\tau_y}{G}$, where G is the composite shear modulus, then:

$$X_c = v_f \left[\frac{G \tau_y}{\tau_y + \frac{\pi f_o}{L} G} \right]$$

Consider using the cryogenic temperature results for the baseline material as a reference state to obtain the parameter $\frac{f_o}{L}$. This choice of reference state isn't entirely arbitrary. As discussed earlier, the strength in this condition (baseline, cryogenic temperature) is very close to that obtained using a simple rules of mixtures expression.

Table 6. Compressive Strength Model Parameters and Results

Radiation Dose	Temp.	G_{12}^1 (msi)	τ_y^2 (ksi)	X_c (ksi) predicted	X_c (ksi) measured
Baseline	Cryogenic	1.17	7.34	241[3]	241
v_f=0.631	Room	0.688	7.56	199	193
	Elevated	0.563	3.94	125	126
Irradiated	Cryogenic	1.12	7.25	228	228
(10,000 Mrads)	Room	0.777	6.83	192	188
v_f=.61	Elevated	0.397	2.33	75.5	48.3

[1]from Milkovich, et al. [3]

[2]estimated from curves in [3]

[3]reference condition for predicted values

$$X_{c,\,predicted} = v_f \left[\frac{G\,\tau_y}{\tau_y + 0.0129\,G} \right]$$

The composite shear modulus was measured by Milkovich, et al. [3] and the shear yield stress can be estimated from the stress-strain plots for the 10° off-axis tests conducted in [3]. The value of all the relevant parameters are listed in Table 6.

Using the values at the reference state to "back-out" a value for the initial fiber imperfection:

$$\frac{f_o}{L} = 0.0041$$

Substituting this into the strength equation:

$$X_c = v_f \left[\frac{G\tau_y}{\tau_y + 0.0129G} \right]$$

The values calculated from this equation agree quite well with the experimental results in all but the irradiated, elevated temperature condition (Table 6).

In view of the agreement between the "predicted" and measured values, the compressive strength would seem to be easily and accurately estimated from the shear stress-strain data. This conclusion must be tempered by the realization that many of the assumptions used in deriving the strength equation have been violated in the application of it to this problem. For instance, the shear stress-strain behavior was assumed to be elastic-perfectly plastic. A cursory examination of the results of Milkovich, et al. [3] reveal this to be, at best, a gross oversimplification. In addition, the characteristic size of the imperfection has been assumed to be constant when it is likely to be effected by temperature and, possibly, irradiation.

Why then, do "the numbers" look so good? It is believed that microdamage, in particular fiber/matrix debonding and matrix microcracking, occurs during loading. The model developed in [24] and used above takes a fiber as the free body and applies the matrix reactions as equivalent loads (forces and moments). It is believed that the local microdamage, for instance fiber/matrix debonding, may produce effects similar to the effect of the matrix becom-

ing perfectly plastic. Thus the model yields the proper correlation, although the actual mechanism may not necessarily be the mechanism contained in the model.

In summary, it appears that the shear crippling mechanism provides an adequate and rational explanation for the failure of unidirectional T300/934 Gr/Ep. The mechanics of failure at the micro-level are likely to require further study, but the model seems conceptually satisfying and capable of producing excellent quantitative results as well.

4.6.2 Transverse Failure

4.6.2.1 Experimental Observations

The 90° specimens all failed, as expected, by fracturing on planes parallel to the fiber direction (Figure 31a-Figure 33a). The number of fractures observed (i.e. the number of pieces the specimen was broken into) was affected by temperature and irradiation. Cryogenic temperature tended to produce a greater number of fractures and elevated temperature a lesser number with respect to room temperature in both the baseline and irradiated conditions. In addition, the irradiated specimens tended to fracture into fewer pieces at all temperatures. This tendency was especially noticeable at elevated temperature where the coupons tended to crush slowly rather than break sharply. Many of the cryogenic and room temperature specimens exhibit "spearhead" fractures, where it appears the fracture initiated at the center of the specimen followed by the two sides shearing off independently (Figure 29b).

a) Irradiated, Elevated Temperature Coupon

b) Baseline, Room Temperature Coupon

Figure 29. Transverse Failure Angles of 90° T300/934 Compression Coupons

4.6.2.2 *Prediction of Fracture Angle*

In contrast to the extensive work on longitudinal failure modes, the transverse compressive strength has received relatively little attention in the literature. This reflects the fact that transverse compressive strength is less frequently a critical design parameter. Collings [33] investigated transverse compressive behavior in unidirectional Gr/Ep and outlined a method for estimating fracture angle. In terms of the coordinates in Figure 30, he assumed that the 2-3 plane was a plane of isotropy and that "...failure will occure on a plane where the shear stress reaches the shear strength under the corresponding normal compressive strength". Collings [33] obtained this shear strength experimentally and obtained good agreement between his predicted and experimental fracture angles.

Similar results can be obtained by applying a quadratic failure criterion to the stress state on the n-t plane (see Figure 30). For example, if the Tsai-Wu tensor polynomial is used with all interaction terms set to zero the following equation is obtained :

$$\sigma^2[F_{33} - F_{44}]\cos^4\theta + [F_3\sigma + F_{44}\sigma^2]\cos^2\theta - 1 = 0$$

Again using the assumption of transverse isotropy:

$$Z_c = Y_c \qquad Z_t = Y_t$$

$$F_3 = \frac{1}{Y_t} + \frac{1}{Y_c} \qquad F_{33} = \frac{1}{Y_t Y_c} \qquad F_{44} = \frac{1}{S_{23}^2}$$

The value of θ is obtained by setting $\sigma = Y_c$ and solving the equation for θ. Calculations reveal that θ ranges from 60-80° with the lower values corresponding to elevated temperature and higher values corresponding to cryogenic temperature.

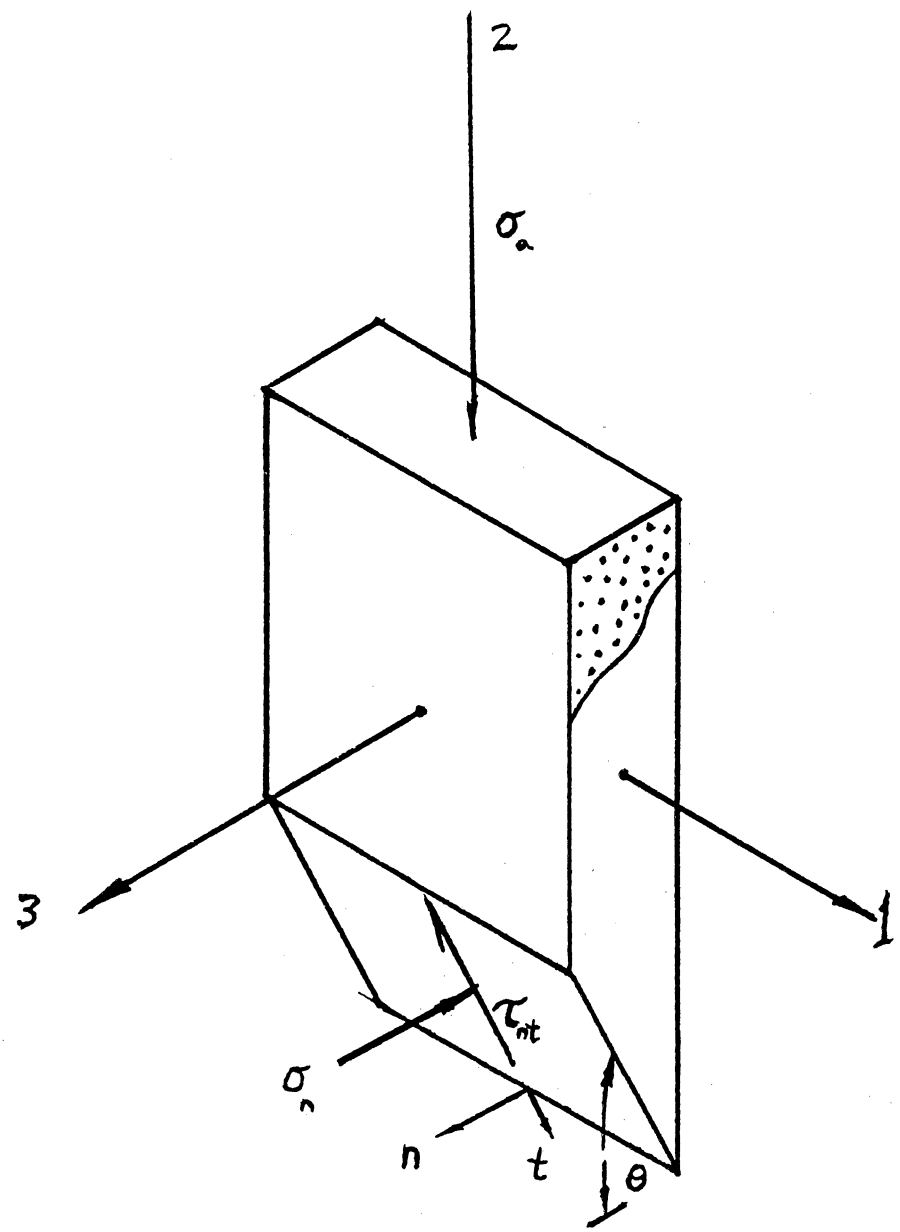

Figure 30. Geometry Used for Transverse Fracture Angle Calculations

It was not possible to determine the fracture angle accurately enough to evaluate whether they followed the calculated values quantitatively. However, they appear to follow the predicted trends (e.g the angle is generally greater at cryogenic and room temperature than at elevated temperature).

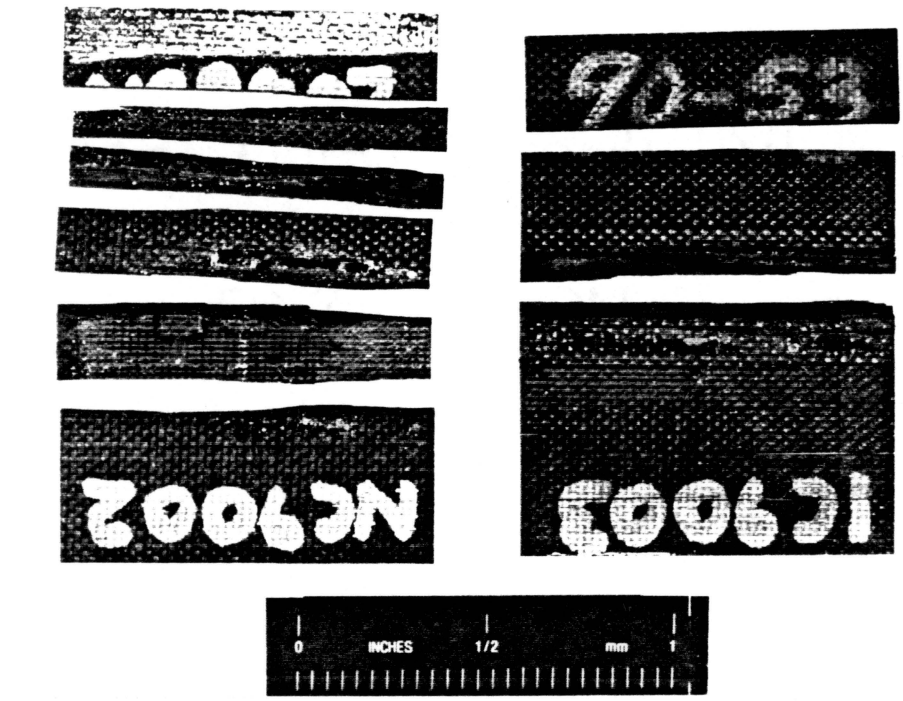

a) 90° Coupons

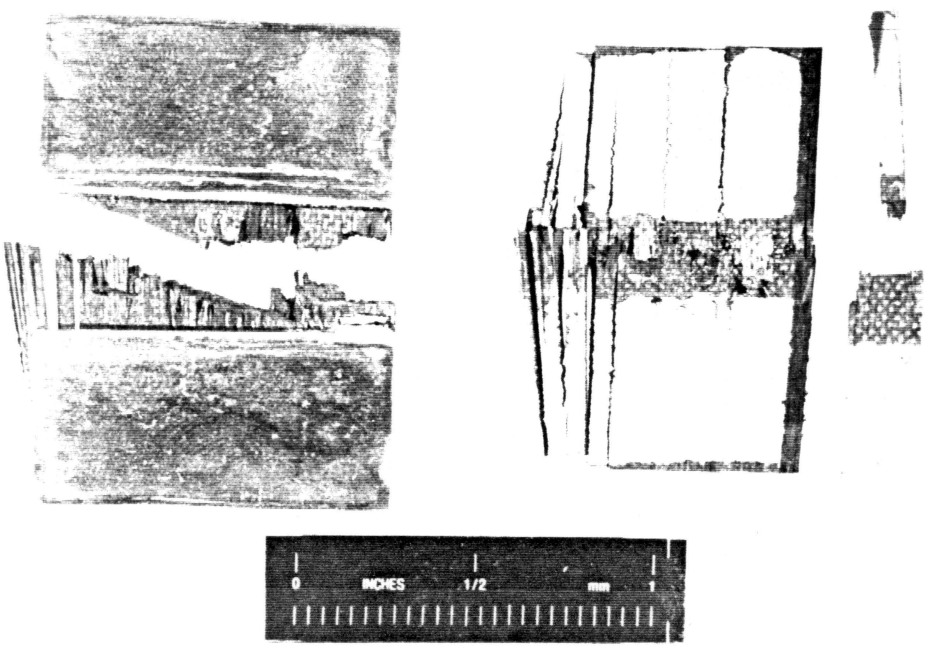

b) 0° Coupons

Figure 31. Failed Cryogenic Temperature T300/934 Compression Coupons

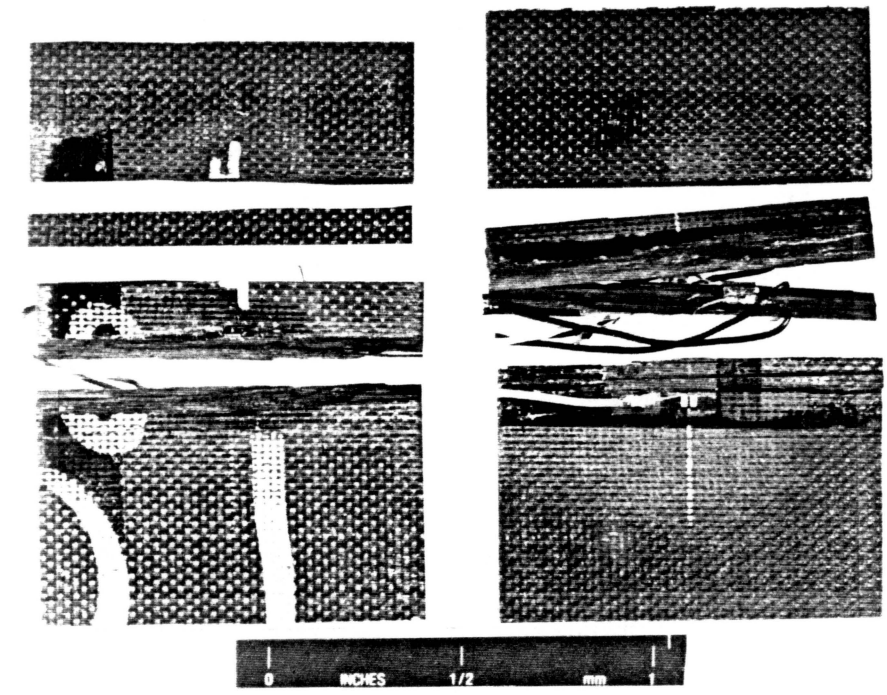

Baseline Irradiated

a) 90° Coupons

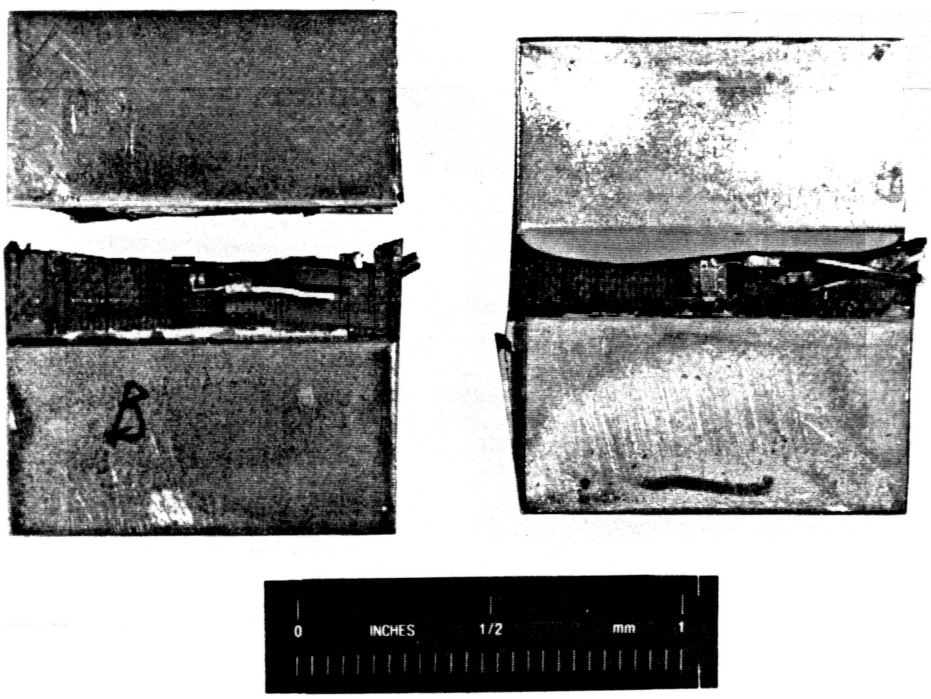

Baseline Irradiated

b) 0° Coupons

Figure 32. Failed Room Temperature T300/934 Compression Coupons

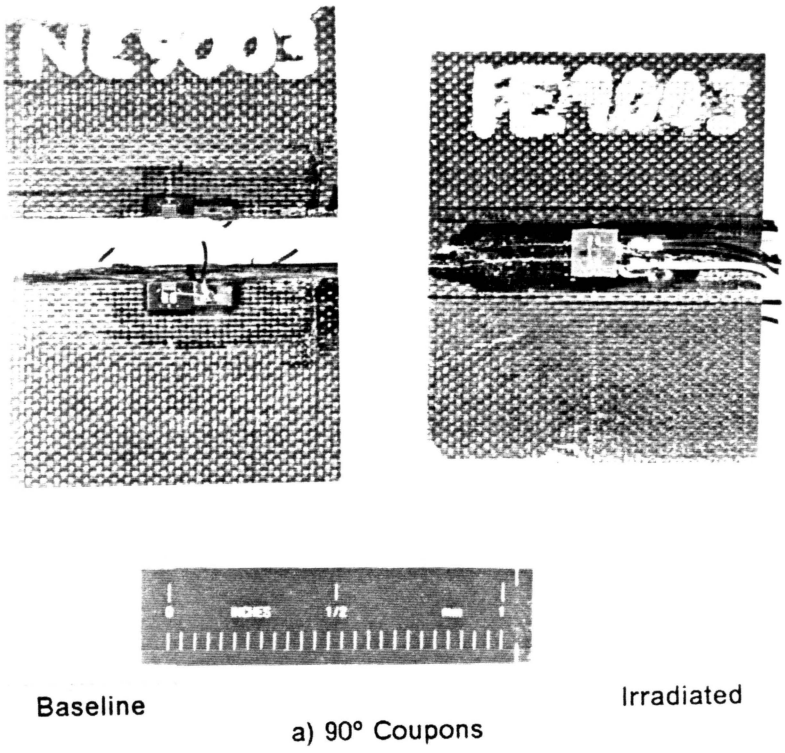

Figure 33. Failed Elevated Temperature T300/934 Compression Coupons

5.0 Neat Resin Tensile Tests

The second major thrust of this study was an investigation of the effects of elevated temperature and electron irradiation on the tensile properties of the neat (unfilled) Fiberite 934 epoxy resin. The specimen fabrication and preparation are described in detail. Following this, the test procedures and equipment are described and, finally, the results of the neat resin tests are presented and discussed. It is uncertain how closely the properties of the epoxy resin when cured in the neat (unfilled) form correlate with the properties of the resin as a matrix material in a composite. Therefore, this chapter will deal only with the neat resin properties. The next chapter will examine the use of these properties to help explain the changes observed in composite properties.

5.1 Specimen Fabrication and Preparation

The properties of all materials are dependent on the processes used to form or fabricate them. In the case of epoxy resins, it is widely recognized that the properties of the cured resin can be tailored to meet the requirements of the intended use by manipulation of the resin formu-

lation and cure cycle. Epoxies are thermosetting polymers which form strong rigid network structures with good thermal and chemical stability. The brittle nature of the epoxies can make it difficult to obtain consistent and reliable epoxy tensile test data [34].

There are two principal methods for fabricating epoxy tensile specimens--casting to net shape and machining from relatively large sheets or blocks of material. Both methods have their advantages and disadvantages. Because of the brittle nature of cast epoxies, they are difficult to machine using conventional methods [35], and it is sometimes difficult to obtain large sheets or blocks of the cured material. However Chiao, et al. [34] found these to be less serious difficulties than those encountered in casting individual specimens to net shape and recommended machining specimens from sheets. An additional advantage of this method is the ability to cut around voids or other flaws in the material.

As would be expected, the primary advantage of the other method, casting to net shape, is the avoidance of machining operations. The disadvantages of this method are the necessity to produce molds and the elimination of voids and other irregularities from the cast specimens. Additional problems can be encountered if metal molds are used, for example, the surface flaws caused by the mismatch in thermal expansion properties [34] and contamination of the surfaces by release agents [35].

After weighing all these factors, it was decided to cast specimens to net shape in silicone rubber molds. The specimen shape chosen was the small "dog-bone" specimen (type V) from ASTM Standard D638-82a [18]. The small specimen was chosen because of the limited amount of resin available and to maximize the number of specimens which could be irradiated at one time.

The remainder of this section will describe the production of molds, the casting and curing procedure and the final shaping of the cured specimens.

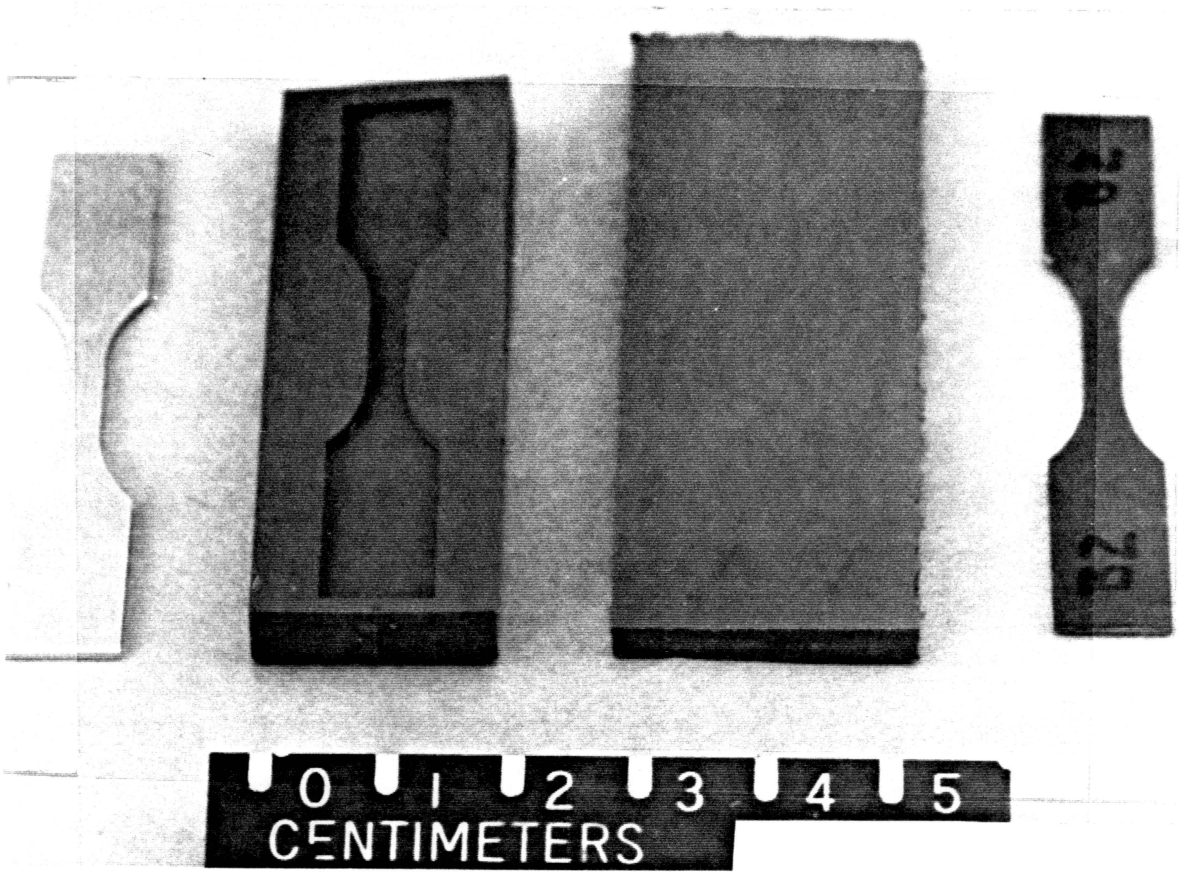

Mold Cavity

Mold Cover

Aluminum
Master Specimen

Silicone Rubber
Mold

Cast Epoxy
Specimen

Figure 34. Neat Resin Specimen Fabrication Sequence

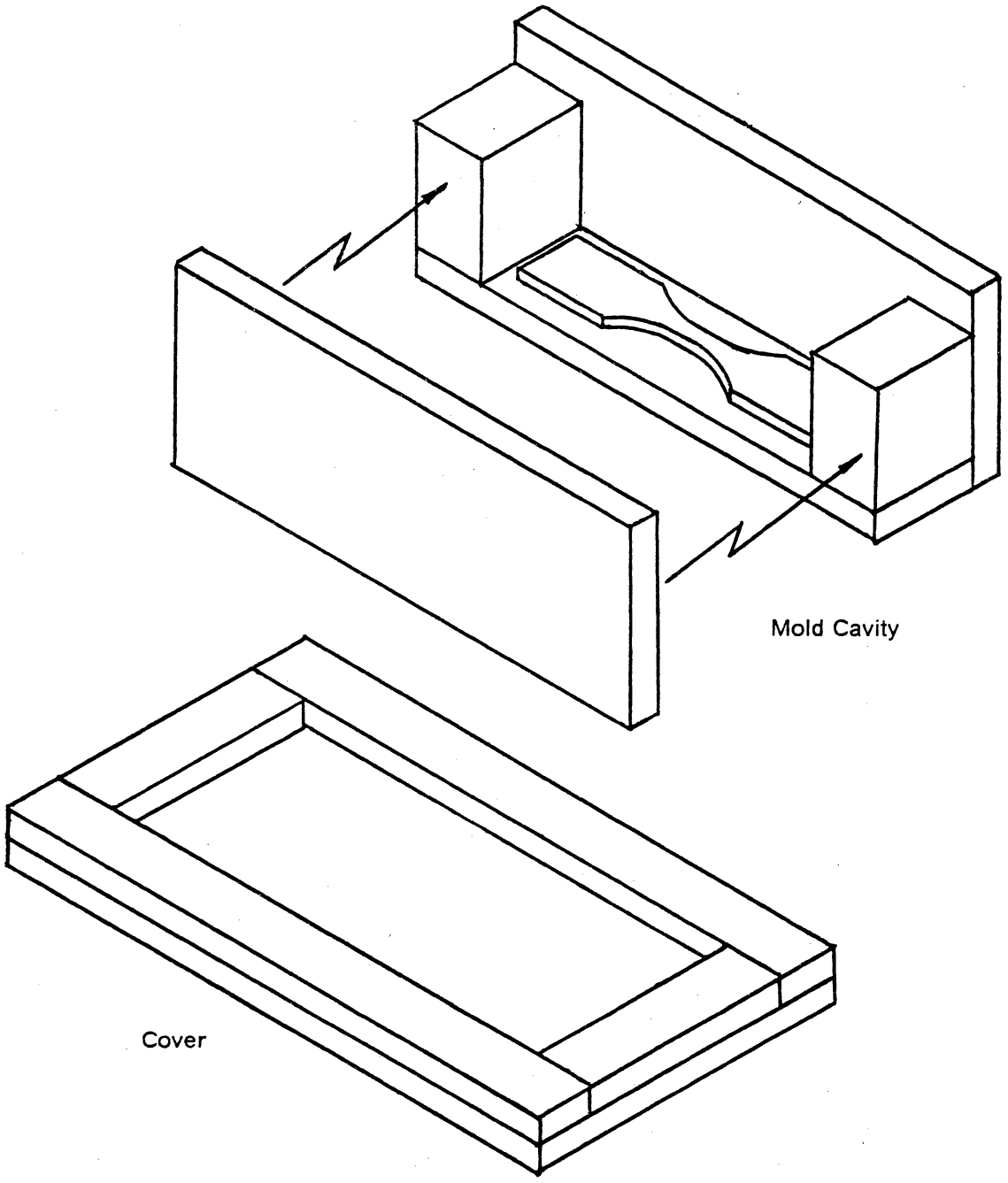

Figure 35. Method Used to Produce Neat Resin Molds

5.1.1 Mold Production

The molds were produced from silicone rubber, RTV60, in a manner based on that of Fanter [35]. An aluminum "master" specimen was fabricated according to the dimensions given in ASTM Standard D638-82a [18]. The thickness of this master specimen was 0.040". The molds consisted of two pieces--a bottom, containing the actual mold cavity and a cover, simply a flat piece of material (Figure 34). The pieces were formed by placing the master specimen in the bottom of a small box and filling this box one-half full of silicone rubber (Figure 35). The cover was molded in a shallow box at the same time. After pouring, the RTV was allowed to cure overnight at room temperature. The two pieces were then removed from their molds and postcured for 4 hours at the maximum temperature used for curing the epoxy (350° F; 177° C).

5.1.2 Casting and Curing

As noted earlier, the properties of epoxies are dependent on the cure cycle. It is particularly important to control the maximum temperature and the time at this temperature during the cure cycle. Time at maximum temperature is the factor which most influences the density of the cured material.

In the actual casting process other factors are also important. The most significant of these is the removal of solvents and entrapped gases (including water), both of which lead to void formation. The resin used in this study was in 20-30% acetone solution and solvent removal proved to be a bothersome problem.

The casting process used in this study consisted of the following steps:

- Solvent removal
- Filling open mold cavities
- Gelation
- Covering molds
- Completion of cure cycle

The casting was carried out in a Hotpack Model 734 vacuum oven; both the heat and vacuum capabilities were found to be useful for solvent removal. The specimens were cast in batches of five, with an average of three acceptable specimens being produced per batch. Approximately 12-15 ml of the liquid resin were poured into a 50 ml beaker and the beaker was then put in the cool ($< 100°$ F) oven. The resin initially had low viscosity and was easy to pour and measure. It is necessary to use a relatively large container because during processing the resin would tend to foam up to several times its quiescent volume.

The molds were thoroughly cleaned with alcohol and placed in the oven along with the beaker of resin. The oven was closed, approximately 20-25 in Hg. of vacuum were drawn, and the temperature was set at 200° F. It is important to note that the oven responded slowly to temperature changes, particularly under vacuum, and it would take a considerable length of time (1.5-2 hrs) to reach a stable 200° F temperature. The acetone would begin to boil off in the 100-150° temperature range. During this phase of the casting operation, it was necessary to watch the solution carefully to avoid boil over. Partial release of the vacuum and occasionally opening the oven and stirring the resin often helped expedite solvent removal. Higher initial vacuums tended to produce problems with violent and sudden foaming of the resin.

Once the acetone began to boil off, the vacuum could slowly be increased to 30 in Hg (1 atm). This phase often involved frequent adjustments to the vacuum pressure. Eventually, the temperature would stabilize near 200° F (100° C) and most of the bubbling would cease.

At this point the oven was opened, the molds filled, and the vacuum redrawn. As is characteristic of epoxies, the resin would usually foam up at this point. After the foam subsided this process would be repeated until the molds remained full. The temperature was then slowly increased to 250° F (121° C) and held constant until all bubbling ceased and the resin began to gel. The oven was opened and the covers were placed on the molds. The resin was extremely thick and partially cured at this point. It was desirable to cover the molds as quickly as possible to minimize the heat loss during this phase. Once all the molds were covered, the oven was closed and the temperature was raised to 350° F (177° C). This final temperature rise usually took about an hour.

The remainder of the cure cycle took place under atmospheric pressure and simply consisted of holding the oven temperature at 350° F for one hour. The oven temperature was closely monitored during this time and allowed to vary no more than ±2° F (±1.5° C). Following completion of the cure cycle, the specimens were removed from the molds, the molds cleaned, and the process begun again. It should be noted that the specimens are fragile and care should be taken in removing them from the molds to avoid breakage.

5.1.3 Final Specimen Preparation

Final shaping of the specimens consisted of trimming off the excess material ("flash") left from the casting operation and included inspection for visible voids.

The excess material was removed with a razor blade and file, with the final sanding of the edges accomplished with 400 grit sandpaper. Considerable care was taken to ensure that the finishing strokes were made parallel to the long axis of the specimen (i.e. in the load direction). This finishing process involved only the edges of the specimens. The top and bottom cast surfaces were smooth and didn't require further polishing or sanding.

Following this preparation, the specimens were slowly heated to 350° F (177° C) in a forced air oven, held at this temperature for an hour, and slowly cooled to room temperature. The specimens were placed between smooth glass plates during this process. This thermal cycle was an attempt to "even-out" the small differences in cure cycles between different batches of specimens.

The width and thickness of all specimens were measured to the nearest 0.001 in (0.025 mm) at three locations in the test section: in the center and near the ends of the narrow section. These measurements were found to vary $<$ 0.003 in ($<$ .08 mm) between the three locations. The averages of the three measurements were used to calculate the cross-sectional area for stress calculations.

5.1.4 Instrumentation

The neat resin tensile specimens were each instrumented with three electrical resistance strain gages. Two of the gages (Micro-Measurements EA-06-062AQ-350) were mounted, back-to-back and centered in the test section, in the load direction. The remaining gage (Micro-Measurements EA-06-045AL-350) was oriented transverse to the load direction and above one of the longitudinal gages. All gages were entirely within the narrow test section of the specimens. The two longitudinal gages allowed thru-the-thickness strain variation, due to either bending loads or initial specimen curvature, to be averaged out. The transverse gage was used to determine Poisson's ratio.

All gages were bonded using Micro-Measurements Strain Gage Adhesive AE-15. The adhesive was cured at 120° F (49° C) for six hours under 15 psi (103 Pa) pressure. Typical instrumented specimens are shown in Figure 36.

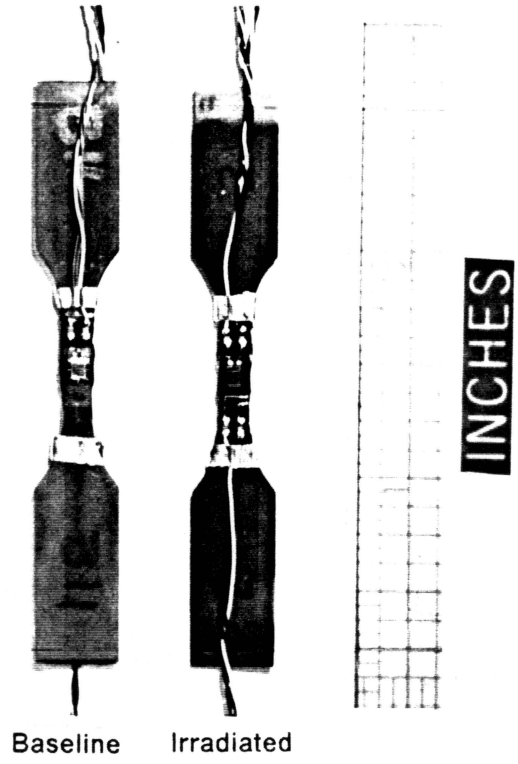

Figure 36. Instrumented Fiberite 934 Tensile Specimens

5.2 Test Method

The test method was relatively simple compared to that used for the compression tests described earlier. All the neat resin tests were conducted at Virginia Tech using a servo-hydraulic Instron testing machine (model 1351) with a 20 kip load frame. A 2 kip load cell was "piggy-backed" in the load train to allow accurate measurement of the small loads involved in these tests.

The specimen grips were made of aluminum and were held against the specimen by four screws (Figure 37). The grip faces were lined with Crocus cloth to prevent slippage. The specimen was installed in the grips using an alignment jig which ensured constant grip separation and facilitated accurate centering of the specimen. All joints used to connect the grips to the load train of the testing machine were made with pin connections. All tests were conducted under stroke (displacement) control at a constant rate of 0.033 in/min (0.85 mm/min).

An ATS environmental chamber was mounted in the test machine for the elevated temperature tests. This chamber provides heat by forced convection of air over electrical resistance heating coils. Temperature was monitored using a K-type thermocouple attached to the specimen grips.

The strain gage and load cell data were acquired using an Orion Datalogger and IBM PC-AT. The Orion employs a constant current type Wheatstone bridge and provides bridge excitation only during the actual strain measurement. This minimizes the effects of self-heating of the strain gages. The data are converted to stress and strain units during data acquisition and a stress-strain curve is generated using a software package developed at Virginia Tech, MATPACO. After testing the data were uploaded to the IBM mainframe at Virginia Tech for further analysis.

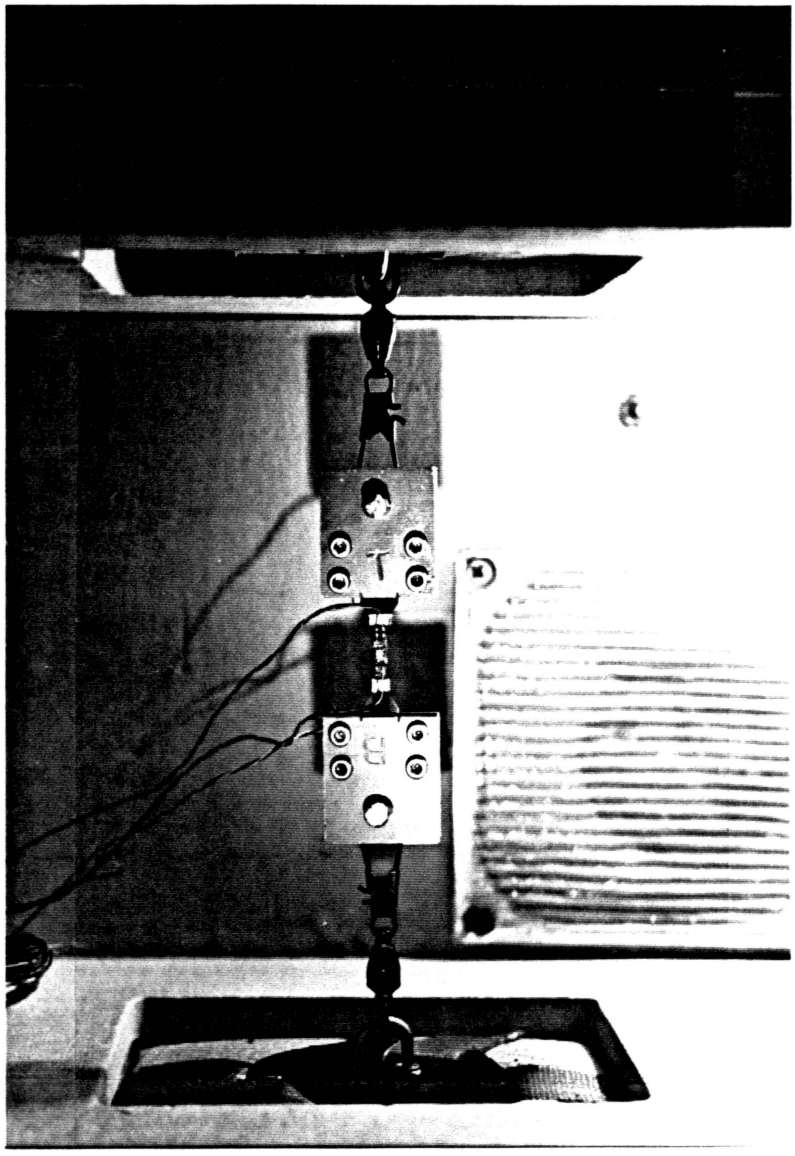

Figure 37. Fiberite 934 Tensile Specimen Prepared for Testing

5.3 Data Reduction and Analysis

The data reduction and analysis calculations were similar to those used for the compression test data. The strain gage data were corrected for transverse sensitivity and averaged to eliminate the effects of thru-the-thickness strain variation as previously described (Chapter 3, Appendix C). Three replicate tests were run at each condition (Table 7). The test data and the detailed test results are presented in Appendix B.

5.3.1 Consideration of Reinforcement Effects

The use of strain gages on low modulus materials and thin sections often raises the question of reinforcement effects. That is, to what degree does the presence of the strain gage alter the very strain state that the gage is intended to measure? There are, in general, two types of reinforcement: local and global. When the overall stiffness of the gage is of the same order as that of the test specimen, the gage carries a non-negligible portion of the load and this is called global reinforcement. Local reinforcement refers to strain transmission errors due to shear lag at the specimen/gage interface. This type of reinforcement can be a problem even on large sheets of low modulus materials since the gage itself produces local perturbations in the strain field. Perry [36] provides an excellent discussion of these and other difficulties which limit the accuracy of strain gage measurements.

In the present situation, the thickness and width of the strain gage and specimen are of the same order, additionally the effective modulus of the strain gage is actually somewhat higher than that of the specimen. This presents an almost perfect case of global reinforcement. The following analysis was conducted in order to gain a quantitative idea of the probable error in the calculated material properties.

Table 7. Fiberite 934 Tensile Test Matrix

Radiation Dose	Temp ° F (° C)	Number of Tests
Baseline (non-irradiated)	Room	3
	250 (121)	3
Irradiated (10,000 Mrads)	Room	3
	250 (121)	3

Test: Monotonic Tension

Material: Neat Fiberite 934 Epoxy

Specimen: ASTM D638-82a Type V

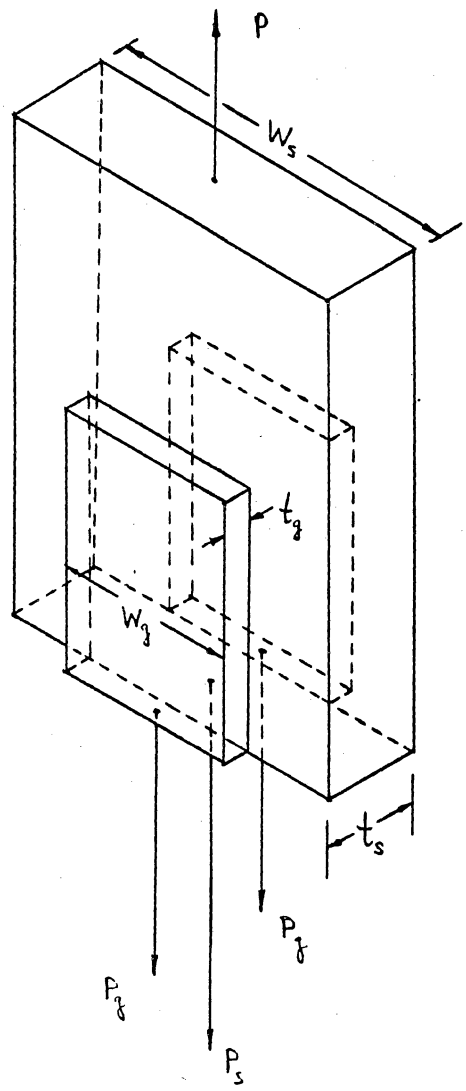

$\hat{\varepsilon}_x$ = measured longitudinal strain

$\hat{\varepsilon}_y$ = measured transverse strain

A_g = cross-sectional area of strain gage = $t_g w_g$

A_s = cross-sectional area of specimen = $t_s w_s$

Figure 38. Geometry for Consideration of Strain Gage Reinforcement Effects

Assume that the total applied force, P, is shared by the gages, P_g, and the specimen, P_s, in the area under the gages (Figure 38).

$$P = P_s + 2P_g$$

Assume that the gages have isotropic effective properties and are in a state of uniform plane stress. Using Hookes Law,

$$P_g = \sigma_g A_g = \frac{A_g E_g}{(1 - \nu_g^2)}[\hat{\varepsilon}_x + \nu_g \hat{\varepsilon}_y]$$

If the specimen is also assumed to be in a uniform state of plane stress, σ_s ,

$$P = \sigma_s A_s + 2\sigma_g A_g$$

$$\sigma_s = \frac{P}{A_s} - \frac{2E_g}{(1 - \nu_g^2)}\left[\frac{A_g}{A_s}\right][\hat{\varepsilon}_x + \nu_g \hat{\varepsilon}_y]$$

The above equation allows for the correction of the stress value to more accurately reflect the stress in the specimen. Note that if the width of the specimen and the strain gages are equal this equation can be derived using classical lamination theory. The above equation corrects for the reinforcement due to elastic modulus mismatch, but not Poisson ratio mismatch. If the specimen and gage are assumed to be the same width it can easily be shown that this affect is negligibly small for isotropic materials. For orthotropic materials, the Poisson's ratio can be quite small in some directions (i.e. ν_{21}) and the Poisson's ratio mismatch becomes a more important problem.

It should be noted that the above analysis is very simplified and doesn't consider the fact that the strain gage reinforcement occurs over a small portion of the specimen length and neglects transverse shear deformation.

Calculations using the above equation and effective gage properties (obtained from Micro-Measurements) reveal that the error in neglecting the reinforcement effect is < 10% in magnitude and is negative in sign. Thus, the true modulus of the specimen is likely to be somewhat less than the apparent modulus calculated by ignoring reinforcement effects. The magnitude of the error is inversely related to the specimen modulus (e.g. the magnitude of the error increases as the specimen modulus decreases).

For the results to be presented below, the reinforcement effect was not taken into account and the stress used in calculations was simply P/A. Therefore, the quoted modulus values are probably somewhat higher than the true modulus of the material, particularly at elevated temperature.

5.4 Results

This section presents the results of the Fiberite 934 neat resin tensile tests. For convenience, the properties are tabulated in Table 8. The stress-strain curves for all conditions are shown in Figure 39 and the Poisson response in Figure 40.

After irradiation there was a dramatic color change in the specimens. Prior to irradiation they were transparent and an amber, slightly reddish, color. During irradiation they became dark and virtually opaque. In very thin sections (i.e. near bubbles), it was possible to see through the material and it was a very deep green color.

Table 8. Fiberite 934 Tensile Properties

		Baseline		Irradiated		
Temp	Prop	Value	$\%\Delta_{RT}$	Value	$\%\Delta_{RT}$	$\%\Delta_{IR}$
Room	E (msi)	0.674	---	0.799	---	+19
	ν	0.363	---	0.373	---	+3
	G (msi)	0.247	---	0.291	---	+18
	σ_{PL} (ksi)	3.42	---	5.15	---	+51
	σ_{ult} (ksi)	8.53	---	10.9	---	+28
	ε_{ult} (%)	1.48	---	1.55	---	+5
+250° F	E (msi)	0.489	-27	0.501	-37	+2
	ν	0.341	-6	0.368	-1	+7
	G (msi)	0.182	-26	0.183	-37	n.c.
	σ_{PL} (ksi)	2.44	-29	1.34	-74	-45
	σ_{max} (ksi)	10.3	+21	6.61	-39	-36
	ε_{max} (%)	3.05	+106	2.54	+64	-17

$\%\Delta_{RT}$ = percent change w.r.t room temperature value

$\%\Delta_{IR}$ = percent change of irradiated w.r.t. baseline value

$$G = \frac{E}{2(1 + \nu)}$$

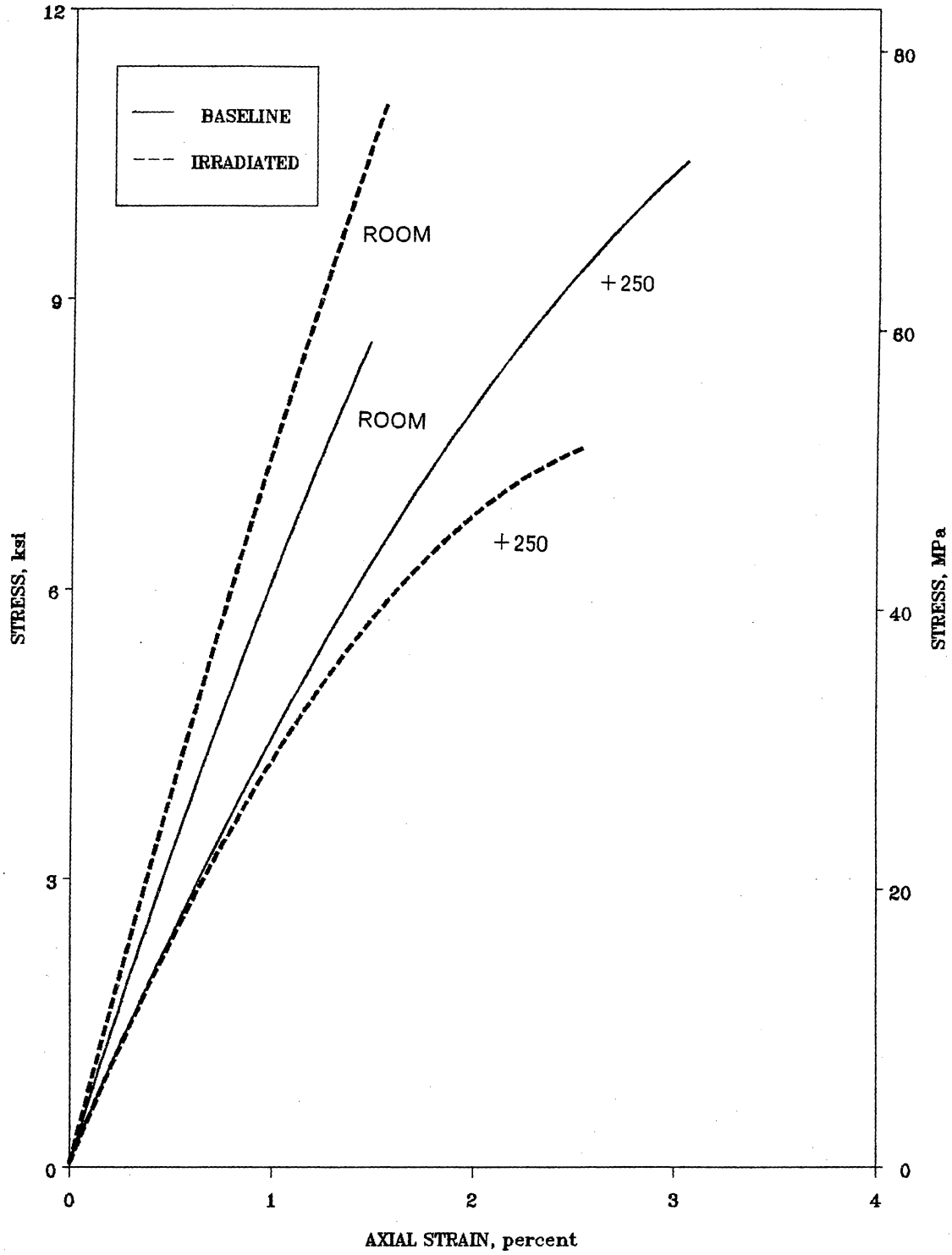

Figure 39. Fiberite 934 Tensile Stress-Strain Response

5.4.1 Young's Modulus

Young's modulus, E, is significantly affected by both temperature and irradiation (Figure 39, Table 8). The modulus of the baseline material is 27% lower at elevated than at room temperature. The irradiated material behaves similarly, with a 37% lower modulus at elevated than at room temperature. The irradiated material has a higher modulus than the baseline at both temperatures. The difference is 19% at room temperature and 2% at elevated temperature. It should be noted that at elevated temperature, the irradiated material behaves more non-linearly than the baseline material.

The decreases in E at elevated temperature are expected and consistent with the known effect of temperature on polymeric materials. Based on the results of the composite tests, it was expected that a more substantial reduction in the modulus of the irradiated material would occur at elevated temperature. The discrepancy between expected and actual behavior is believed to be a result of differences in the structure of the epoxy when cured in the presence of fibers and when cured in the neat (unfilled) form or to differences in the material/radiation interaction between the composite and neat resin materials. The neat material has a somewhat higher softening point than the composite. Therefore, the composite is nearer to its T_g at the elevated test temperature (250° F; 121° C) than is the neat resin.

5.4.2 Poisson's Ratio

The Poisson's ratio was little affected by either temperature or irradiation (Table 8, Figure 40). The values at elevated temperature were 6% lower for the baseline material and 1% lower for the irradiated material (w.r.t. the corresponding room temperature values). The irradiated specimens had higher Poisson's ratios at room and elevated temperatures, by 3% and 9%, respectively, than the corresponding baseline specimens.

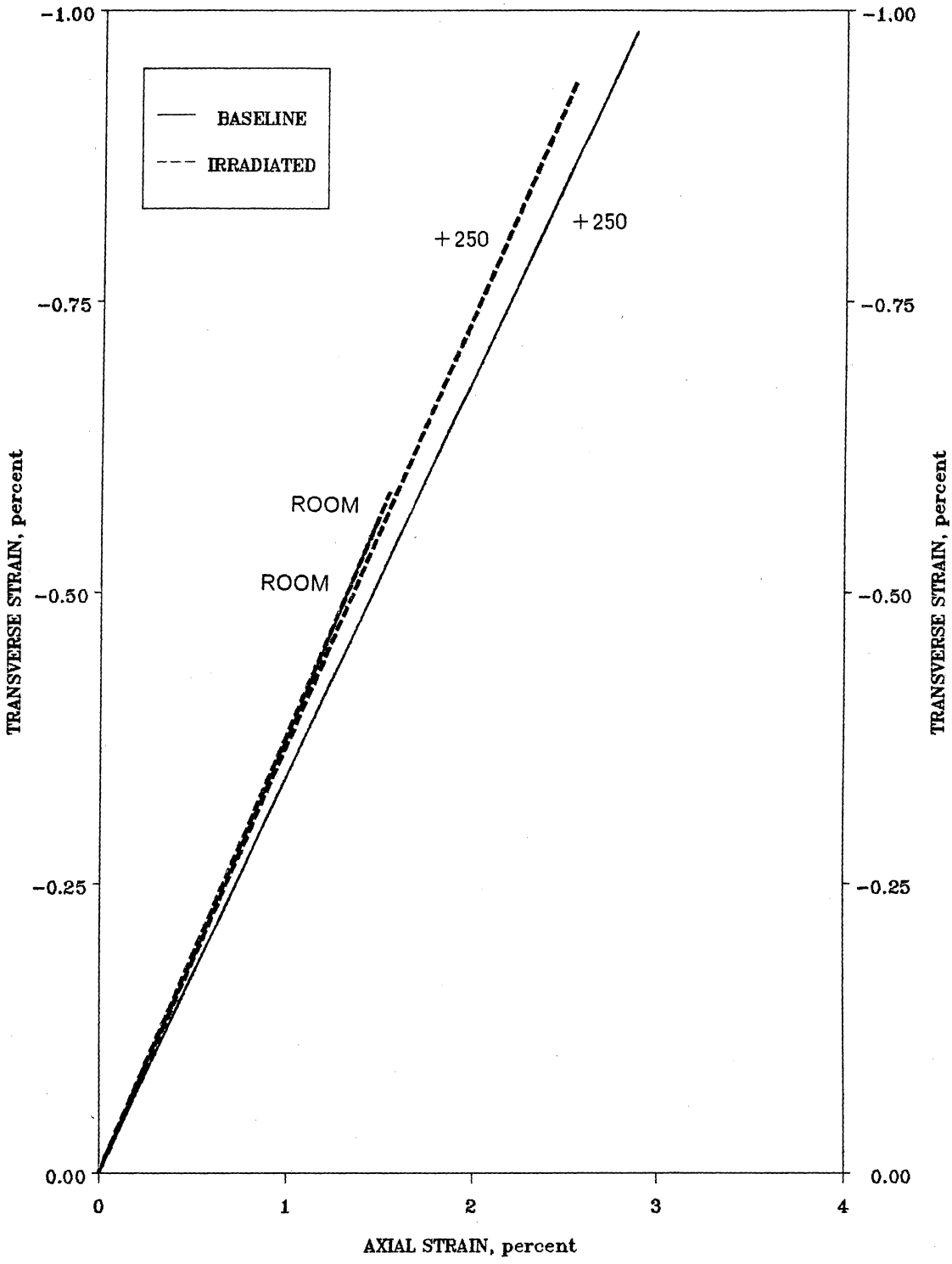

Figure 40. Fiberite 934 Tensile Poisson Response

The Poisson response was essentially linear and the values were were consistent, 5% coefficient of variation or less, in all conditions. (Figure 40, Appendix B)

5.4.3 Shear Modulus

The shear modulus, G, was calculated using the measured values of E and v and the E, G, v relationship for isotropic, elastic materials ($G = \frac{E}{2(1 + v)}$). The changes in G are essentially the same as those in E. This is result of the nearly constant value of v in all conditions. The scatter in the shear modulus values is modest with less than 5% coefficient of variation in all conditions.

5.4.4 Ultimate Stress

The ultimate tensile stress of the baseline specimens was 21% higher at elevated temperature with respect to the room temperature value (Table 8). The irradiated material exhibited the opposite behavior, with the elevated temperature value being 39% lower than the room temperature value. At room temperature, σ_{ult} was 28% higher for the irradiated specimens, while at elevated temperature it was 39% lower for the baseline specimens.

There was considerable scatter in the ultimate stress data at elevated temperature. It is uncertain whether this scatter was coincidental or related to the temperature. All specimens failed at the edges of the strain gages or solder tabs. It is believed that one of the by-products of the strain gage reinforcement effect was the creation of what is essentially a re-entrant corner at these locations. In addition, it is possible that the specimens sustained local damage during gage installation (i.e. during surface preparation or soldering). In view of these

considerations, the measured maximum stresses may not accurately reflect the strength of the material.

5.4.5 Ultimate Strain

The ultimate tensile strain was greater at elevated temperature in both the baseline and irradiated specimens, by 10% and 65%, respectively (Table 8). The irradiated specimens had a 5% higher ultimate strain at room temperature and 17% lower failure strain at elevated temperature than the corresponding baseline specimens.

The ultimate strain values, like the strength values, exhibited significant scatter at elevated temperature. The comments made in the discussion of tensile strength apply equally to the results of this section.

5.4.6 Proportional Limit

The proportional limit, σ_{PL}, is the stress level at which the stress-strain response deviates from linearity. The proportional limit was lower, in both the baseline and irradiated material, at elevated temperature, by 29% and 74%, respectively. At room temperature, σ_{PL} of the irradiated material was 28% greater than that of the baseline material. At elevated temperature, however, the irradiated material exhibited a 45% lower σ_{PL} than the baseline material.

In contrast to the strength and ultimate strain, the values of σ_{PL} were consistent. The coefficients of variation were less than 5% in all except the irradiated, elevated temperature condition where it was 14%.

6.0 Discussion

This chapter will discuss the results in this study and how they relate to the previous work of Milkovich, et al. [3] and Reed, et al. [7]. In particular, the tensile and compressive properties of the T300/934 composite will be compared and the neat resin results will be compared to the relevant composite properties.

6.1 Comparison of Tensile and Compressive Composite Properties

In this section the trends in the composite properties, under tensile and compressive loading, will be discussed. The tensile properties, unless otherwise noted, are those reported by Milkovich, et al. [3] and the compressive properties are those obtained during this study.

The tensile and compressive properties exhibit similar trends at elevated temperature, but opposite trends at cryogenic temperature. In comparing the baseline and irradiated proper-

ties, the trends are reasonably similar at all temperatures. The compressive properties, in general, show a greater change with respect to both temperature and irradiation. For clarity, the tension and compression properties will be denoted by "t" and "c" subscripts, respectively. The results for each of the properties measured in both studies will now be summarized. For convenient reference, the tensile and compressive properties are presented in Table 9.

- E_1: In tension, E_{1t}, is virtually unaffected by temperature with less than 5% variation in all cases. In compression, E_{1c}, shows somewhat more variation with 10% increases at cryogenic temperature in both the irradiated and baseline conditions. In all cases, E_{1t} is greater than E_{1c}.
- E_2: The trends in transverse modulus are similar in tension and compression. The transverse modulus increased 23-39% at cryogenic temperature with E_{2t} increasing more than E_{2c}. For the baseline material at elevated temperature, E_{2t} was 10% lower and E_{2c} 10% higher than their respective room temperature values. For the irradiated material, however both E_{2t} and E_{2c} were reduced, by -30% and -62%, respectively. The irradiated material had a higher transverse modulus (in tension and compression) at cryogenic and room temperatures than the baseline material. Similarly, both E_{2t} and E_{2c} were lower for the irradiated material at elevated temperature. In all conditions, except for the irradiated material at elevated temperature, E_{2t} is lower than E_{2c}.
- ν_{12}: Poisson's ratio was significantly affected by temperature and irradiation in tension and compression. The value of ν_{12c} decreased at cryogenic temperature, but the value of ν_{12t} increased (or was unchanged). Both ν_{12c} and ν_{12t} increased at elevated temperature, however, the percentage increases in ν_{12c} were much larger than those in ν_{12t}. The irradiated material had lower ν_{12} at room temperature and higher ν_{12} at elevated temperature (compared to the baseline), in tension and compression. At cryogenic temperature, the irradiated material exhibited a higher ν_{12t}, but a lower ν_{12c}. In all cases ν_{12t} was greater than ν_{12c}. Some of the reasons for this were discussed in Chapter 4.

Table 9. Tensile and Compressive Properties of T300/934

		Baseline				Irradiated					
		Tension*		Compression		Tension*		Compression		Δ_{IR}%	
Temp	Prop		Δ_{RT}%		Δ_{RT}%		Δ_{RT}%		Δ_{RT}%	Tens.*	Comp.
	X	141	-36	241	25	127	-43	228	21	10	-5
	Y	4.56	-51	56.5	86	2.81	-60	51.8	97	-38	-8
	S	7.34	-26	---	---	7.25	-22	---	---	-1.2	---
-250°F	E_1	18.6	-1.6	17.2	11	19.2	n.c.	16.0	10	3.2	-7
	E_2	1.83	33	2.10	29	2.12	39	2.14	23	16	2
	ν_{12}	0.313	n.c.	0.136	-25	0.368	30	0.104	-32	18	-24
	ν_{21}	---	---	0.0320	-13	---	---	0.0324	-28	---	1
	G_{12}	1.17	70	---	---	1.12	44	---	---	-4.3	---
	X	222	---	193	---	223	---	188	---	n.c.	-3
	Y	9.37	---	30.4	---	6.98	---	26.3	---	-26	-13
	S	9.92	---	---	---	9.25	---	---	---	-6.8	---
Room	E_1	18.9	---	15.5	---	19.3	---	14.6	---	2.1	-6
	E_2	1.38	---	1.63	---	1.52	---	1.74	---	10	7
	ν_{12}	0.314	---	0.182	---	0.283	---	0.153	---	-10	-16
	ν_{21}	---	---	0.0366	---	---	---	0.0447	---	---	22
	G_{12}	0.688	---	---	---	0.777	---	---	---	13	---
	X	194	-13	126	-35	162	-27	48.3	-74	-16	-62
	Y	6.76	-28	18.9	-37	5.88	-16	8.71	-67	-13	-54
	S	5.97	-40	---	---	4.06	-56	---	---	-32	---
250°F	E_1	19.0	n.c.	15.0	-3	19.8	2.6	14.4	-1	4.2	-4
	E_2	1.24	-10	1.80	10	1.06	-30	0.666	-62	-15	-63
	ν_{12}	0.345	9.9	0.309	70	0.397	40	0.384	151	15	24
	ν_{21}	---	---	0.0791	116	---	---	0.239	435	---	237
	G_{12}	0.563	-18	---	---	0.397	-49	---	---	-29	---

All properties in U.S. Customary units (e.g. strengths in ksi, moduli in msi, and strains in percent)

Δ_{RT}% percent change from room temperature value

Δ_{IR}% percent change of irradiated w.r.t baseline value

* Tensile properties the results of Milkovich, et al. [3]

- X: Longitudinal strength was reduced at elevated temperature in both tension and compression. The percentage decrease for compression was three times larger than for tension. At cryogenic temperature, however, X_t was significantly reduced (36-43%) while X_c was significantly increased (21-25%). In all cases, irradiation reduced (from 0 to -54%) the longitudinal strength. The tensile strengths are higher than the corresponding compressive strengths at room and elevated temperature, but lower at cryogenic temperature.
- Y: The transverse strength was effected in much the same way as the longitudinal strength. That is, both Y_t and Y_c were lower at elevated temperature, while the tensile strength was lower and the compressive strength higher at cryogenic temperature. The irradiated material had lower transverse strength, Y_t and Y_c, at all temperatures. In all conditions, Y_c was significantly greater than Y_t.

The changes in properties observed at cryogenic temperature are believed to be the result of matrix "embrittlement". As the temperature is decreased, the matrix becomes more rigid and this leads to increases in moduli, but decreases in tensile strength. It is common for brittle materials to exhibit considerably higher strength in compression than in tension.

A similar argument can be made about softening of the matrix at elevated temperature. The decreases in modulus and in tensile and compressive strengths are characteristics of softened materials.

Irradiation degraded the modulus and strength at all temperatures, with the exception of transverse modulus at room and cryogenic temperature. The effects of irradiation were particularly pronounced on compressive properties at elevated temperature.

6.2 Comparison of Neat Resin and Composite Properties

As noted in the last Chapter, the difference in epoxy properties when cured in neat form and as a matrix material in a composite is uncertain. For the purposes of this discussion, it will be assumed that the properties behave similarly in both cases even if the actual values are somewhat different. As in the last section, the tensile and compressive composite properties will be denoted by "t" and "c" subscripts, respectively. In addition, the neat Fiberite 934 resin properties will be denoted by the subscript "nr".

The matrix properties obviously effect the transverse and shear properties more than the longitudinal tensile properties. It is widely recognized that the longitudinal compressive strength is dependent on matrix properties, although the exact form of the relationship remains elusive.

The room temperature increase in E_{nr} following irradiation is one of the most interesting results obtained. Both the tensile [3] and compressive (Chapter 4) transverse moduli, E_{2t} and E_{2c}, were higher in the irradiated material at room and cryogenic temperatures. The increase in E_{nr} provides a simple and direct explanation for this phenomena at room temperature. It is not unreasonable to assume that the difference at cryogenic temperature is similarly due to a radiation-induced increase in the matrix modulus.

As noted in Chapter 5, E_{nr} of irradiated material did not decrease, as it was expected to, at elevated temperature. However, the softening point of the neat resin material is higher than that of the composite, probably reflecting a somewhat higher degree of cross-linking or greater average molecular weight than that of the composite. Additionally, the irradiated neat resin material behaves more non-linearly than the baseline material. The presence of residual curing stresses, even at the elevated test temperature, may be enough to push the matrix material into the nonlinear range early (or even initially) in the loading. Thus, the effective

modulus of the matrix material, in situ, may be lower than the modulus of the neat resin material. This is an example of the importance of remembering that the matrix (and fibers) in a composite are not in a stress-free condition.

The decrease in composite transverse moduli at elevated temperature (compared to room temperature) is consistent with the decrease in E_{nr} at elevated temperature. It should be noted that E_{2c} for the baseline material increased at elevated temperature. This effect remains unexplained.

The trends in G_{12} [3] are similar to those in E_{2t} and can be explained by changes in G_{nr}, analogous to those in E_{nr} used to explain the E_{2t} results. For example, the higher G_{12} for the irradiated material at room temperature compares well with the corresponding increase in G_{nr}. Additionally, the increased nonlinearity of the $\sigma - \varepsilon$ response of the 10° and 45° off-axis tensile coupons [3] compares well with similar changes in the $\sigma - \varepsilon$ response of the neat resin (assuming the shear and axial stress-strain behavior of the neat resin are qualitatively similar).

The prediction of composite strength using micromechanics is more difficult than the prediction of elastic constants, particularly for transverse and shear properties. Additionally, as noted in Chapter 5, there remains some question about how well the measured maximum stresses represent the tensile strength of the matrix. For these reasons, it is probably unwise to draw conclusions about the relationship between the composite strength properties and the neat resin tensile strength.

It is often assumed that longitudinal compressive strength is related to the matrix shear modulus ([22], Chapter 4). Comparison of the trends in X_c and G_{nr} lead to mixed results. The neat resin shear modulus, G_{nr}, increases significantly at room temperature although the compressive strength decreases slightly. Both G_{nr} and X_c decrease considerably at elevated temperature (compared to room temperature). However, the irradiated composite material

experiences a very large decrease in X_c which is not reflected in a corresponding change in G_{nr}. Once again this difference may be attributable to the difference in the T_g between the composite and neat resin as previously discussed.

6.3 *Effect of Irradiation on Chemical Structure*

The properties of the neat resin are clearly a function of the morphology of the epoxy. The matrix dependent properties of the composite are also dependent on the epoxy morphology, although there are also other factors which may be equally important (i.e. fiber/matrix interfacial properties). Epoxies form highly cross-linked rigid network structures and it is sometimes stated that they are actually single gigantic molecules. However, Lee and Neville [2] state that "...there is no real evidence for this..." and suggest that the actual structure consists of "relatively small macromolecules embedded in a surrounding matrix of lower molecular weight material".

Electron radiation is known to produce two effects on polymeric materials, crosslinking and chain scission (cleavage). Because the Fiberite 934 system has a relatively high crosslink density the primary mechanism is believed to be chain scission [3-4,7]. Evidence for this hypothesis is the lowering of the T_g following irradiation and the generation of low molecular weight products [4, Chapter 2]. Additionally, systems containing carbon-nitrogen bonds have been reported to be particularly susceptible to cleavage and the radiation resistance of epoxies cured with BF_3MEA has been found to be poorer than expected from the relatively high T_g's [2]. The Fiberite 934 system contains a number of C-N bonds and BF_3MEA, while not used as the primary curing agent, is also present.

The dramatic color change the neat resin experienced during irradiation (Chapter 4) is believed to be a result of formation of a color center, due to addition of a hydrogen atom to an amine group. This information, coupled with the vulnerability of the C-N to cleavage, leads to the conclusion that a number of these bonds may be broken during irradiation.

Reliable quantitative relationships between chemical structure and mechanical properties have not, to the best of the author's knowledge, been shown to exist. However, in view of the measured changes in the neat resin and composite properties, the work done by Reed, et al. [7] with a modified material system, and the postulated changes in the chemical structure of the epoxy, it is unlikely that the radiation resistance of the Fiberite 934 system can be improved without substantial modifications to the basic epoxy chemistry.

7.0 Conclusions

The effects of temperature and electron radiation on the compressive properties of T300/934 graphite/epoxy and on the tensile properties of the neat Fiberite 934 resin will be summarized below. The temperature range and total radiation dose were selected to simulate "worst-case" exposure to 30 years in the geosynchronous earth orbit (GEO) environment. Materials which actually experience long term exposure to the GEO environment may be affected to a greater or lesser degree.

- Temperature was found to significantly affect compressive properties of T300/934. Properties generally improved at cryogenic temperature (-250° F; -157° C) and degraded at elevated temperature (250° F; 121° C).
- Irradiation degraded properties at all three temperatures and this degradation was most severe at elevated temperature.
- The compressive strengths, X_c and Y_c, were the "best" indicators of temperature and radiation induced changes. Although the Poisson's ratios experienced very large changes, the data exhibited considerable scatter, is difficult to interpret, and may be test method dependent. The strength values, on the other hand, were consistent and followed clear trends.

- Compressive strength models were investigated. The shear crippling mechanism developed by Hahn and Williams [24] was found to be conceptually satisfying, in addition to producing predicted values which correlate well with experimental measurements.
- The radiation-induced increases in elastic and shear moduli of the neat Fiberite 934 resin are consistent with the similar, and previously unexplained, changes in the composite room temperature transverse and shear moduli.

7.1.1 Recommendations for Future Study

- The nonlinear behavior of the composite and neat resin be investigated and characterized as viscoelastic, plastic, or microdamage related
- The effect of temperature and irradiation on the fiber/matrix interfacial bond be investigated
- The Poisson response under compressive load be further studied, using a different test method, to clarify the findings of this study
- Radiation-induced changes in the chemical structure of the epoxy be investigated in detail
- The effect of electron radiation on T300 carbon fibers be determined
- Realistic laminate configurations be investigated to determine if characterization of unidirectional material allows accurate estimates of changes in laminate properties or whether, presently unknown, interactions occur at the ply level during radiation exposure

References

1. Tenney, D.R., Sykes, G.F., and Bowles, D.E., "Composite Materials for Space Structures", Proceedings of the Third European Symposium on Spacecraft Materials in Space Environment, Oct., 1985, pp. 9-21.

2. Lee, H. and Neville, K., *Handbook of Epoxy Resins*, McGraw-Hill, 1967.

3. Milkovich, S.M., Herakovich, C.T., and Sykes, G.F., *Space Radiation Effects on Graphite-Epoxy Composite Materials*, Interim Report 45, The NASA-Virginia Tech Composites Program, VPI-E-84-20, June, 1984.

4. Sykes, G.F., Milkovich, S.M., and Herakovich, C.T., "Simulated Space Radiation Effects on a Graphite Epoxy Composite", *Polymeric Materials Science and Engineering, Proceedings of the ACS Division of Polymeric Materials and Engineering*, Vol. 52, American Chemical Society, 1985, pp. 598-603.

5. Milkovich, S.M., Sykes, G.F., and Herakovich, C.T., "Fracture Surfaces of Irradiated Composites", ASTM Symposium on Fractography of Modern Engineering Materials, Nashville, Nov., 1985 (in press for ASTM STP).

6. Milkovich, S.M., Sykes, G.F., and Herakovich, C.T., "Space Radiation Effects on the Thermo-Mechanical Behavior of Graphite-Epoxy Composites", *Journal of Composite Materials*, Vol. 20, No. 6, Nov. 1986, pp. 579-593.

7. Reed, S.M., Herakovich, C.T., and Sykes, G.F., *The Effects of Space Radiation on a Chemically Modified Graphite-Epoxy Composite Material*, Interim Report 60, The NASA-Virginia Tech Composites Program, VPI-E-86-19, October, 1986.

8. Reed, S.M., Sykes, G.F., and Herakovich, C.T., "Influence of Electron Radiation and Temperature on the Cyclic Matrix Dominated Response of Graphite-Epoxy" to appear in the *Journal of Reinforced Plastics and Composites*.

9. Bowles, D.E., Tompkins, S.S., and Sykes, G.F., "Electron Radiation Effects on the Thermal Expansion of Graphite/Resin Composites", *AIAA Paper no. AIAA-84-1704*, AIAA 19th Thermophysics Conference, Snowmass, CO, June 25-28, 1984.

10. Sykes, G.F. and Bowles, D.E., "Space Radiation Effects on the Dimensional Stability of a Toughened Epoxy Graphite Composite", *SAMPE Quarterly*, vol. 17, no. 4, July, 1986, pp. 39-45.

11. Tompkins, S.S., Sykes, G.F., and Bowles, D.E., "The Thermal and Mechanical Stability of Composite Materials for Space Structures", *IEEE/ASM/ASME/SME Space Tech Conference*, Anaheim, CA, Sept 23-25, 1985.

12. Sykes, G.F. and Slemp W.S., "Space Radiation Effects on an Elastomer Toughened Epoxy-Graphite Composite", *30th SAMPE National Symposium/Exhibition*, Anaheim, CA, March 19-21, 1985.

13. Funk, J.G. and Sykes, G.F., "The Effects of Radiation on the Interlaminar Fracture Toughness of a Graphite/Epoxy Composite", *Journal of Composites Technology and Research*, vol. 8, no. 3, Fall, 1986, pp. 92-97.

14. Takeda, N., Kawanishi, S., Udagawa, A., and Hagiwara, M., "Electron Irradiation Effects on Interlaminar Shear Strength of Glass or Carbon Cloth Reinforced Epoxy Laminates", *Journal of Materials Science*, no. 20, 1985, pp. 3003-3010.

15. Leung, C.L., "Space Environmental Effects on Graphite/Epoxy Composites", *Composites for Extreme Enviroments*, ASTM STP 768, N.R. Adsit, Ed., American Society for Testing and Materials, 1982, pp. 110-117.

16. Maiden, J., Gounder, R., and Seehra, S., "Development of Design Data on an Ultra-High Modulus Graphite/Epoxy Composite for Space Applications", *30th National SAMPE Symposium*, March 19-21, 1985.

17. D3171-76, "Fiber Content of Resin-Matrix Composites by Matrix Digestion", *1982 Annual Book of ASTM Standards*, American Society for Testing and Materials, part 36, American Society for Testing and Materials, Philadelphia, PA.

18. D638-82a, "Standard Test Method for Tensile Properties of Plastics", *1984 Annual Book of ASTM Standards*, Section 8, Vol. 08.01, American Society for Testing and Materials, 1984, Philadelphia.

19. Haskins, J.F.,"Advanced Composite Design Data", *12th National SAMPE Technical Conference*, Seattle, WA, Oct 7-9, 1980.

20. Tsai, S.W., *Composites Design, 1986*, Think Composites, Dayton, Paris & Tokyo, 1986.

21. D3410-75, "Standard Test for Compressive Properties of Unidirectional or Cross-ply Fiber-Resin Composites", *1984 Book of ASTM Standards*, Section 15, Volume 15.03 American Society for Testing and Materials, 1984, Philadelphia.

22. Sinclair J.H. and Chamis, C.C., "Compressive Behaviour of Unidirectional Fibrous Composites", *Compression Testing of Homogeneous Materials and Composites*, ASTM STP 808, Richard Chait and Ralph Papirno, Eds., American Society for Testing and Materials, 1983, pp. 155-174.

23. Clark, R.K. and Lisagor, W.B., *Effects of Method of Loading and Specimen Configuration on Compressive Strength of Graphite/Epoxy Composite Materials*, NASA TM-81796, April, 1980.

24. Hahn, H.T. and Williams, J.G., "Compression Failure Mechanisms in Unidirectional Composites", *Composite Materials: Testing and Design (Seventh Conference)*, ASTM

STP 893, J.M. Whitney, Ed., American Society for Testing and Materials, Philadelphia, 1986, pp. 115-139.

25. Ashton, J.E. and Whitney, J.M., *Theory of Laminated Plates*, Technomic Publishing Co., Inc. Stamford, CT, 1970.

26. Ashton, J.E. and Waddoups, M.E., "Analysis of Anisotropic Plates", *Journal of Composite Materials*, Vol. 3, Jan, 1969.

27. Ashton, J.E., "Analysis of Anisotropic Plates II", *Journal of Composite Materials*, Vol. 3, July, 1969.

28. Dally, J.W. and Riley, W.F., *Experimental Stress Analysis*, McGraw-Hill,1978.

29. Measurements Group, Inc., *Tech Note TN-509*, "Errors Due to Transverse Sensitivity in Strain Gages", 1982.

30. Pindera, M.-J., Gurdal, Z., Hidde, J.S., and Herakovich, C.T., *Mechanical and Thermal Characterization of Unidirectional Aramid/Epoxy*, CCMS-86-08, VPI-86-29, Virginia Tech, Blacksburg, VA, February, 1987.

31. Kumar, S., Adams, W.W., and Helminiak, T.E., "Uniaxial Compressive Strength of High Modulus Fibers for Composites", *Proceedings of the American Society for Composites (Dayton, OH)*, Technomic Publishing Co., Lancaster, PA, pp. 8-19.

32. Reiss, R., Yao, T.M., and Clark, R.K.,"Effect of Load Introduction in Compression Testing of Composite Laminates", *Compression Testing of Homogeneous and Composite Materials*, ASTM STP 808, Richard Chait and Ralph Papirno, Eds., American Society for Testing and Materials, 1893, pp. 200-220.

33. Collings, T.A., "Transverse Compressive Behaviour of Unidirectional Carbon Fibre Reinforced Plastics", *COMPOSITES*, May, 1974, pp 108-116.

34. Chiao, T.T., Cummins, A.D., and Moore, R.L., "Fabrication and Testing of Epoxide Resin Tensile Specimens", *COMPOSITES*, Jan/Feb, 1972, pp. 10-15.

35. Fanter, D.L.,"Method for Casting Epoxy Tensile Coupons", *Review of Scientific Instrumentation*, 49(7), July, 1978, pp. 1005-1006.

36. Perry, C.C.,"The Resistance Strain Gage Revisited", *Proceedings of the Society for Experimental Mechanics*, Vol. XLI, Brookfield Center, CT 1984.

37. Snedecor, G.W. and Cochran, W.G., *Statistical Methods*, The Iowa State University Press, Ames, IA, 1967.

Appendix A. Compression Test Results

This Appendix presents the detailed results of the T30/934 compression tests . The stress-strain data is shown in Figure 41-Figure 46 and the Poisson response is shown in Figure 47-Figure 52. The plots contain data from five replicate tests with the following exceptions: the results for the 0° coupons of the irradiated material at cryogenic temperature (Figure 41b) include six tests and the Poisson response for the 0° coupons of the irradiated material at elevated temperature (Figure 43b) includes the results of three tests.

Following the plots are tabulations of the elastic (Table 10) and strength (Table 11) properties. The method used to analyze the compression data is outlined in Chapter 3 and the details are presented in Appendix C.

The test condition is designated by the following code,

XYII

X = [N — Baseline (non-irradiated) material
I — Irradiated (10,000 Mrads) material

Y = [C — Cryogenic (−250°F; −157°C) Temperature
R — Room Temperature
E — Elevated (250°F; 121°C) Temperature

II = [00 — 0° Fiber Orientation
90 — 90° Fiber Orientation

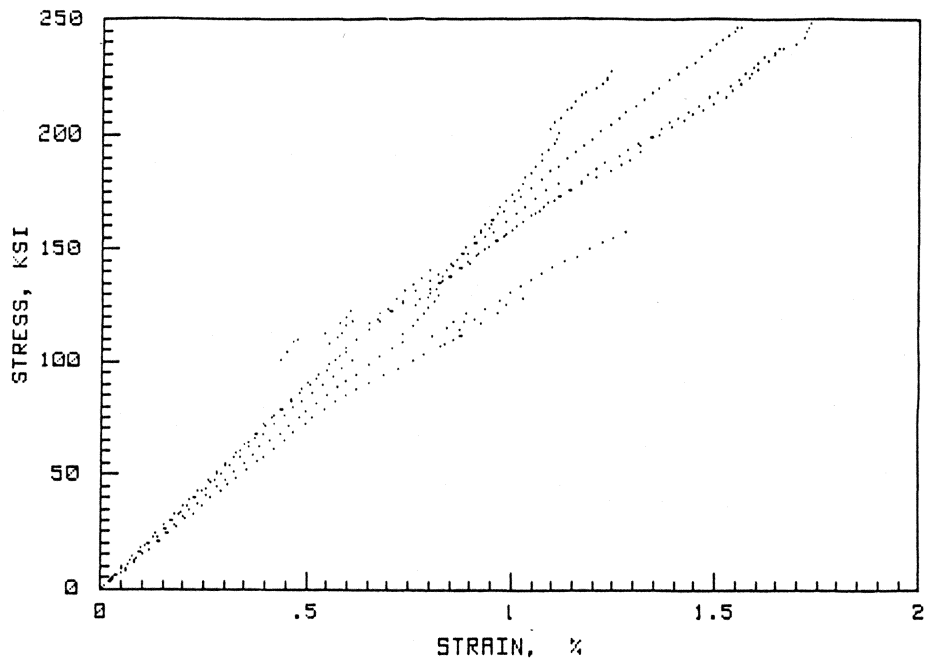

a) Baseline

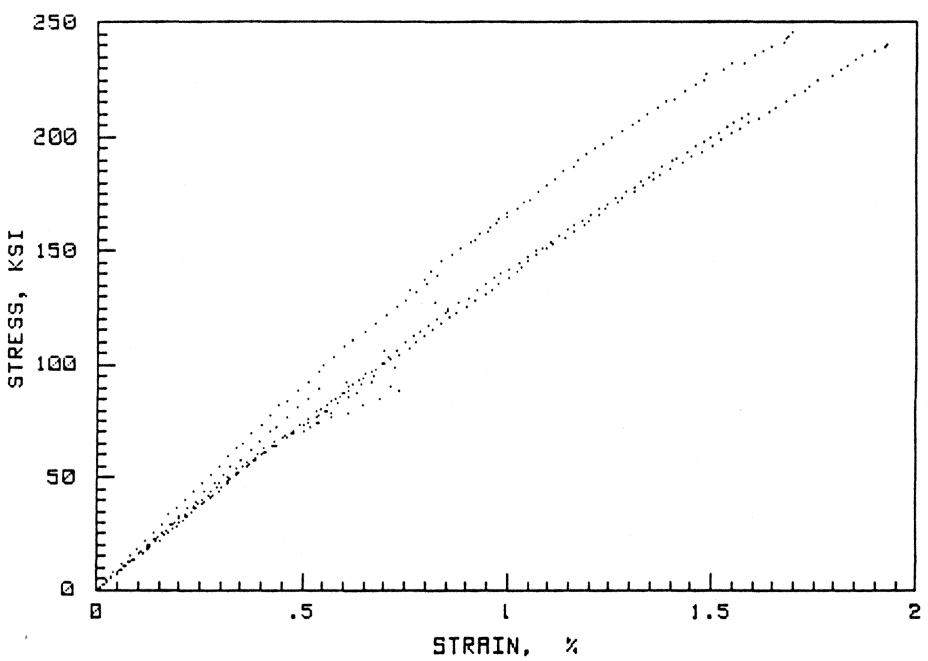

b) Irradiated

Figure 41. Compressive Stress-Strain Data for T300/934 0° Coupons at Cryogenic Temperature

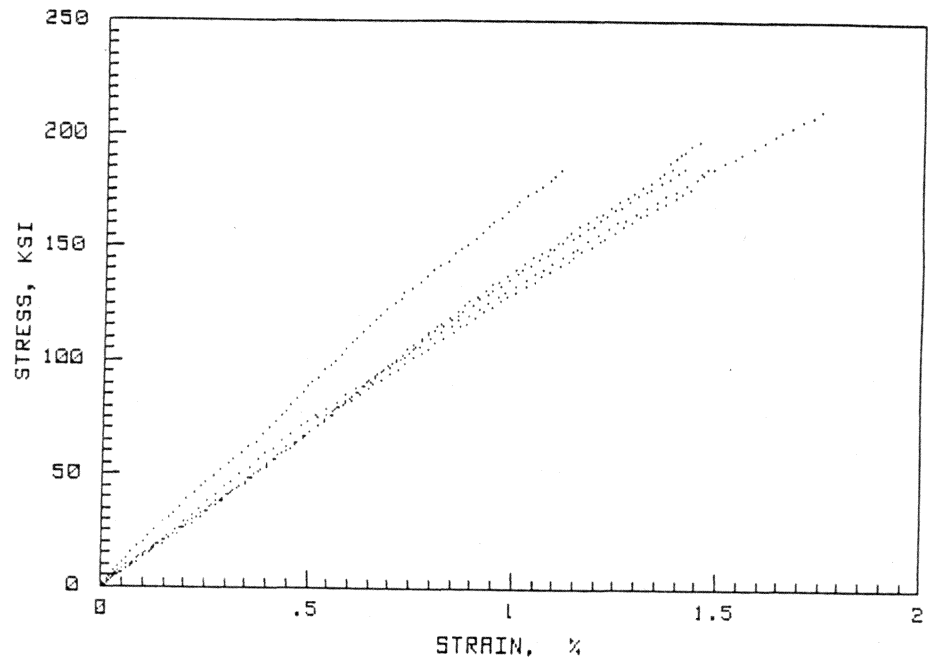

a) Baseline

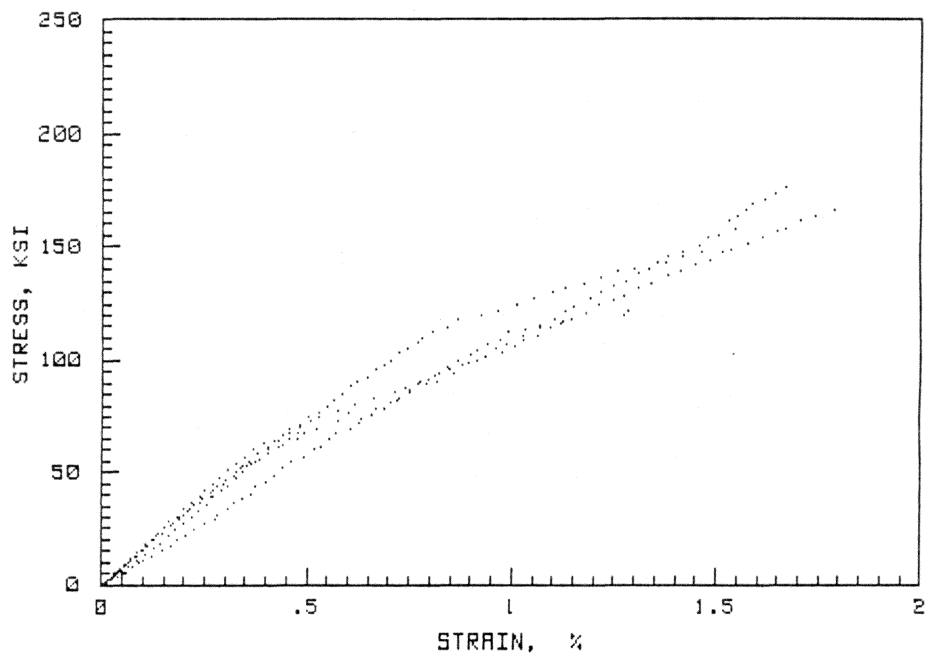

b) Irradiated

Figure 42. Compressive Stress-Strain Data for T300/934 0° Coupons at Room Temperature

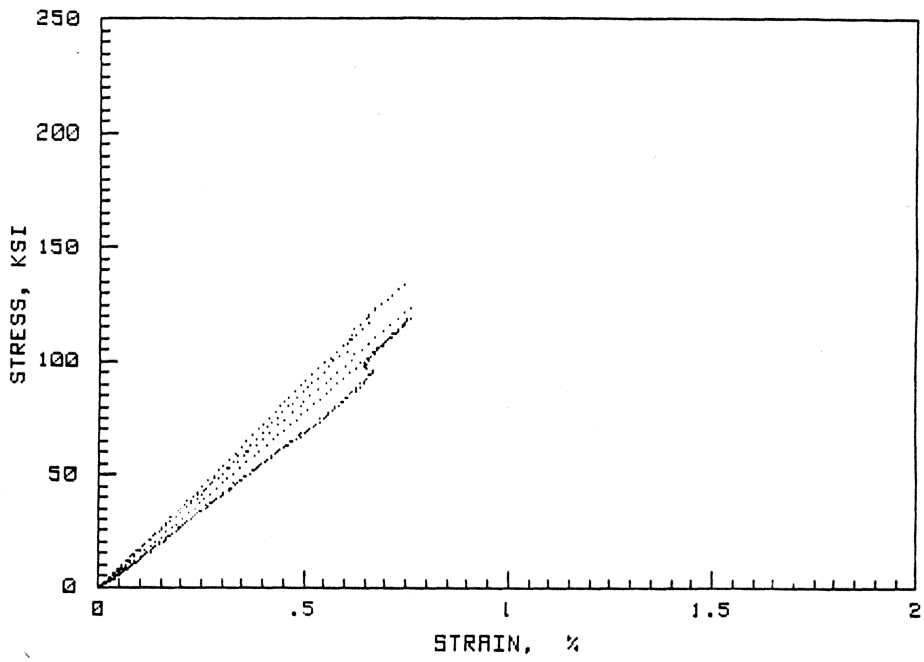

a) Baseline

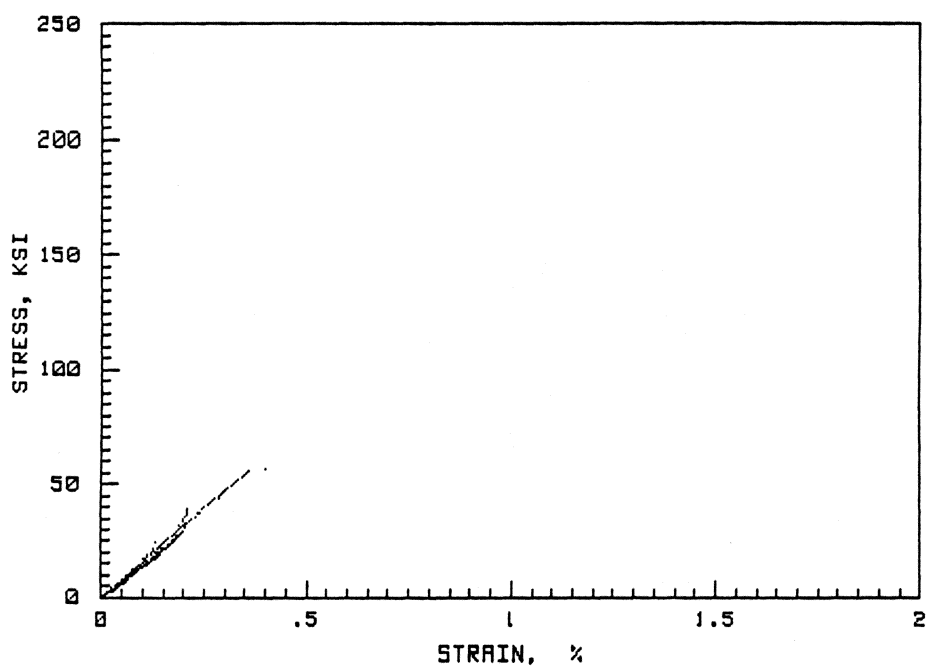

b) Irradiated

Figure 43. Compressive Stress-Strain Data for T300/934 0° Coupons at Elevated Temperature

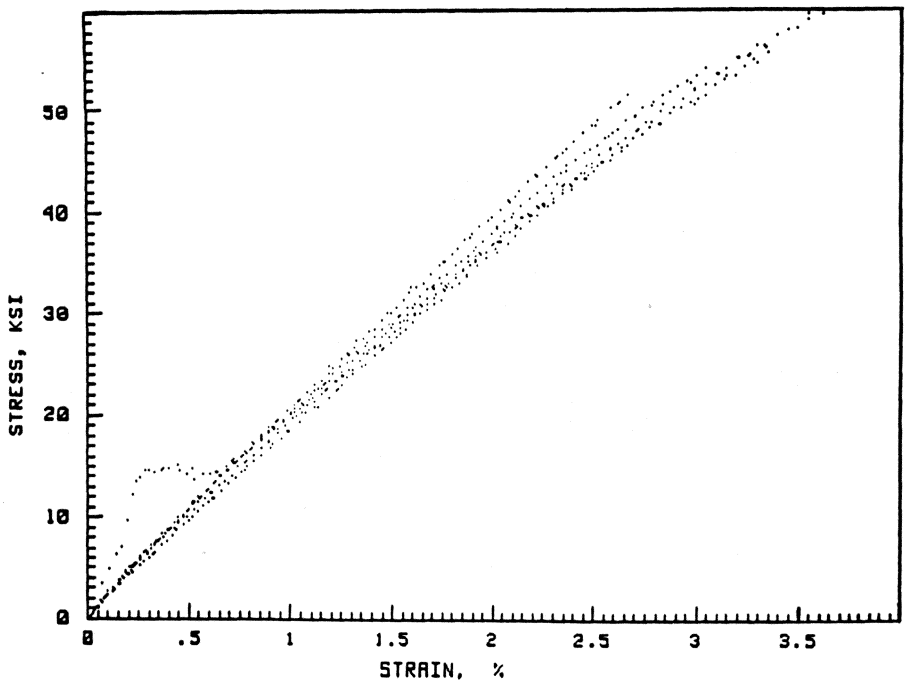

a) Baseline

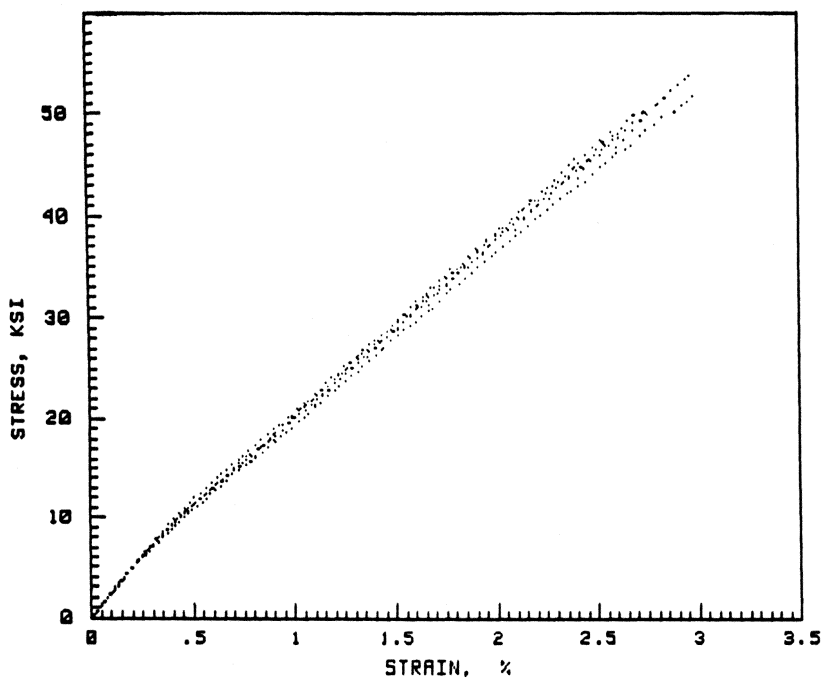

b) Irradiated

Figure 44. Compressive Stress-Strain Data for T300/934 90° Coupons at Cryogenic Temperature

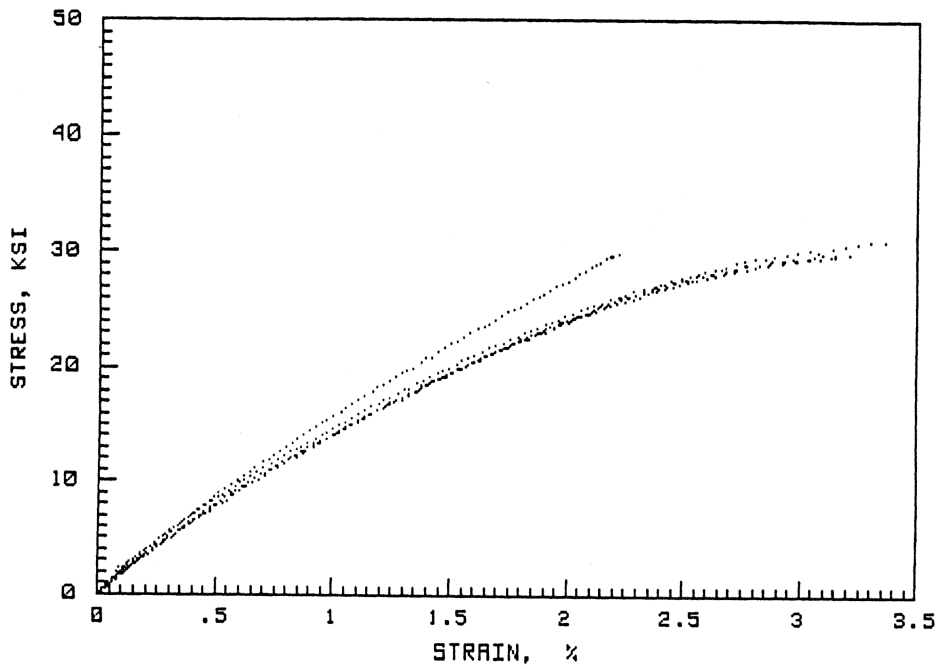

a) Baseline

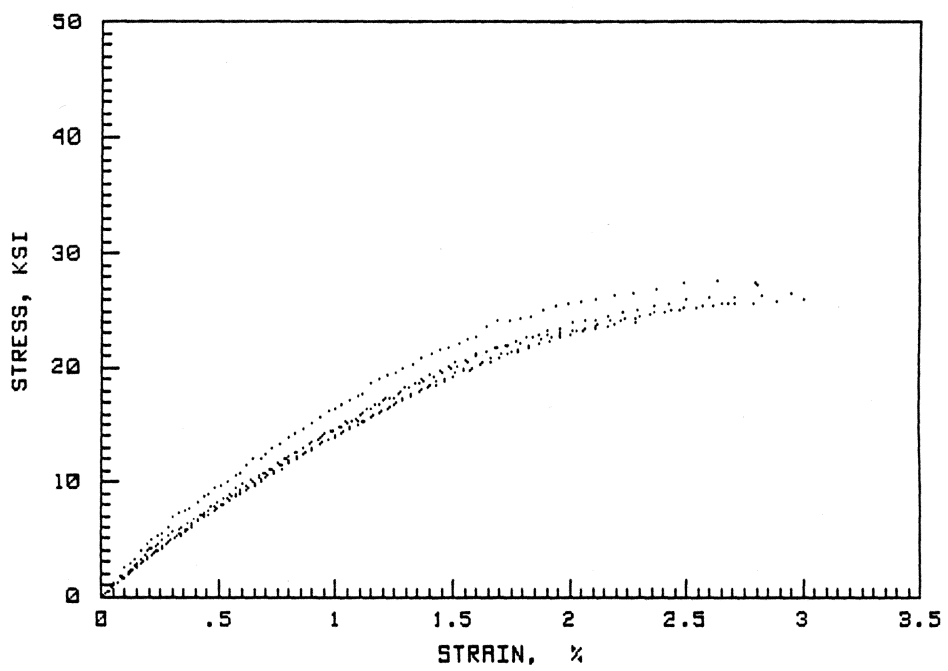

b) Irradiated

Figure 45. Compressive Stress-Strain Data for T300/934 90° Coupons at Room Temperature

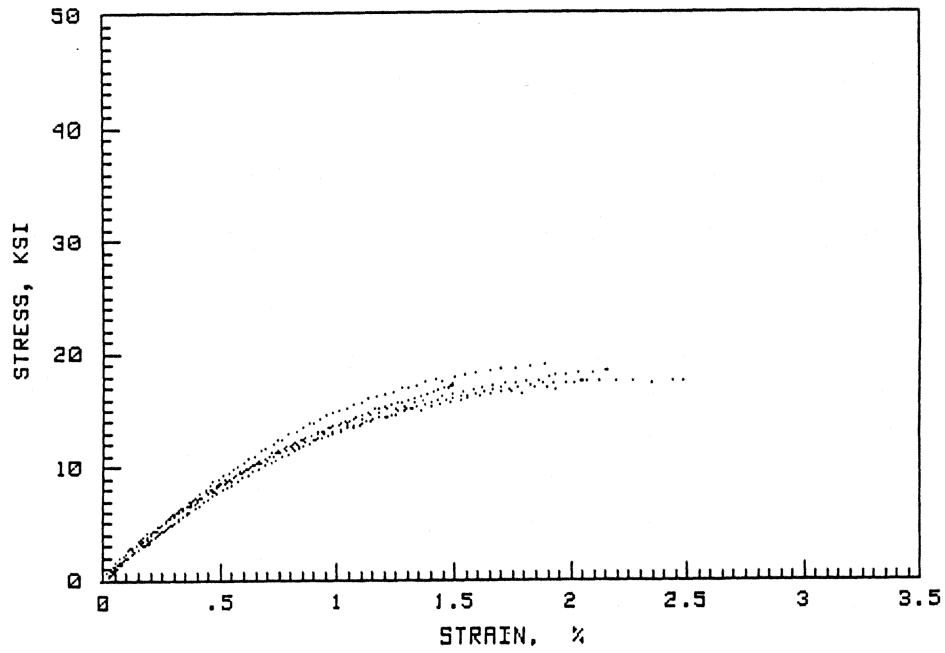

a) Baseline

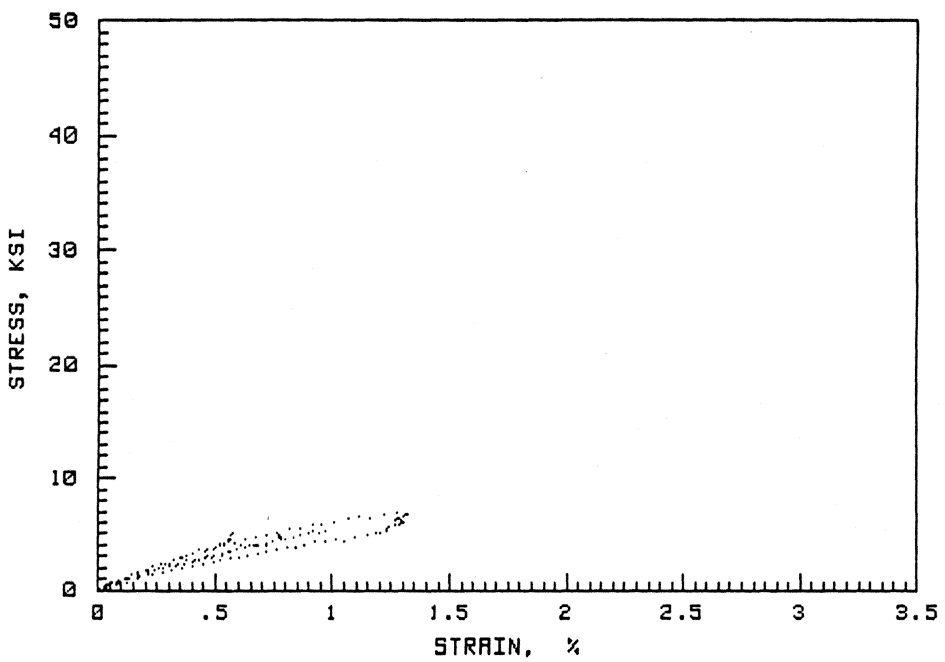

b) Irradiated

Figure 46. Compressive Stress-Strain Data for T300/934 90° Coupons at Elevated Temperature

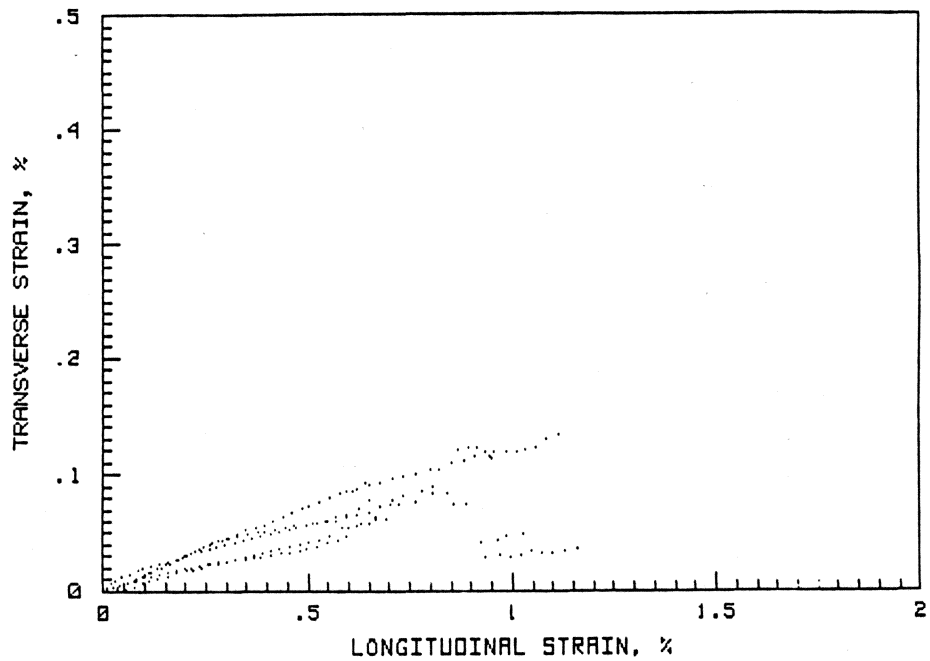

a) Baseline

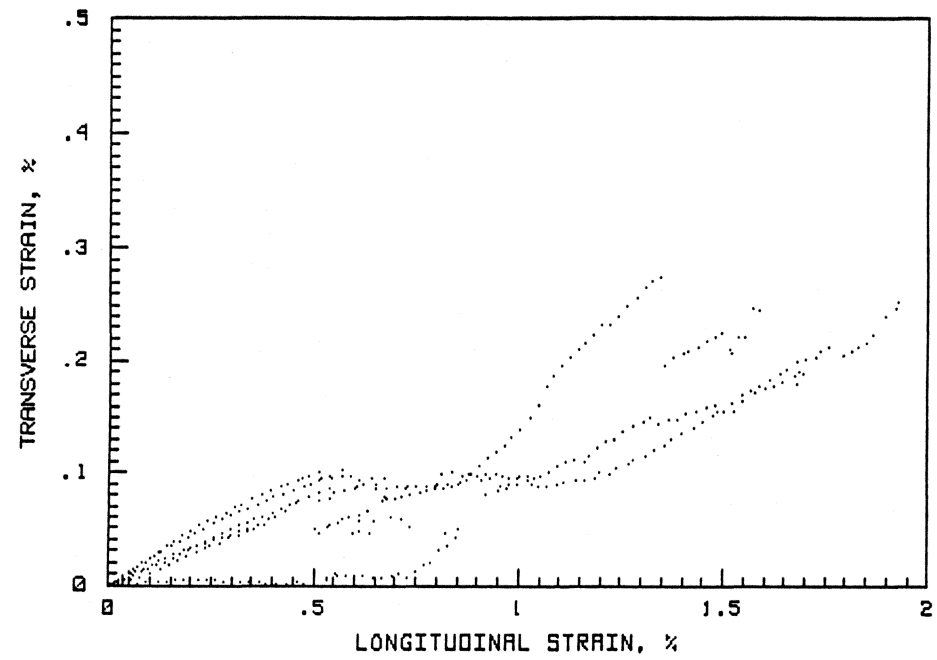

b) Irradiated

Figure 47. Compressive Poisson Response Data for T300/934 0° Coupons at Cryogenic Temperature

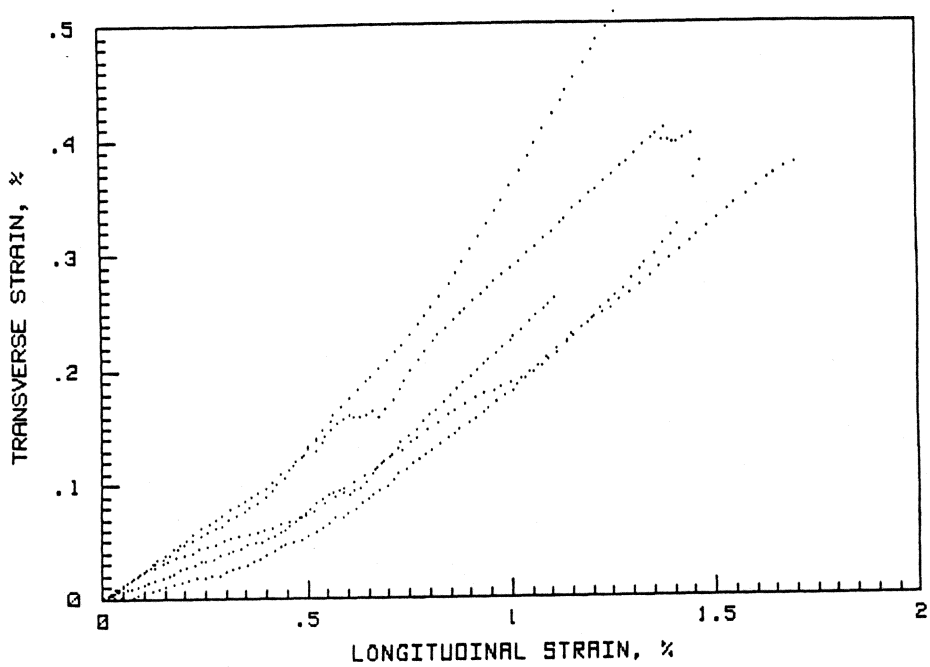

a) Baseline

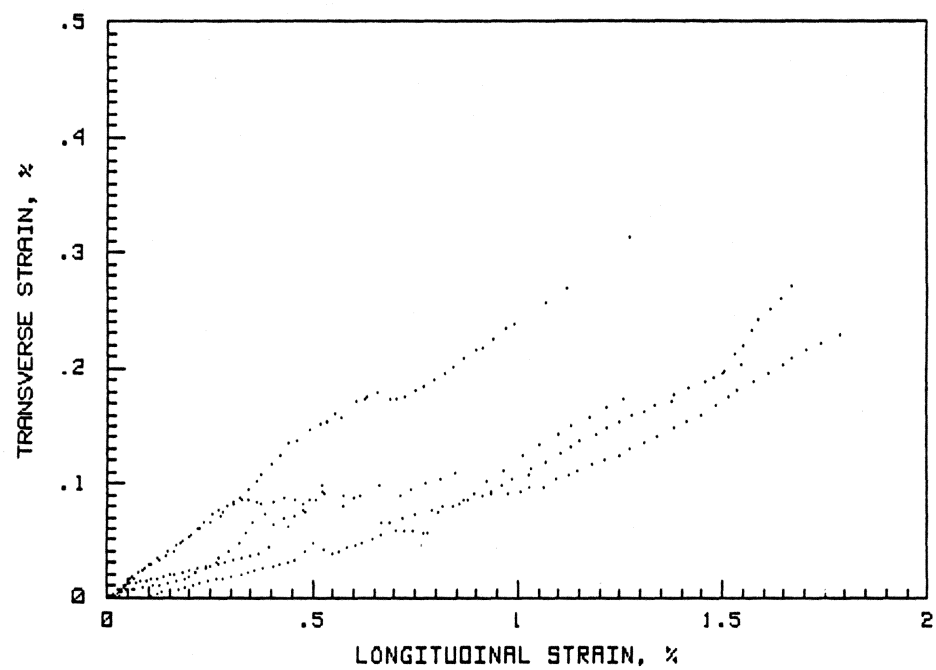

b) Irradiated

Figure 48. Compressive Poisson Response Data for T300/934 0° Coupons at Room Temperature

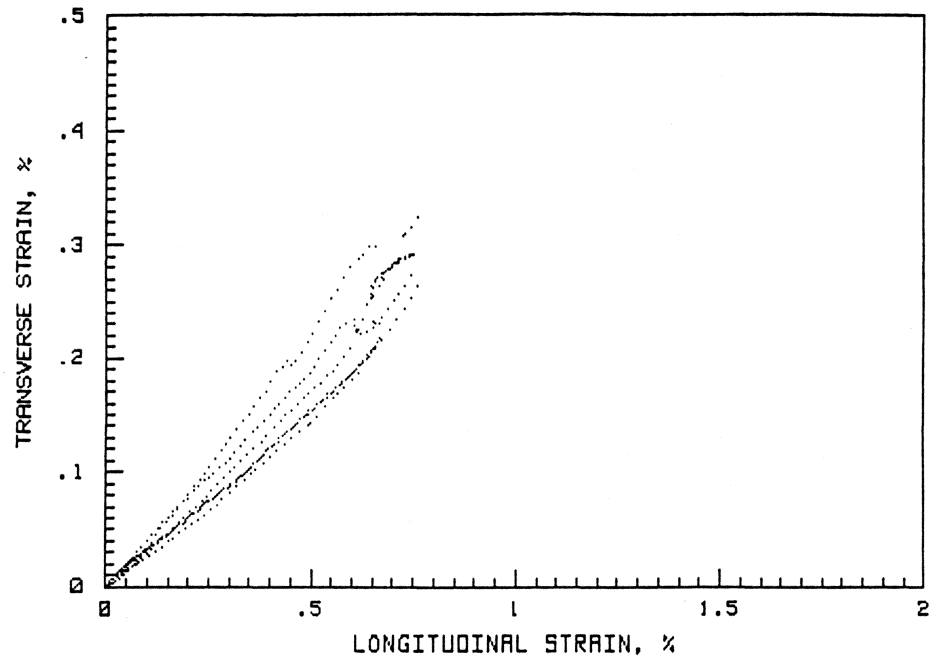

a) Baseline

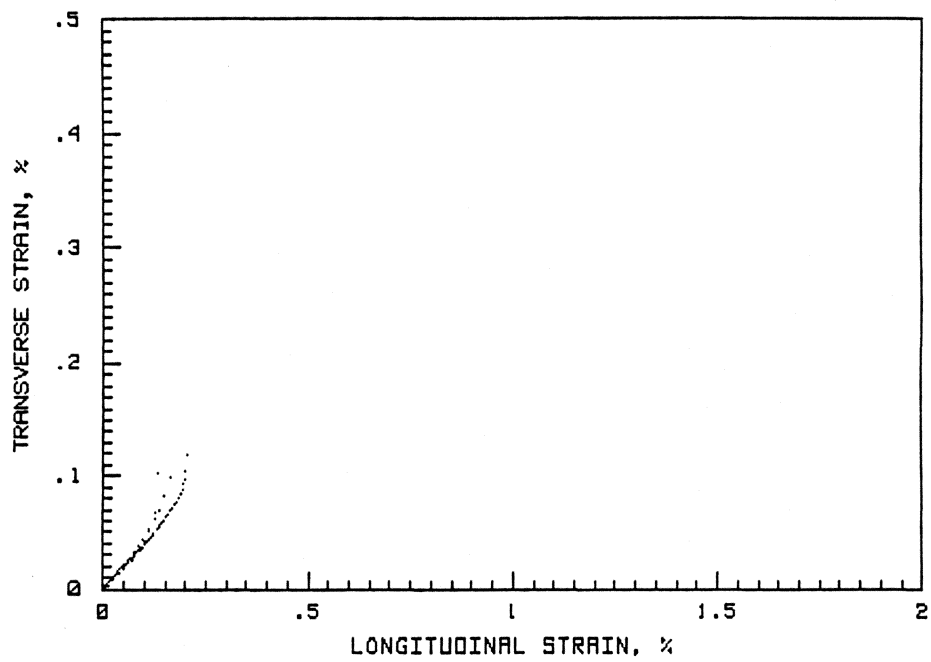

b) Irradiated

Figure 49. Compressive Poisson Response Data for T300/934 0° Coupons at Elevated Temperature

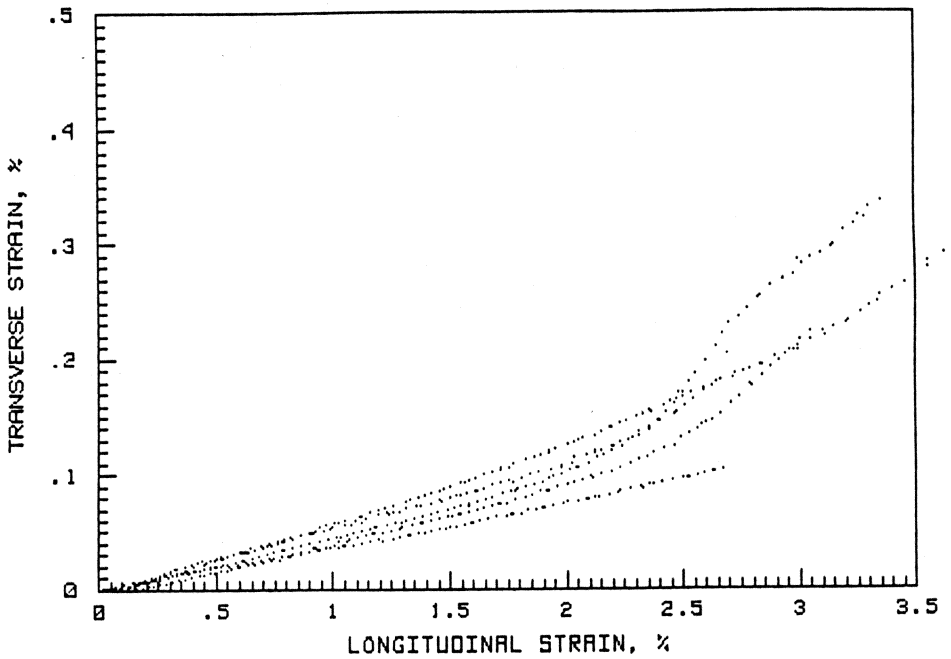

a) Baseline

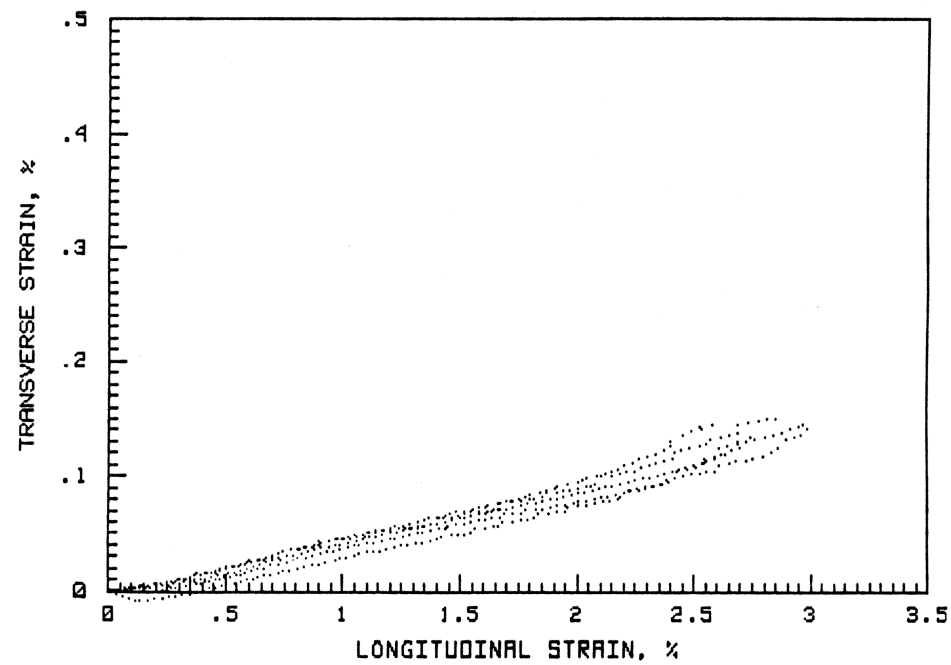

b) Irradiated

Figure 50. Compressive Poisson Response Data for T300/934 90° Coupons at Cryogenic Temperature

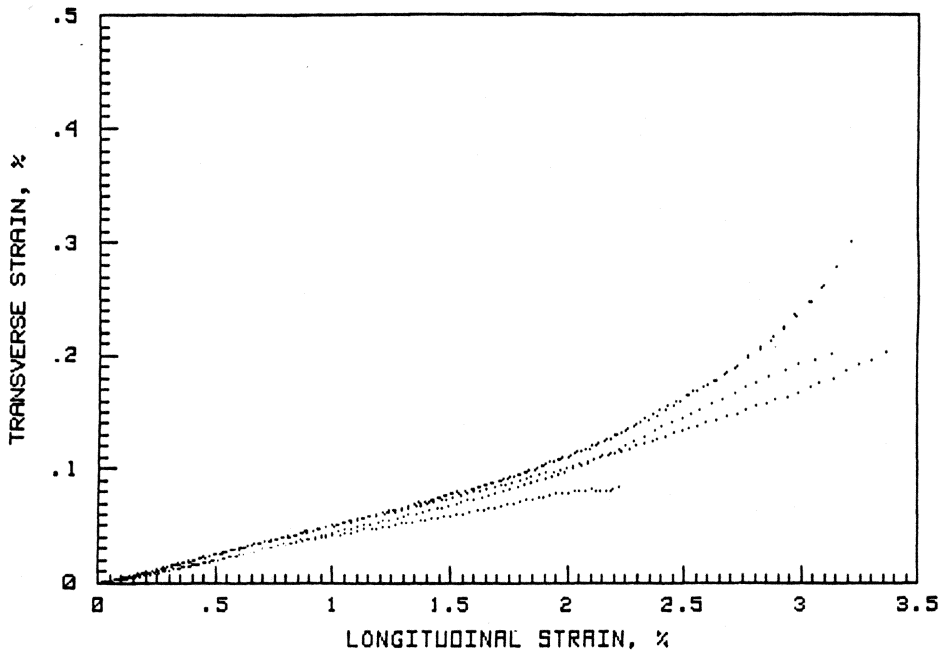

a) Baseline

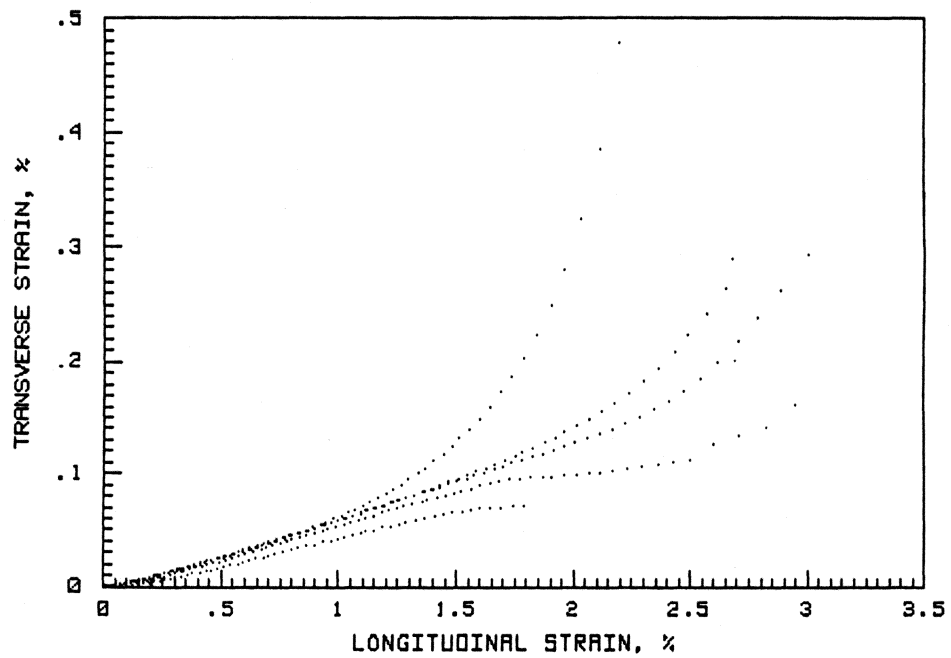

b) Irradiated

Figure 51. Compressive Poisson Response Data for T300/934 90° Coupons at Room Temperature

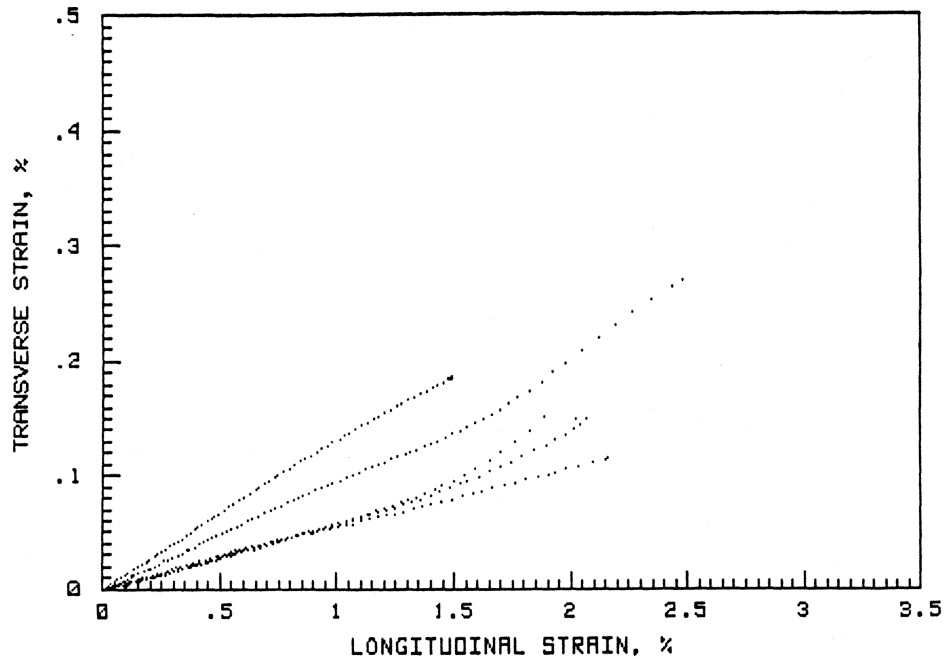

a) Baseline

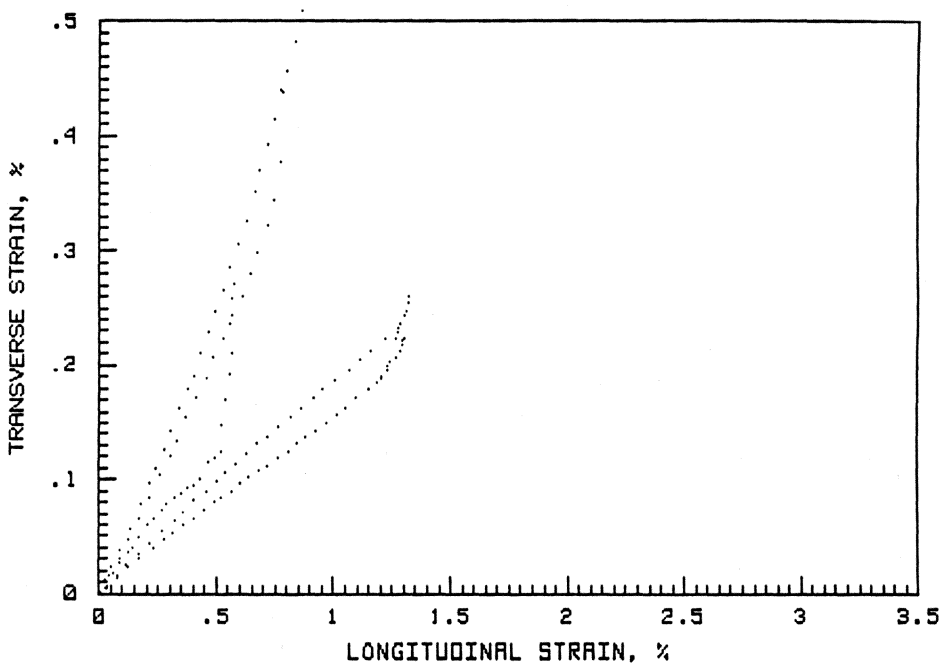

b) Irradiated

Figure 52. Compressive Poisson Response Data for T300/934 90° Coupons at Elevated Temperature

Table 10. Statistical Analysis for T300/934 Compressive Elastic Properties

YOUNG'S MODULUS

Test Condition	Mean Value	Standard Error	Range	
			High	Low
NC00	17.2	0.717	18.6	15.7
IC00	16.0	0.528	17.1	15.0
NR00	15.5	0.575	16.7	14.3
IR00	14.6	0.271	15.1	14.0
NE00	15.0	0.751	16.5	13.5
IE00	14.4	0.420	15.3	13.6
NC90	2.10	0.0529	2.21	2.00
IC90	2.14	0.0239	2.18	2.09
NR90	1.63	0.0270	1.69	1.58
IR90	1.74	0.0299	1.80	1.68
NE90	1.80	0.0304	1.86	1.73
IE90	0.666	0.0296	0.725	0.607

POISSON'S RATIO

NC00	0.136	0.0101	0.157	0.116
IC00	0.104	0.0169	0.138	0.0701
NR00	0.182	0.0361	0.255	0.110
IR00	0.153	0.0156	0.184	0.122
NE00	0.309	0.0232	0.356	0.263
IE00	0.384	0.0199	0.424	0.344
NC90	0.0320	0.0058	0.0436	0.0203
IC90	0.0324	0.0025	0.0374	0.0275
NR90	0.0366	0.0038	0.0442	0.0290
IR90	0.0447	0.0129	0.0705	0.0189
NE90	0.0791	0.0122	0.1035	0.0546
IE90	0.239	0.0545	0.348	0.130

Table 11. Statistical Analysis for T300/934 Compressive Strength Properties

COMPRESSIVE STRENGTH

Test Condition	Mean Value	Standard Error	Range	
			High	Low
NC00	241	9.26	260	222
IC00	228	18.4	265	192
NR00	193	13.2	219	166
IR00	188	15.0	218	158
NE00	126	6.16	139	114
IE00	48.3	6.09	60.5	36.1
NC90	56.4	3.10	62.7	50.3
IC90	51.8	2.11	56.0	47.5
NR90	30.4	0.530	31.5	29.3
IR90	26.3	1.36	29.0	23.5
NE90	18.9	0.688	20.3	17.6
IE90	8.71	0.674	10.1	7.36

FAILURE STRAIN

NC00	1.62	---	1.78	1.47
IC00	1.69	---	1.99	1.37
NR00	1.45	---	1.67	1.22
IR00	2.00	---	2.48	1.57
NE00	0.751	---	0.813	0.691
IE00	0.310	---	0.379	0.235
NC90	3.26	---	3.74	2.82
IC90	2.92	---	3.23	2.62
NR90	3.07	---	3.65	2.78
IR90	2.65	---	3.03+	1.97
NE90	1.94+	---	---	1.74
IE90	1.75	---	2.19	1.45

Appendix B. Neat Resin Test Results

This Appendix presents the detailed test data from the neat resin tensile tests. All the plots contain the results of three replicate tests. The stress-strain response is shown in Figure 53-Figure 56 and the Poisson response is shown in Figure 57-Figure 60.

Table 12 presents the elastic and strength properties for the individual tests. The system used to identify the individual specimens is similar to that used for the compression coupons. The first letter denotes the radiation dose; "N" denotes baseline (non-irradiated) and "I" denotes irradiated (10,000 Mrads). The second letter denotes the test temperature with "R" denoting room temperature and "E" denoting elevated (250° F; 121° C) temperature. The final two digits are related to the specimen fabrication sequence and allow specimens which were cured in the same batch to be identified.

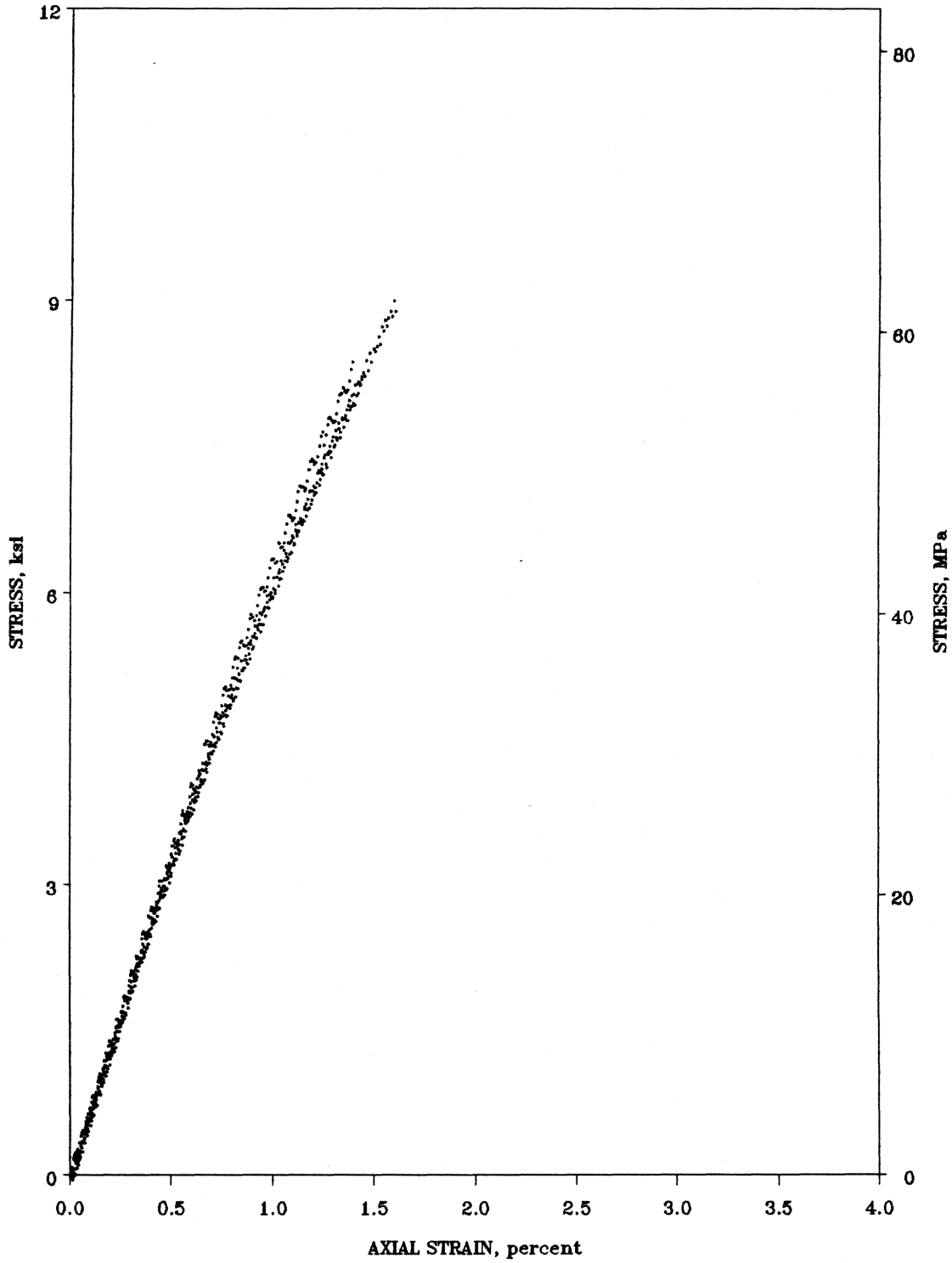

Figure 53. Tensile Stress-Strain Data for Fiberite 934 Specimens at Room Temperature (Baseline)

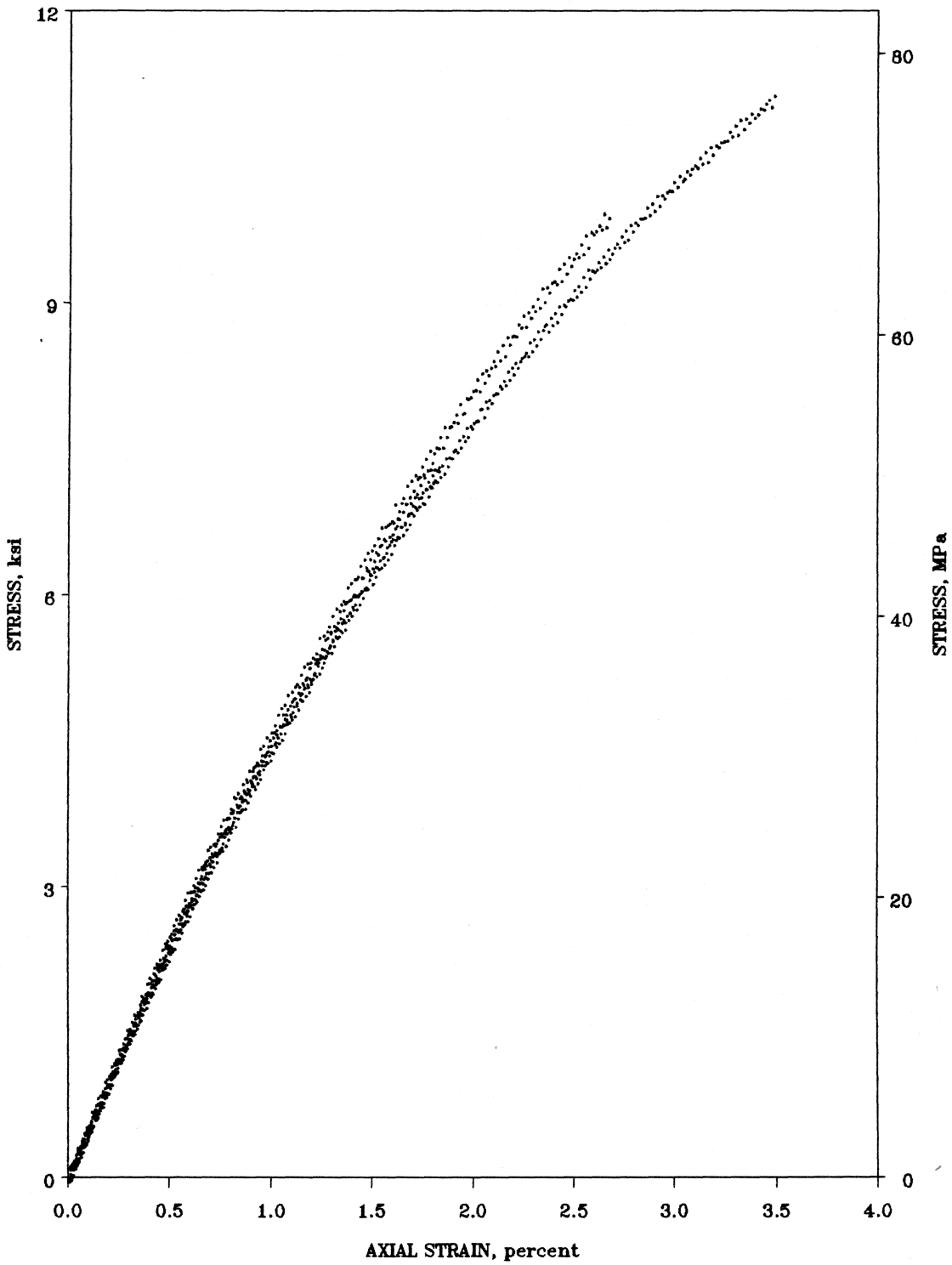

Figure 54. Tensile Stress-Strain Data for Fiberite 934 Specimens at Elevated Temperature (Baseline)

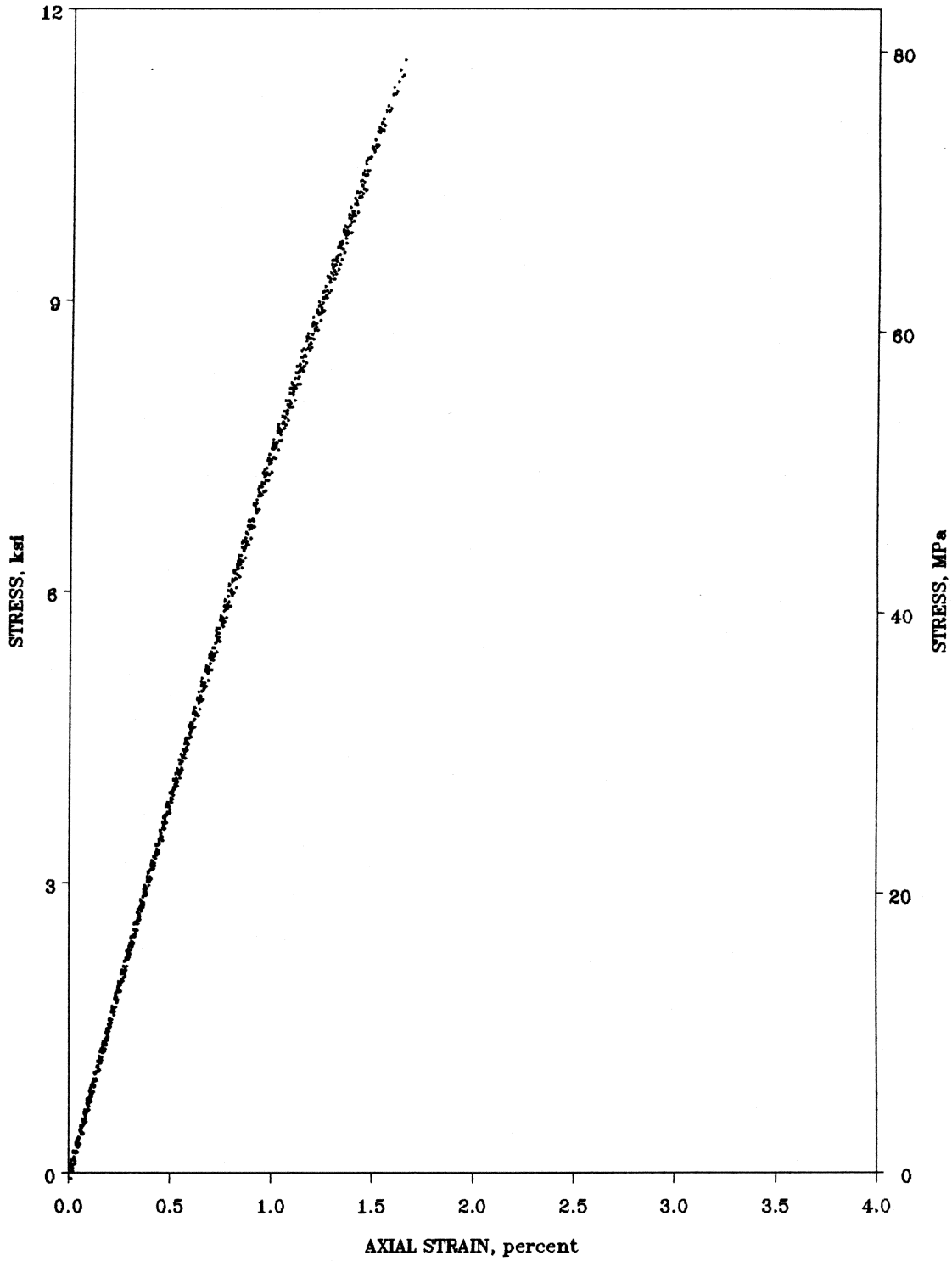

Figure 55. Tensile Stress-Strain Data for Fiberite 934 Specimens at Room Temperature (Irradiated)

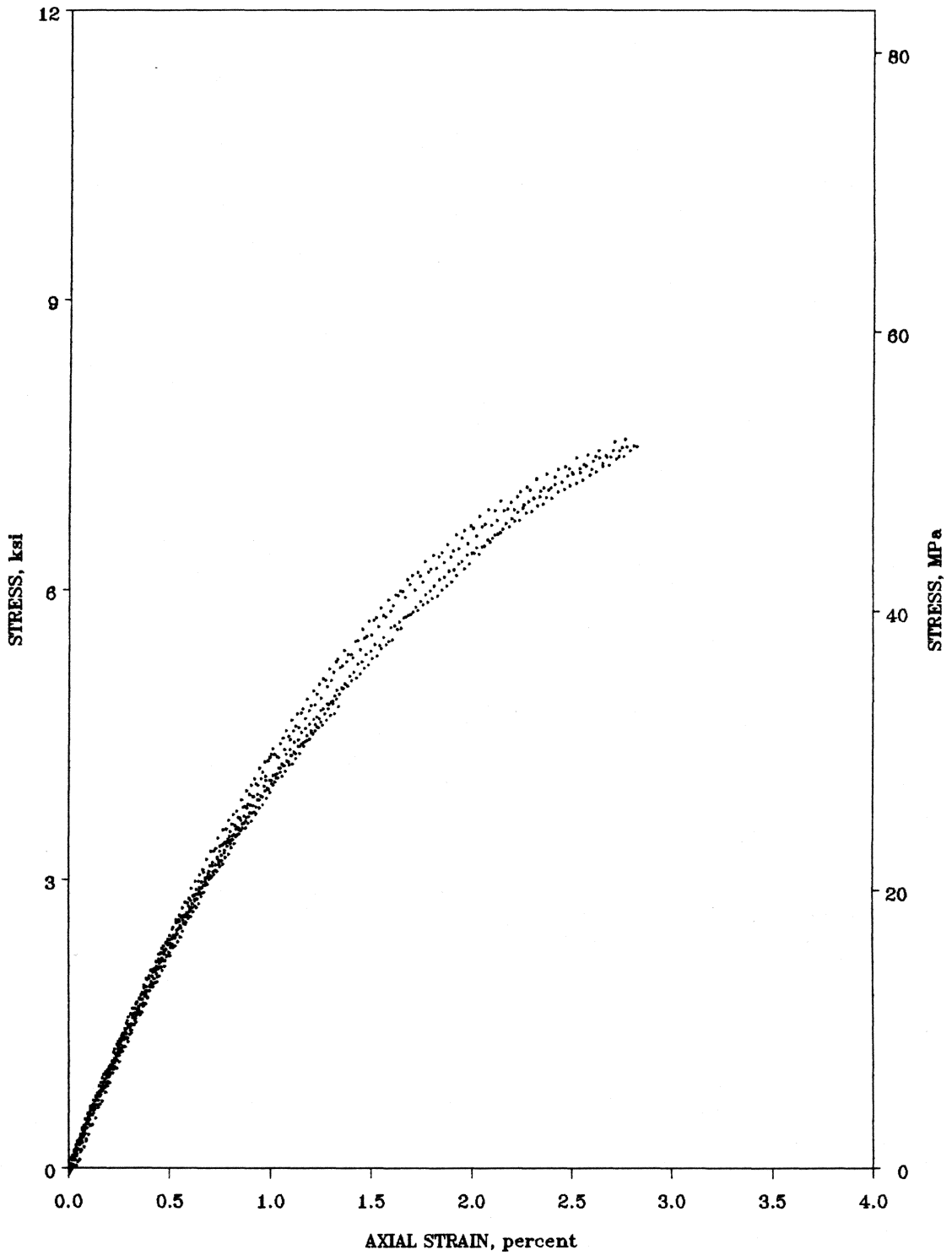

Figure 56. Tensile Stress-Strain Data for Fiberite 934 Specimens at Elevated Temperature (Irradiated)

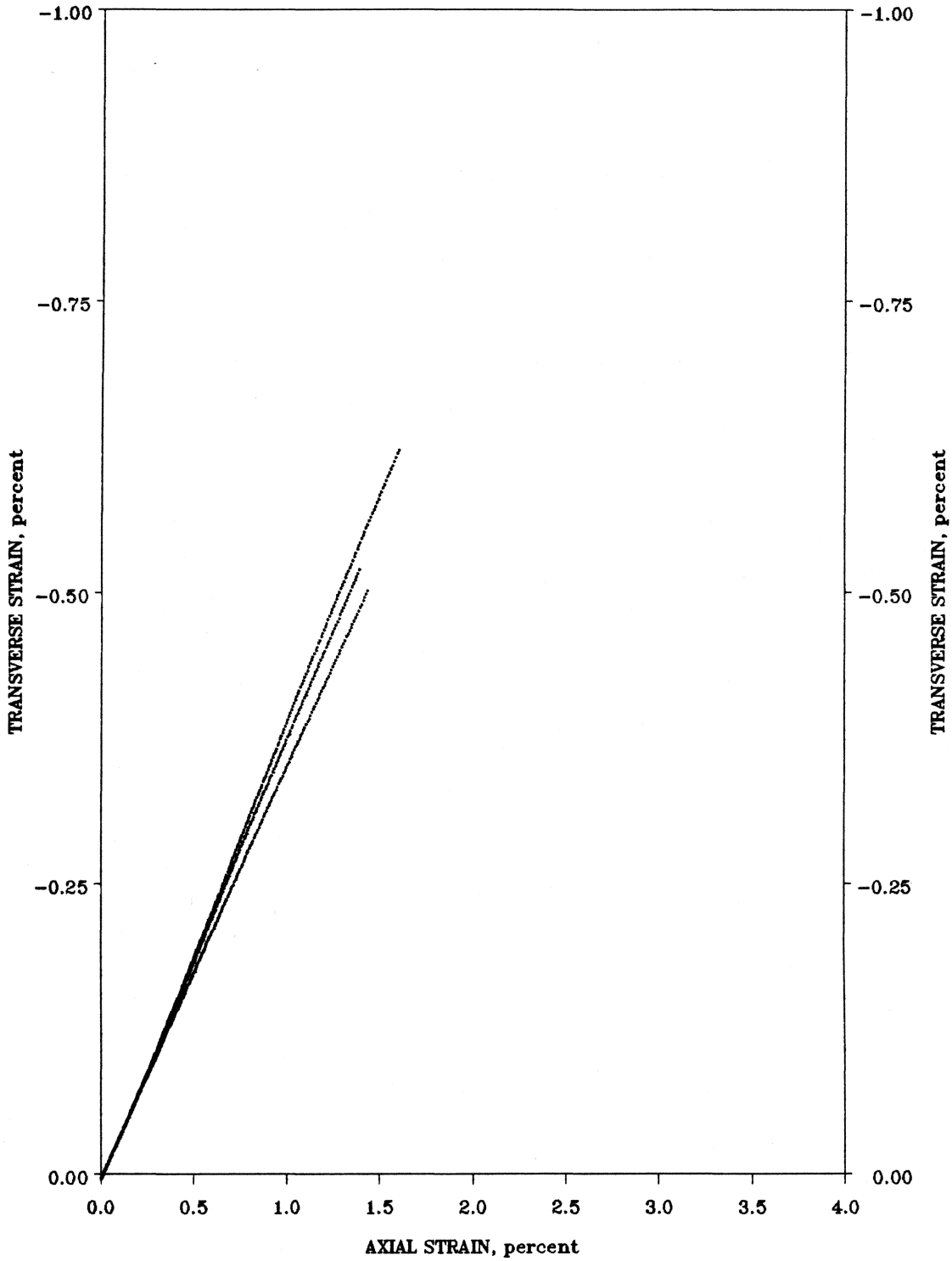

Figure 57. Fiberite 934 Neat Resin Poisson Response (Baseline, Room Temperature)

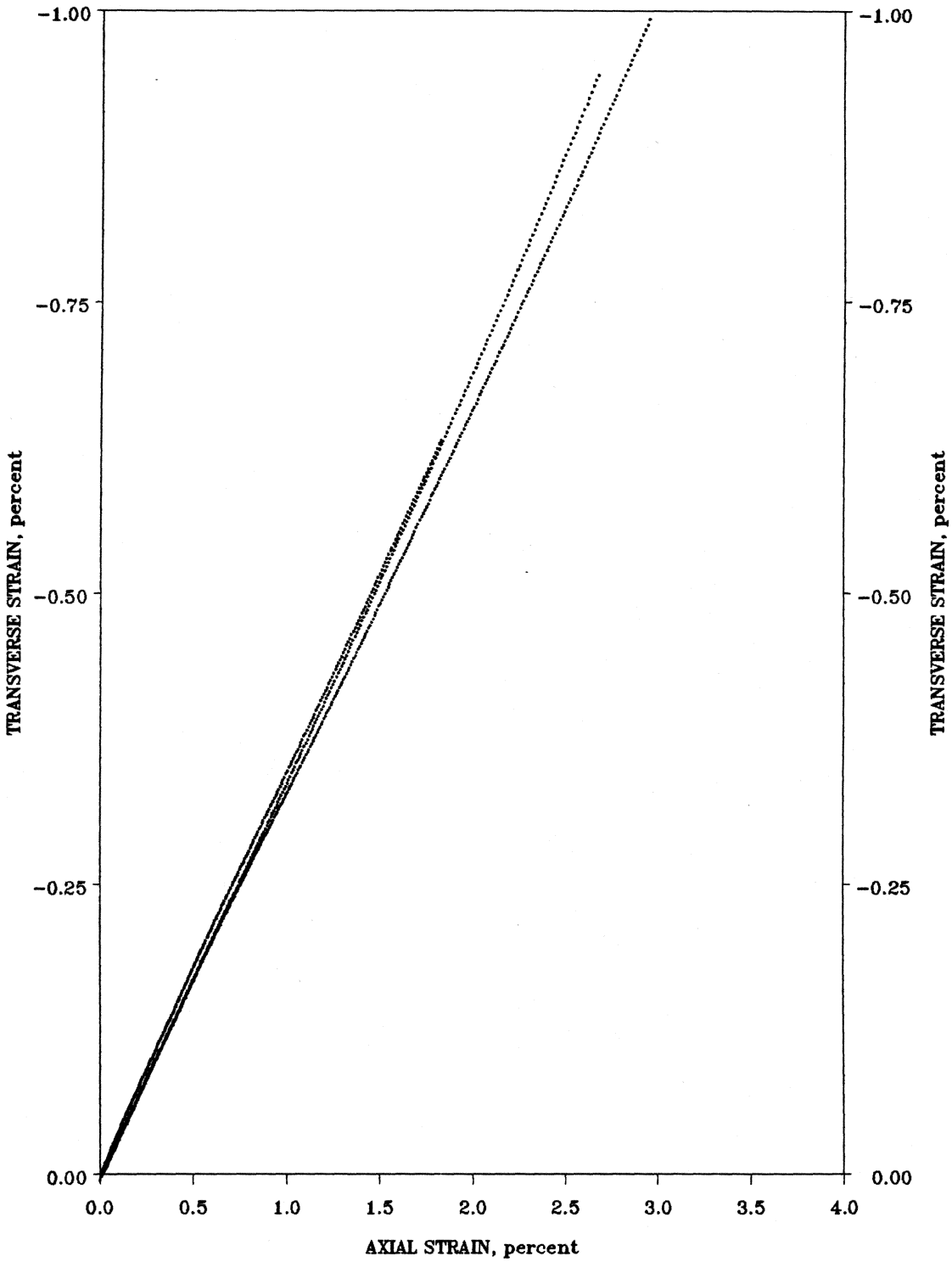

Figure 58. Fiberite 934 Neat Resin Poisson Response (Baseline, Elevated Temperature)

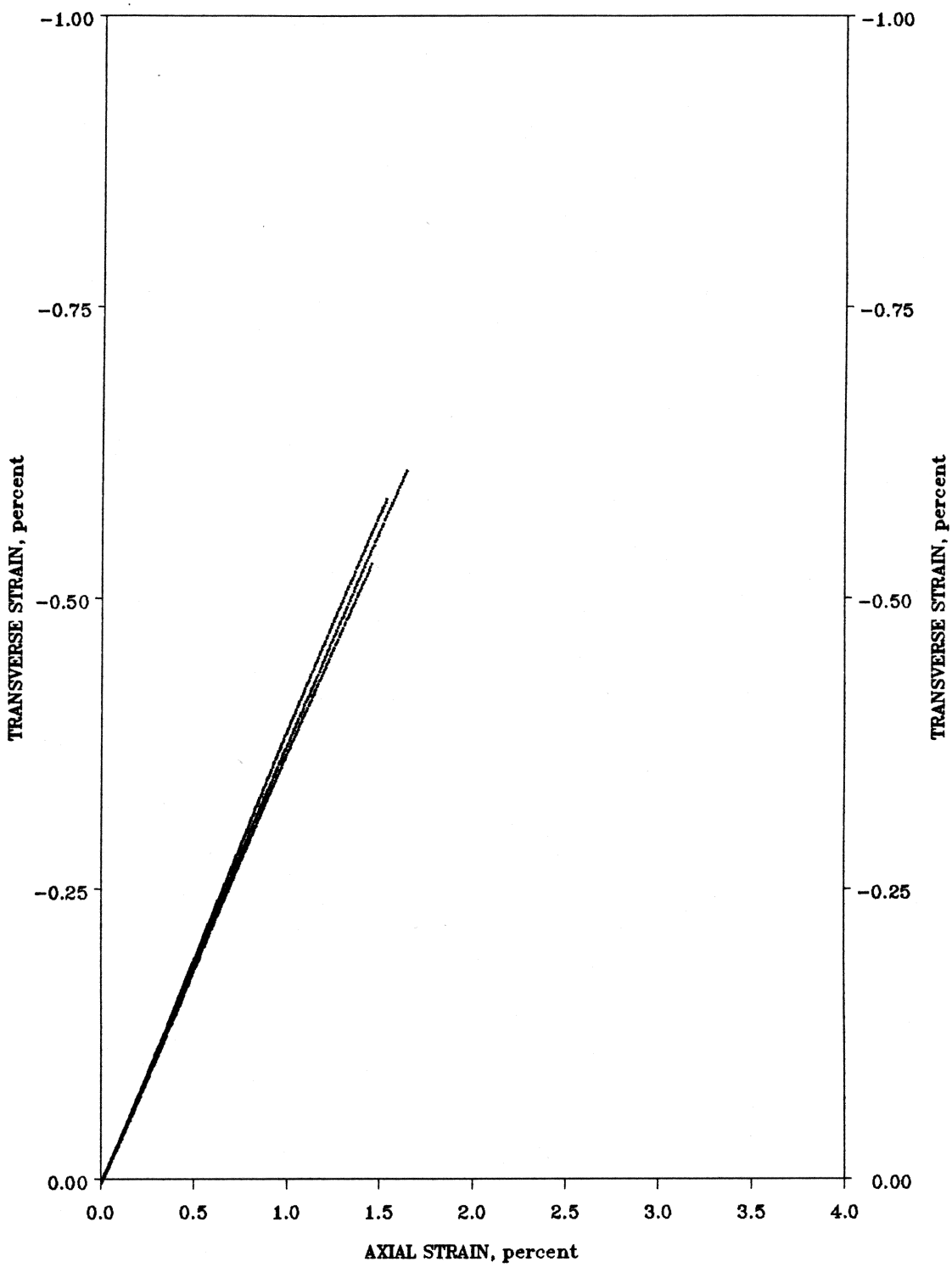

Figure 59. Fiberite 934 Neat Resin Poisson Response (Irradiated, Room Temperature)

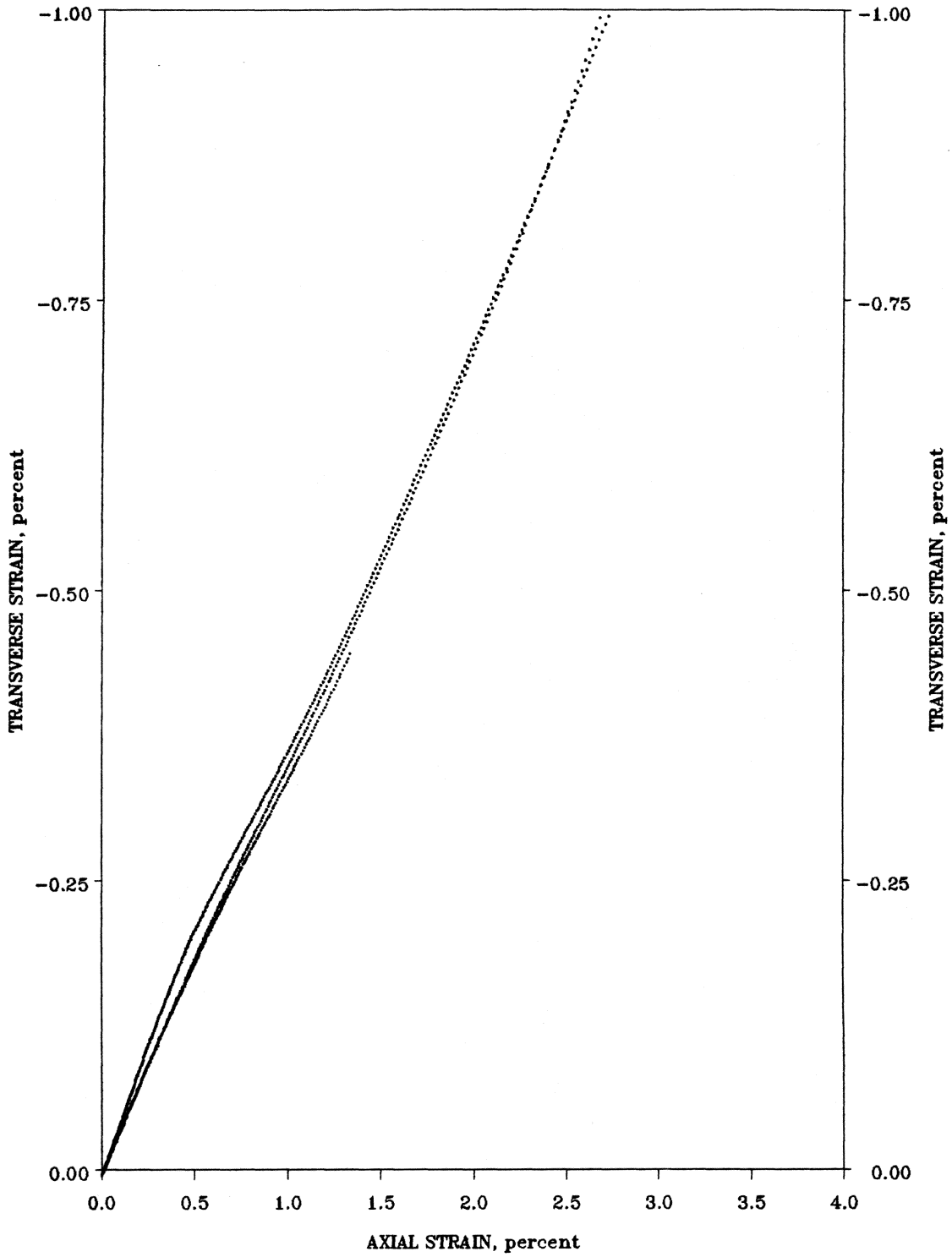

Figure 60. Fiberite 934 Neat Resin Poisson Response (Irradiated, Elevated Temperature)

Table 12. Detailed Fiberite 934 Neat Resin Tensile Test Results

Test	E (msi)	ν	σ_{max} (ksi)	ε_{max} (%)	G (msi)	σ_{PL} (ksi)
NR03	0.658	0.369	8.93	1.60	0.240	3.51
NR06	0.695	0.367	8.41	1.39	0.254	3.47
NR10	0.668	0.354	8.26	1.44	0.247	3.27
Mean	0.674	0.363	8.53	1.48	0.247	3.42
St. Dev.	0.019	0.008	0.35	0.11	0.007	0.13
CV	2.8%	2.2%	4.1%	7.4%	2.8%	3.8%
NE02	0.494	0.356	7.36	1.83	0.182	2.35
NE05	0.500	0.337	12.38	3.83	0.187	2.50
NE09	0.474	0.329	11.16	3.49	0.178	2.46
Mean	0.489	0.341	10.30	3.05	0.182	2.44
St. Dev.	0.014	0.014	2.62	1.07	0.005	0.08
CV	2.8%	4.1%	25%	35%	2.5%	3.2%
IR05	0.804	0.383	10.92	1.54	0.291	5.18
IR10	0.802	0.372	11.53	1.64	0.292	5.05
IR23	0.791	0.365	10.34	1.47	0.290	5.22
Mean	0.799	0.373	10.93	1.55	0.291	5.15
St. Dev.	0.007	0.009	0.56	0.085	0.001	0.089
CV	0.9%	2.4%	5.4%	5.5%	0.3%	1.7%
IE06	0.487	0.382	7.54	2.82	0.176	1.42
IE12	0.503	0.347	7.46	3.45	0.187	1.47
IE22	0.512	0.375	4.84	1.34	0.186	1.13
Mean	0.501	0.368	6.61	2.54	0.183	1.34
St. Dev.	0.013	0.019	1.54	1.08	0.006	0.18
CV	2.5%	5%	23%	43%	3.3%	14%

St. Dev.--Sample Standard Deviation
CV--------Coefficient of Variation--St. Dev/Mean

Appendix C. Data Analysis and Statistical Calculations

This Appendix contains the details of various calculations and derivations described in the text in a general way. More specifically, the first section covers the derivation of the correction for bending effects used in the analysis of the compression test data; the second section presents the least squares equations and describes how this criterion was applied to the analysis of the test data; and finally, the third section describes the methods used to estimate the standard errors presented in Appendix A and shown in Chapter 4.

C.1 Correction for Bending Effects

This section outlines the method used to correct the strain gage data to eliminate the influence of bending effects. The method uses the geometry and load conditions shown in Figure 61. The goal is to modify the strain data so it that it reflects only the the influence of the axial load, P. The following assumptions are used:

- The strain distribution is continuous and linear through the thickness
- The neutral axis is located at the geometric center of the cross-section
- The strain gage grids are flat and separated by a uniform layer of backing material and adhesive

Two different gage stacking sequences are considered; the orientations of the gages is with reference to the load direction. The numerical subscripts (i.e. 1,2,3,4) on the strains denote the gage number (Figure 61), the subscript "a" denotes "axial" and the "t" subscript denotes "transverse".

C.1.1 For Case 1:

If "c" denotes the distance from the center of the specimen to the first active grid and "b" denotes the thickness of the gage backing and an adhesive layer, then the strain in the four gages are:

$$\varepsilon_1 = \frac{P}{AE} + \frac{Mc}{IE}$$

$$\varepsilon_2 = -\nu\left[\frac{P}{AE} + \frac{M(c+b)}{IE}\right]$$

$$\varepsilon_3 = \frac{1-\nu}{2}\left[\frac{P}{AE} + \frac{M(c+2b)}{IE}\right]$$

$$\varepsilon_4 = \frac{P}{AE} - \frac{Mc}{IE}$$

The axial strain, P/AE, is then:

$$\varepsilon_a = \frac{P}{AE} = \frac{\varepsilon_1 + \varepsilon_4}{2}$$

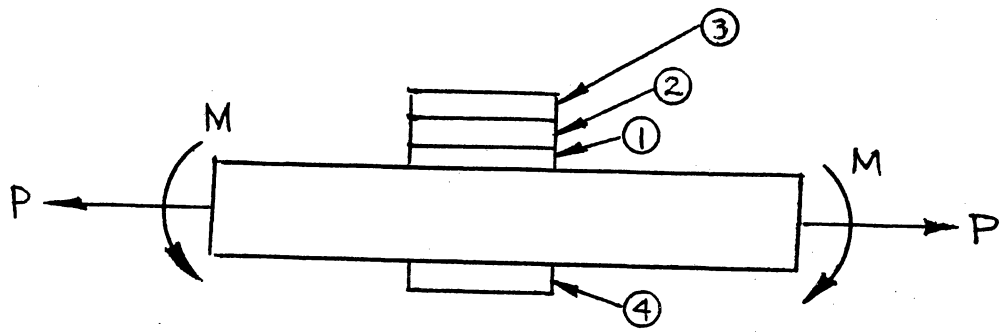

Gage Number	Orientation	
	Case 1	Case 2
1	0°	90°
2	90°	0°
3	45°	45°
4	0°	0°

Figure 61. Strain Gage Stacking Sequences

Using the fact that $\nu = -\frac{\varepsilon_T}{\varepsilon_a}$, the equation for ε_2 can be rewritten,

$$\varepsilon_2 = \varepsilon_T + \frac{\varepsilon_T}{\varepsilon_a}\left(\frac{M(c + b)}{IE}\right)$$

The bending strain coefficient, $\frac{M}{IE}$, is:

$$\frac{M}{IE} = \frac{\varepsilon_1 - \varepsilon_4}{2c}$$

Finally, substituting the expressions for $\frac{M}{IE}$ and ε_a into the equation for ε_2 and solving for ε_T,

$$\varepsilon_T = \frac{\varepsilon_2}{1 + \left[\frac{\varepsilon_1 - \varepsilon_4}{\varepsilon_1 + \varepsilon_4}\right]\left[\frac{c + b}{c}\right]}$$

C.1.2 For Case 2:

Performing a similar analysis for the second stacking sequence,

$$\varepsilon_1 = -\nu\left[\frac{P}{AE} + \frac{Mc}{IE}\right]$$

$$\varepsilon_2 = \frac{P}{AE} + M\frac{(c + b)}{IE}$$

$$\varepsilon_3 = \frac{1 - \nu}{2}\left[\frac{P}{AE} + M\frac{(c + 2b)}{IE}\right]$$

$$\varepsilon_4 = \frac{P}{AE} - \frac{Mc}{IE}$$

The bending strain coefficient is,

$$\frac{M}{IE} = \frac{\varepsilon_2 - \varepsilon_4}{2c + b}$$

The axial strain is,

$$\varepsilon_a = \frac{\varepsilon_2 + \varepsilon_4}{2} - \frac{b}{2}\left[\frac{\varepsilon_2 - \varepsilon_4}{2c + b}\right]$$

The transverse strain is:

$$\varepsilon_T = \frac{\varepsilon_1}{1 + \left[\frac{\varepsilon_2 - \varepsilon_4}{\varepsilon_a}\right]\left[\frac{c}{2c + b}\right]}$$

It should be noted that typical values for the thickness of the gage backing and adhesive layer can be obtained from Micro-Measurements technical literature [39].

C.2 Regression Equations

Probably the most common method used to determine the "best" curve through a set of data is the method of least squares. In essence the least squares criterion asserts that the optimal curve is obtained if the square of the deviations of the data points from it is minimized. Imagine a set of n matched pairs (x,y) of observations. The least squares criterion states that the best $y = f(x)$ curve is obtained for the minimum of,

$$E = \sum_{i=1}^{n} [y_i - f(x_i)]^2$$

In this study f(x) was chosen to be quadratic,

$$E = \sum_{i=1}^{n} [y_i - (A + Bx_i + Cx_i^2)]^2$$

The minimum is obtained by differentiating with respect to each of the parameters and equating to zero.

$$\frac{\partial E}{\partial A} = 0 = -2 \sum_{i=1}^{n} [y_i - (A + Bx_i + Cx_i^2)]$$

$$\frac{\partial E}{\partial B} = 0 = -2 \sum_{i=1}^{n} [y_i - (A + Bx_i + Cx_i^2)]x_i$$

$$\frac{\partial E}{\partial C} = 0 = -2 \sum_{i=1}^{n} [y_i - (A + Bx_i + Cx_i^2)]x_i^2$$

Dropping the limits on the summations and writing in matrix form,

$$\begin{bmatrix} n & \Sigma x & \Sigma x^2 \\ \Sigma x & \Sigma x^2 & \Sigma x^3 \\ \Sigma x^2 & \Sigma x^3 & \Sigma x^4 \end{bmatrix} \begin{bmatrix} A \\ B \\ C \end{bmatrix} = \begin{bmatrix} \Sigma y \\ \Sigma xy \\ \Sigma x^2 y \end{bmatrix}$$

These equations were used to obtain the material properties from the compression test data by including the data points obtained from all the tests at one condition (i.e. one of the twelve unique combinations of fiber orientation, radiation dose, and test temperature) in a single calculation. Young's modulus and Poisson's ratio are the initial slopes of the curves obtained by these calculations. In general, the slope is given by $\frac{dy}{dx} = B + 2Cx$ and the initial slope is simply B.

Two types of functions, $y = f(x)$ and $x = f(y)$, were calculated and found to yield essentially the same values for E and ν. The values of the function of the form $y = f(x)$ were used for convenience.

The failure strains were obtained by solving the $\sigma - \varepsilon$ equations for the value of ε corresponding to the σ at failure (e.g. the strength). Some differences were found in the failure strains obtained from the two types of functions. These differences were resolved by examining the nature of the calculated curves and comparing the final strain gage readings to the calculated values for failure strain.

The properties for the neat resin were obtained in a similar way, except that the regression analysis was conducted on each individual set of test data. The values for the three tests at each condition were then simply averaged together. Another calculation was made in which all the tests at one condition were lumped together (the same as described above for the compression data). The difference between the averages of the three tests and the "lumped" calculation were insignificant.

C.3 Determination of Standard Errors

This section describes the methods used to obtain the standard errors (or deviations) of the various properties. For the compressive strength values, the mean and standard deviation were calculated using the 5 individual values obtained at each condition and the usual formulas,

$$\text{Mean} = \frac{\Sigma x}{n}$$

$$\text{Standard Deviation} = \left[\Sigma x^2 - \frac{(\Sigma x)^2}{n} \right]^{1/2} \frac{}{n-1}$$

The elastic properties and the failure strains for the compression coupons were obtained by using the quadratic regression curves as described in the previous section. The remainder of this section will describe how the interval estimates for the elastic properties and failure strains were obtained.

There are statistical methods which allow error estimates (confidence intervals) to be be made on the curvilinear regression curves. The details of the calculations are rather involved and tedious. The interested reader is referred to Snedecor and Cochran [37].

These error estimates were used to provide bounds on the elastic properties. This process will be described in detail for Young's modulus. The process starts with a set of $\sigma - \varepsilon$ data, an equation, $\sigma = f(\varepsilon) = A + B\varepsilon + C\varepsilon^2$, calculated as described previously, and an error estimate for ε, which will be denoted "s". The initial slope of the $\sigma - \varepsilon$ curve is B. For purposes of establishing a range on B, the straight line portion of the curve was extended to the failure strain (Figure 62). Denote the final stress on this straight line curve as $\hat{\sigma}$ (note that because the $\sigma - \varepsilon$ were all nonlinear to a greater or lesser degree $\hat{\sigma} \neq X_c$). The bounds on B were obtained in the following way,

$$B_{min} = \frac{\hat{\sigma} - 2s}{\varepsilon_f} = B - \frac{2s}{\varepsilon_f}$$

$$B_{max} = \frac{\hat{\sigma} + 2s}{\varepsilon_f} = B + \frac{2s}{\varepsilon_f}$$

The upper and lower bounds, B_{min} and B_{max}, when substituted into the original function for B, were found to produce "envelopes" which contained essentially all the experimental data points.

The interval estimates for Poisson's ratio were calculated in the same manner as that described above. The procedure is exactly as described above with the exception of using transverse strain rather than stress in the calculations.

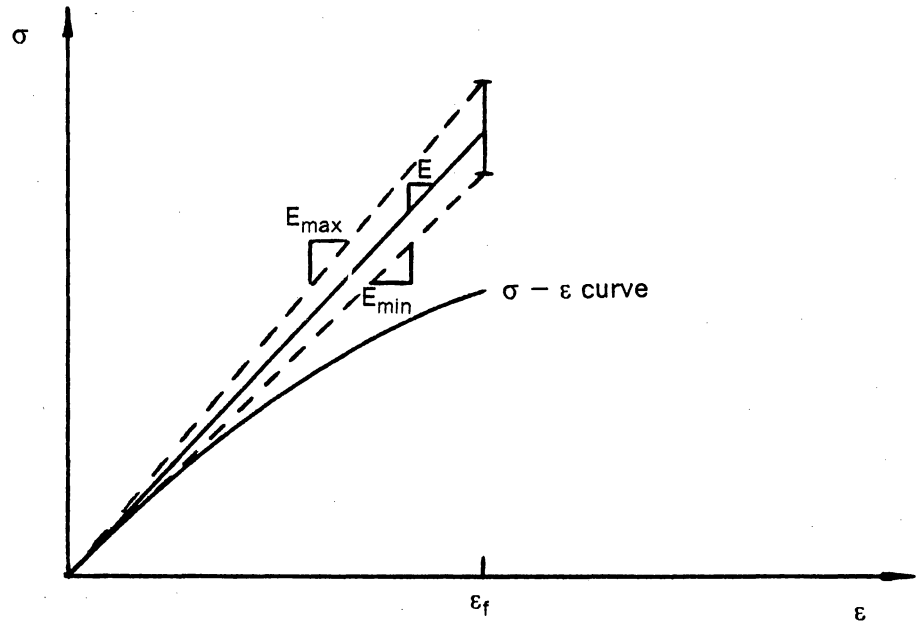

a) Calculation of Upper and Lower Bounds on Modulus

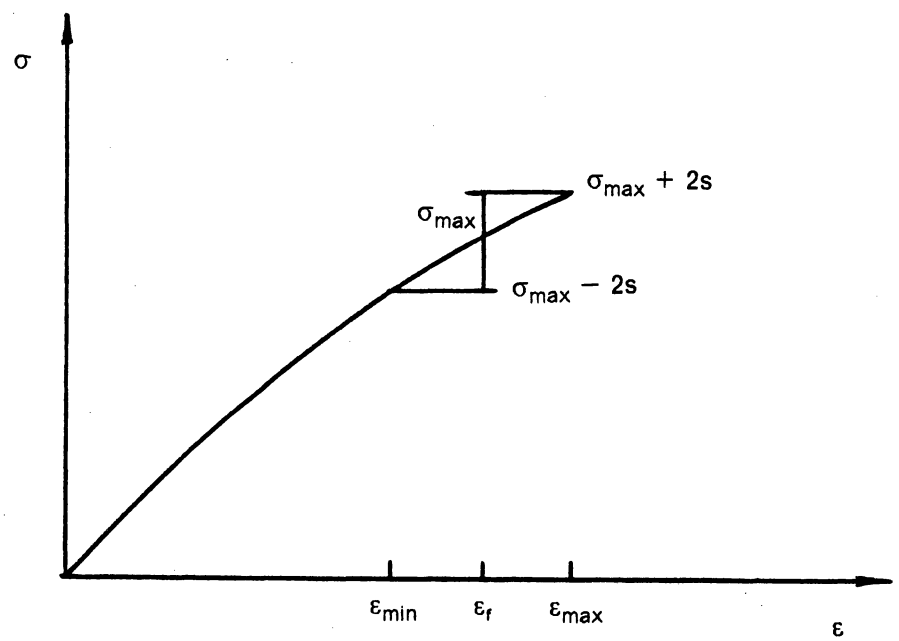

b) Calculation of Upper and Lower Bounds on Failure Strain

Figure 62. Calculation of Bounds on Mechanical Properties

The range for the failure strain was calculated in a similar fashion (Figure 62b). The bounds on the failure strain were obtained by adding $\pm$ 2s to the strength value and solving the $\sigma = f(\varepsilon)$ equation for the corresponding strain values.

The vita has been removed from the scanned document